Mémoire

Auteur : Dethinne, Thomas
Promoteur(s) : Barbier, Christian; Fettweis, Xavier
Faculté : Faculté des Sciences
Diplôme : Master en sciences géographiques, orientation géomatique, à finalité spécialisée en géomètre-expert
Année académique : 2020-2021
URI/URL : http://hdl.handle.net/2268.2/11761

Faculty of Sciences
Geography department

Comparison Between Surface Melt Estimation From Sentinel-1 Synthetic Aperture Radar and a Regional Climate Model

Case Study Over the Roi Baudouin Ice Shelf, East Antarctica

Master thesis presented by: **Thomas DETHINNE**

For obtaining the title of
Master in geographic sciences, geomatics and geometrology orientation, land surveyor finality

Academic year	**2020-2021**
Defence date	**June 2021**
Jury president:	**Pr. René WARNANT**
Promoter:	**Pr. Christian BARBIER**
	Pr. Xavier FETTWEIS
Reading juries:	**Pr. Florent POUX**
	Pr. René WARNANT

First, I would like to thanks M. Xavier Fettweis and M. Christian Barbier, my promoters for making this cross-section master thesis possible.

Then, the Liège Space Center as well as its employees for welcoming me in their facilities and allowing me to use their equipment, without which the treatments would have taken a lot more time.

A special thanks to Quentin Glaude, for his help, his time, his advice and all the other things he made for me finishing in time.

I also would like to thanks Christoph Kittel and Charles Amory for their interest in my work as well as the provided help to understand MAR and for the data.

Thank you to the juries for the interest and time invested in the reading and judging of the master thesis

I wanted to thanks Marine Langlet for the reading and correction.

A last thanks to Evelyne Troussart for the time spend helping me finding the right words and supporting me during the redaction.

Abstract

Global warming, melting ice sheet, sea levels rise, natural disasters - these are words and sentences that we have heard a lot in recent years. In a changing world, studying the poles and their conservation is very important. However, it is often hard to obtain high-resolution data on this vast and distant continent.

Thanks to the Copernicus space program providing free and open-access to high-quality data, this master thesis aims to show the complementarity between Sentinel-1 images and Modèle Atmosphérique régional (MAR) data over Antarctica. This study is conducted over Roi Baudouin Ice Shelf.

The complementarity between the two datasets is established by a quantitative, temporal and spatial comparison of the amplitude information of the radar signal and several variables modelled by MAR. To archive it, mosaics of Sentinel images had to be created to cover a larger area and to allow a comparison of same-day interpolated data.

Obtained results are quite promising. Comparisons show very strong spatial correlations between MAR variables representing melt and the backscatter coefficient recorded by the satellite. Although temporal and quantitative analyses also give great results, there are still questions in some areas of the platform that do not behave in the same way as the rest.

This thesis, therefore, opens up many possibilities in research by showing that most of the time, the results match but in some cases, it is more subtle. Certain questions thus remain open, arousing curiosity but also prospects of complimentary use of radar satellites and climate models.

Résumé

Réchauffement climatique, fonte des glaciers, hausse du niveau de la mer, catastrophes naturelles, ce sont autant de mots et d'expressions que l'on entend beaucoup ces dernières années. Dans un monde en plein changement, l'étude des pôles et leur conservation n'en est que plus important. Or, il est souvent difficile d'obtenir des données à haute résolution sur ce vaste et lointain continent.

Grâce au programme spatial Copernicus qui donne un accès libre et gratuit à des images satellites de hautes qualités, le but de ce mémoire est de montrer la complémentarité entre les images radar Sentinel-1 et les données du Modèle Atmosphérique Régional (MAR) au niveau de l'Antarctique. Cette étude est menée au niveau de plateforme de glace du Roi Baudouin.

La complémentarité entre les deux jeux donnés est établie par une comparaison quantitative, temporel et spatiale entre l'information d'amplitude du signal radar et différentes variables modélisées par MAR. Pour ce faire, un mosaïquage des images Sentinel a dû être réalisé afin de couvrir une plus grande zone et permettre une comparaison des données interpolées au même jour.

Les résultats obtenus sont assez prometteurs. Les comparaisons montrent de très fortes corrélations spatiales entre les variables MAR représentant la fonte et les coefficients de rétrodiffusion enregistrés par le satellite. Et même si les analyses temporelles et quantitatives donnent aussi de bons résultats, il reste des interrogations dans certaines zones de la plateforme qui ne se comportent pas de la même façon.

Ce mémoire ouvre donc de nombreuses possibilités de recherche en montrant que la plupart du temps, les résultats concordent mais que dans certains cas, ils sont plus subtils. Certaines questions restent donc ouvertes attisant la curiosité mais aussi la perspective d'une utilisation complémentaire des satellites radar et des modèles climatiques.

Contents

Chapter 1

Introduction

Snow and ice melt are increasing in the polar region and this made sea level rise for the last few years (Scambos et al., 2013; The IMBIE team et al., 2018). Even more problematic, this phenomenon is ongoing and could increase with global warming (Gilbert & Kittel, 2021; The IMBIE team et al., 2018). Exploring the regions where the ice is melting is a difficult task due to the remoteness and the size of the continent as well as the weather. To simplify the life of many scientists, numerous ways of remotely observing those places have been developed (Nagler et al., 2015; Baghdadi et al., 2000; Nagler & Rott, 2000). At the University of Liège, SPHERES laboratory is working with the predictive "modèle atmosphérique régional" (MAR) model to do so. However, nothing is perfect and the model cannot be used to study ice melt with extreme precision. Firstly because small input errors can result in larger output errors. Secondly, results are provided with a kilometric resolution, which is larger than the resolution satellites can archive nowadays. With the spatial activity development and the launch of more and more satellites, remote sensing began to be one of the techniques used to monitor polar regions (Nagler et al., 2015; Nagler & Rott, 2000; Nagler et al., 2016; Fettweis et al., 2006, 2011; Shah et al., 2019; Lievens et al., 2019). It began with passive satellites as they were the most commonly used and the firsts to provide commercial products. (Parkinson, 2001; Gloersen et al., 1993)

But then, the rise of active remote sensing satellites begins, especially with the Earth observation program from the European Union, Copernicus, allowing to dispose of near-daily radar images with a resolution of the order of 10 metres in open access with the Sentinel constellation (ESA, 2019). Because the active radar satellite output is sensitive to water content, it can be used to detect melt in images (see sub-section 2.3.2). Having a high-resolution technique to monitor the climate in remote places could enable an enhancement for the predictive models

and a better understanding of the mechanisms taking place there.

1.1 Objectives

By working in cooperation with the SPHERES Laboratory from Uliege and the Signal Processing Laboratory from Liege Space Centre, this master thesis has the objective to compare MAR's modellisations with the observations made by Sentinel-1 satellites. The comparison will be made using three methods: quantitatively, temporally, and spatially.
By analysing them, it is possible to understand the differences that exist between the modellisations and the observations made from space. Using Sentinnel-1, satellites images can be seen as a free, high-quality and resolution, open-access resource to be used in conjunction with models to improve the results of both sides.
Such comparisons have already been made but, most of the time, with passive satellites (Parkinson, 2001; Lievens et al., 2019; Fettweis et al., 2011, 2006; Gloersen et al., 1993). As presented further in this paper, it is active satellites that are used. Active remote sensing techniques have advantages with relation to passives ones. Those advantages could be relevant in several situations and help in the research sector.
This master thesis aims to use as much as possible free and open-access materials. Satellites images used are free to access and images processing and visualising are made with open-source softwares.
This master thesis is in collaboration with two laboratories that are not from the geomatic unit. It enabled to work with peoples already actives in the research field and get an idea of how this environment functions and may help to prepare for a possible PhD application.
In order to fulfil the objectives, the present work is divided as follow. The next part describes the area the analysis is conducted on. Chapter 2 is a short summary of the different aspects needed to understand the experiment as well as a state of the previously conducted similar works. Chapter 3 explains the workflow and methodology applied. Chapter 4 is the description of the data used. The treatment and the processing of the images are explained in Chapter 5, while Chapter 6 is dedicated to the comparisons.

1.2 Region of Interest

The region studied in this case is the King Baudouin ice shelf (Or Roi Baudouin ice shelf (RBIS)) and its surroundings, in the Dronning Maud Land, East of Antarctica (fig 1.2). The region is +- 700 km by 135 km, for an ice cover area of approximately 70.000 km^2. The real area studied for each image depends on the image availability and can change between two dates.
An ice shelf is a platform of ice, hundreds of meters in height, that floats on the water. The ice comes from the ice sheet that has flowed into the sea (fig 1.1). If ice shelves may appear insignificant in comparison to the ice sheet, it is just the opposite. Ice shelves exercise a buttressing effect on the glacier from which the ice comes (Dupont & Alley, 2006; Reese et al., 2018). It prevents the ice from passively flows into the ocean due to gravity. Nonetheless, ice shelf should not be confused with sea ice as ice shelf is directly coming from the ice sheet and can be hundreds of meters thick when sea ice comes from the seawater freezing on several meters.

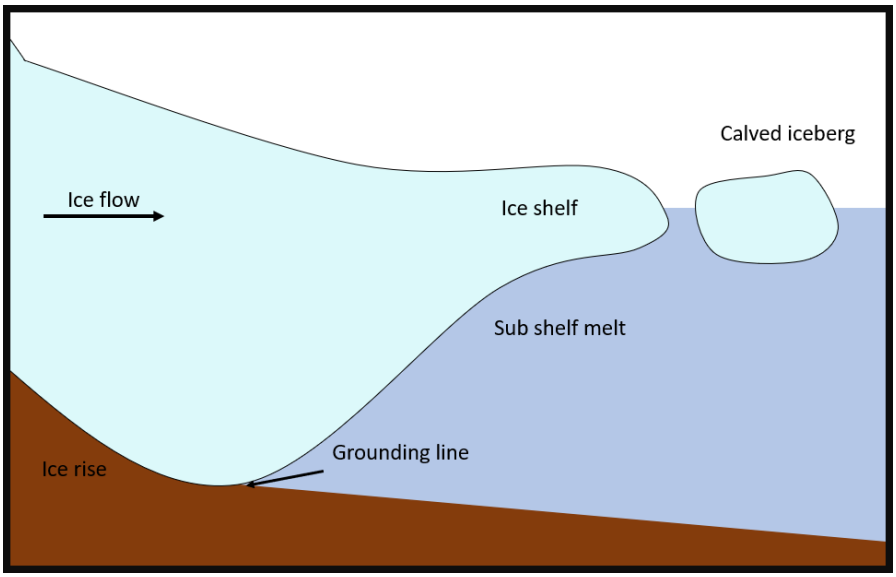

Figure 1.1: Schematic of an ice shelf (Davies, 2020; modified). Ice shelf is the ice coming from the ice cap but floating on the water. Here the schematic does not respect scale, the tongue of ice can be hundred kilometres long for a much smaller high. The separation between ice cap and ice shelf is chosen at the grounding line, the line where ice leaves the ground to float.

With two principal flux of ice (Rignot et al., 2017), divided by the Derwael ice rise (rising ground that blocks the movement of ice), RBIS is not one of the most active ice shelf (Rignot et al., 2013). It makes the comparison easier. Episodes of icebergs calving or fracturing would disrupt the study. Same for fast melt and

refreezing that would not be detected by satellite due to image availability. This is one of the reasons why this zone has been chosen as well as the fact that the ice shelf has already been studied numerous times.
The far south of the zone is a steep slope leading to inland territories. The slope is source of katabatic winds creating surface ablation and possible melt resulting in sub-glacial lakes (Lenaerts et al., 2016). Ablation taking place in the zone also causes blue-ice to be at the surface in three locations in the studied area (fig 5.10). Blue ice is old, blue-coloured, clean glacier ice that covers less than 2% of the Antarctica ice sheet. With a lower albedo, blue ice tends to enhance melt rates. The presence of blue ice permits bringing to the fore the different behaviours of ice in the zone.
At the start of the work, it was planned to create a complete algorithm over RBIS and applying it to a larger zone afterwards. Some complications and delays made the larger-scale analysis impossible as part of this work.

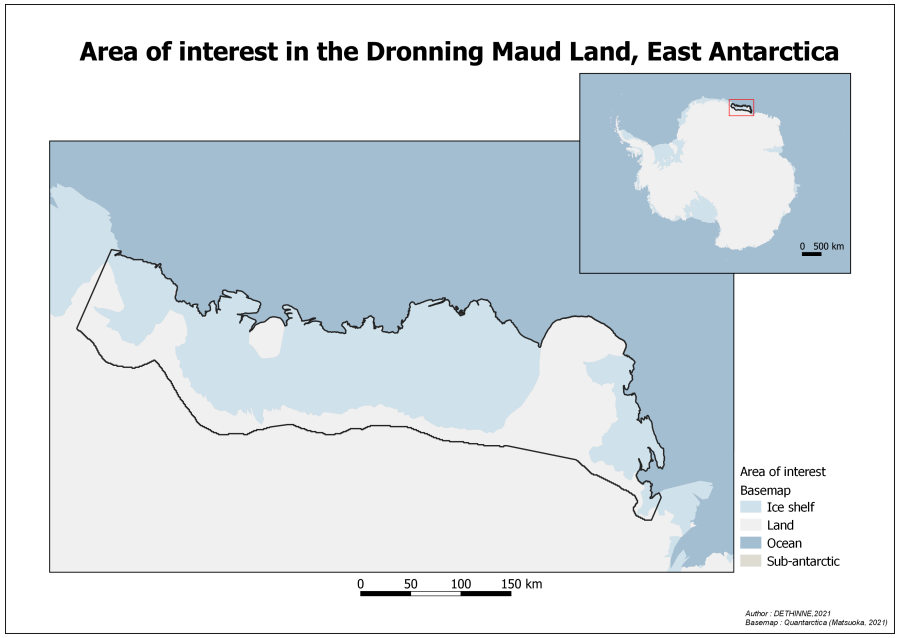

Figure 1.2: Presentation of the studied zone. The area of interest, RBIS, is located in East Antarctica. Parts of Prince Harald and Borchgrevink ice shelves are also included in the area as well as the Derwael ice rise and the Riiser-Larsenhalvøya ice ridge. The starting area has a surface of 66 000km^2, 2 times bigger than Belgium.

Chapter 2

State of the Art

As discussed in the previous parts, this paper's main objective is to compare the melt detected in specific satellite's images and the melt modelled by MAR. However, to complete this objective, several aspects of glaciology and remote sensing have to be studied to understand the viability and relevance of this work. The link between satellite imagery systems acquiring images of hundreds of kilometres square and ice melt, sometimes not even visible bare eye, is not blatant. That is why the problem is approached by three sides: ice melt, MAR and SAR. The following section explains the three problematics, in varying degrees of detail, depending on the needs of the analysis.

2.1 Ice Melt

Fill a cup with water, add ice cubes until the water is at the edge of the cup. Let the cubes melt. The water did not spill. This phenomenon is due to the change in density of the water when it freezes (Bartels-Rausch et al., 2012). When freezing occurs, there is a change in the molecular and crystalline structure that makes the water taking more space. The density is then lowered and if the ice melts, the underwater zone occupied by the ice will be replaced with liquid water. Due to this physical particularity, the melting of ice shelves does not directly participate in sea level rising. As stated before and as shown in fig 1.1, ice from the ice shelf floats on water.

Meltwater from ice shelves not participating in sea-level rise does not mean losing ice shelves is not a problem. As explained before, with the buttressing effect, ice shelf act as an anchor for the ice sheet by stopping it from flowing, leaving lands and melting in the ocean (Dupont & Alley, 2006; Reese et al., 2018). However, even if in opposition to Greenland, Antarctica ice sheet surface mass balance (SMB, i.e.

the result of the difference between the ablation and accumulation process over the ice sheet) should increases because of snowfall enhancement due to atmospheric warming (Lenaerts et al., 2019; Shepherd & Wingham, 2007; Kittel, 2021), meltwater tends to destabilise ice shelves. As explained in Banwell and Macayeal, this is due to the water percolating into the firn (multilayer, compressed snow with a density lower than 830 kg/m^3 (Lenaerts et al., 2019)), creating ponds and lakes in the ice shelf. After several years, ponds will create tension at the bottom of the ice shelf, which may result in break-ups.

Even more, observations show that ice shelves tend to melt and get thinner during the several past years (Reese et al., 2018; Banwell & Macayeal, 2015; Rignot et al., 2013; Paolo et al., 2015; Rignot et al., 2008). It is thus a growing problem: retroactive phenomena can occur. Ice shelf breaking cause more melt, causing sea level to rise, which cause the atmosphere to warm, which cause the ice to melt and so forth (Scambos et al., 2004). Some models also show an increase in surface melt and runoff with future warming (Gilbert & Kittel, 2021).

If Antarctica ice cap would melt entirely, estimations made with the Data Elevation Model (DEM) "Bedmap2" suggests a rising of the sea level for about 58m (P. Fretwell et al., 2013) but there is a lot of uncertainties when talking about the mass balance of ice sheets (Shepherd & Wingham, 2007; Rignot et al., 2008; Gilbert & Kittel, 2021). By rising, the sea can cause multiple problems: the destruction of coastal habitats and inland habitats for high rise, more dangerous hurricanes and typhoons, and other disasters. Already, people are forced to migrate to get in a safer place and millions of people are threatened by the sea level change (Nuñez, 2019; Stern, 2007). Global warming is not only about sea level rising, it is a much more global and long term problem. With the temperature rise comes repercussion on water and food supplies, health problems and much more (Stern, 2007).

If warming has repercussion on human through environmental problems, some animals also directly suffer from the melt as it destructs their natural habitat. For the Northern ice caps, the polar bear may be the most emblematic animal to represents this problem (Ferguson et al., 2000). When for Antarctica, it may be penguins. The studied zone was discovered to be a large host zone for Emperor penguin as in 2009, almost 5 per cent of Antarctica's population of Emperor penguin was observed there within two colonies (P. T. Fretwell et al., 2012). Those two marine colonies, near the Princess Ragnhild coast and the Riiser-Larsen Peninsula, have also been pinpointed as two Important Bird Areas, respectively number ANT114 and ANT115 (C. M. Harris et al., 2015). With the destruction and the properties

changes in their habitat, a 1°C warming could cause 10% of land species to face extinction. For a 3°C warming this number goes up to 50% (Stern, 2007).
The melt study with satellite in this paper is the liquid water formed by surface ice and snow melting (see explanation in subsection 2.3). But in reality, ice shelves melt in multiple ways. For example, basalt melting is another way for ice shelves to melt (Walker et al., 2008; Reese et al., 2018; Pritchard et al., 2012). However, as the grounding line is several hundred meters under the surface (as seen in fig 1.1), it is more difficult to study this melt with spaceborne sensors. Other types of vehicles are used to navigate under the cap of ice (Price et al., 2008).
RBIS being an ice shelf in East Antarctica, it is less probable to see important variations through the years as several studies show less mass balance in East than in West (Lenaerts et al., 2019; Thomas et al., 2004; Paolo et al., 2015; The IMBIE team et al., 2018; Shepherd & Wingham, 2007).
Ice melting in Antarctica remains a challenge as there are not a lot of ground samples available (Lenaerts et al., 2019). Expeditions are expensive and automatic weather stations still need to be collected and are distributed with a large distance on the continent. This lack of ground truth and ways to confirm the analysis is a problem for the verification of the thresholds used during this study. Data accessibility is one of the main reason why satellites are used to monitor the poles. They provide a lot of information and enable studying the zone more easily.

2.2 Modèle Atmoshérique Régional

2.2.1 Atmospheric Model

The atmospheric regional model is used to model and simulate diverse climate variables (*e.g.* quantity of rain, surface melt, wind speed and others). Often used to study polar regions, it has been applied over Greenland (Fettweis et al., 2006, 2011; Fettweis, 2007) and Antarctica (Kittel et al., 2018, 2021; Gilbert & Kittel, 2021; Kittel et al., 2021; Amory et al., 2020). The base of the model is primitive equations described in Gallée and Schayes (1994).
The model includes a microphysics module for the clouds (Gallée, 1995) and the radiative transfer scheme is adapted from (Morcrette, 2002).
As explained in Amory et al. (2020), MAR topography is derived from Bedmap2 DEM (P. Fretwell et al., 2013), at a 1km resolution. Amory et al. also stipulate that MAR is driven by the 6 hourly ERA5 reanalysis fields (Hersbach et al., 2020). This means that the model's variables are forced at its lateral boundaries (pressure, specific humidity, temperature and wind speed), at the top of the troposphere

(temperature and wind speed) and at the ocean surface (sea ice concentration and sea surface temperature). The latest updates of version 3.11 used are described in (Kittel et al., 2021). The model is referenced as "MAR" hereafter.

2.2.2 Surface Model

The model explained right above is the atmospheric part of MAR. The model is also coupled with a surface model: SISVAT (Soil-Ice-Snow-Vegetation-Atmosphere-Transfer). This link allows handling the exchanges between surface and atmosphere and at the same time, keeping the energy balance. The model also has a layer's representation for snow and ice (Gallée et al., 2001; Lefebre et al., 2003).
SISVAT allows describing the layers of snow and ice with different attributes as water content, temperature or grain size. In this study, only the layers making the first meter of depth were used. In the case of precipitation or deposit, if the maximum number of snow layer has already been reached, a new layer is formed at the surface through the aggregation of internal layers. It means that two layers can merge in the case they present similar properties. The different layers of snow and ice interact with each other as well as with the atmosphere. Hydrological and thermodynamic calculus are used to model heat and water transfer. Melt, run-off and meltwater refreezing and accumulation can be derived from water mass conservation (Parotto, 2019).

2.3 Remote Sensing

2.3.1 Spaceborne Remote Sensing

In general, the name remote sensing is used to define the action of collecting data and monitoring the physical properties of a body from a distance (USGS, 2020). Hereafter, remote sensing is used to talk about the monitoring of the Earth from satellites equipped with different sensors.
Satellite's observations bring several advantages compared to *in-situ* observations. But they also can have some disadvantages. When the time resolution is generally greater (images are available almost all the time during the year for several years), the spatial resolution of the sensor cannot permit the study of a small punctual event or a deep underground event. However, satellite's observations, because they cover a large zone (see section 4.2), allow studying a larger area that cannot be covered on foot during the same time.
To monitor the Earth, satellites orbit it. The orbit is an ellipse with a low eccen-

tricity, the Earth being one of the focal points. The closest point to the Earth is named the perigee and the further, the peak. The orbits are categorised by their altitude or their inclination. The inclination is the angle formed by the equatorial plane and the orbital plane. The orbit is said direct when the angle is smaller than 90°, the rotation of the satellite is in the same rotational direction when projected on the equatorial plane. In opposition, when the angle is between 90° and 180°, the orbit is said retrograde, meaning that when projected in the equatorial plane, the orbit rotation is opposed to the Earth's one. When the angle is close to 90°, the satellites fly near the poles. We then talk about polar orbit.
Concerning their height, there are three main orbits, depending on the mission, the constellation and the time resolution needed.
The closest to the Earth is the low earth orbit, with an altitude of approximately 1.000 km. This orbit allows reaching a revolution period of one or two hours. Gravity depends on the altitude and speed depends on gravity. So the speed of the spacecraft orbiting the Earth at a certain altitude can then be approximated by:

$$v = \sqrt{\frac{g \cdot Re}{R}} \tag{2.1}$$

With g, the universal constant of gravity, R_e the radius of the Earth and R, R_e increased by the altitude of the orbit.
The further orbit is the geostationary orbit. Given the altitude of 35.786 km and because of equation (2.1), it allows the satellite to turn around the Earth at the same speed as the Earth rotates, assuming one sidereal day lasting for 86164 sec. Such satellites stay above the same point all the time of their mission. However, to achieve such an orbit, the satellite needs to be in the equatorial plane, making the observation of the poles impossible.
Between the two previous orbits is the medium earth orbit. With an altitude ranging from 1.500 to 35.000km, this orbit is often chosen for GNSS satellites because the farthest from the Earth, the more places it is visible from.
It is possible for a satellite to pass over a point on the Earth at almost the same time for each passage. This type of orbit is called "sun-synchronous" (Boain, 2004). It allows to keep the same condition of illumination on the scene and permits a better comparison of two images (Tychon, 2019).
When talking about satellite remote sensing, we make the distinction between two different families of imagery depending on the signal's source used. On one hand, there is the passive one and on the other hand, the active one (fig 2.1). Both have already been used in order to observe the evolution of ice (The IMBIE team et al.,

2018; Lenaerts et al., 2019; Paolo et al., 2015; Shepherd & Wingham, 2007; Rignot et al., 2008; Baghdadi et al., 2000; Nagler & Rott, 2000; Nagler et al., 2015, 2016; Mahmud et al., 2020; Ramjan et al., 2018; Johnson et al., 2020; Buchelt et al., 2021).

2.3.2 Active Satellite Imagery

This section is explaining the basic principle of active satellites using synthetic-aperture technology. They are called SAR (synthetic-aperture radar) to be distinguished from the other radars. The information presented hereupon is a summary of university hearings (Tychon, 2019; Glaude, 2018), online-classes (EO College, 2020, 2021), and a journal article (Moreira et al., 2013).

Principle

As explained before, the main difference between active and passive is the source of the signal used. Passive satellites observed the Earth and record the quantity of Sun's energy the object on the Earth reflects in different wavelengths. Whereas, as its name implies, SAR is basically a RADAR. It means that the satellite transmits high-frequency electromagnetic pulses and records the backscattered echo. Not

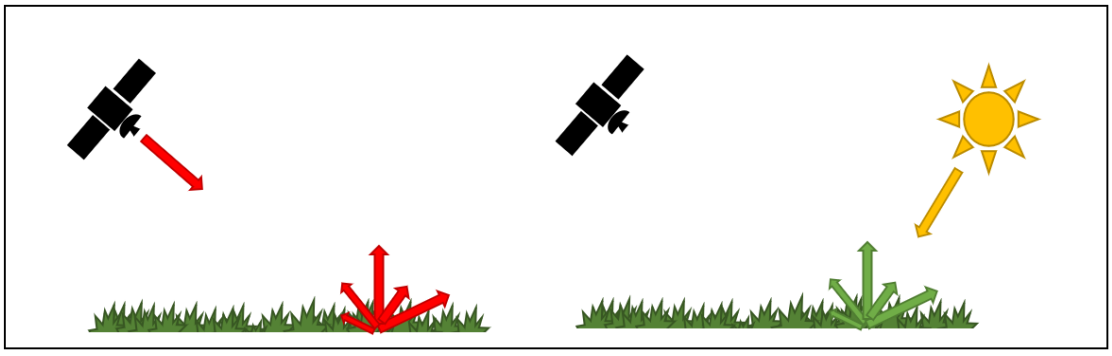

Figure 2.1: Difference between active and passive satellites. The left image shows how an active satellite works. It emits a signal that interacts with the ground and registers the part of the signal that comes back to the sensor. The right one shows the functioning of a passive one. Passive satellites do not emit a signal. They record the quantity of energy reflected or emitted by the ground. Most of the time, this energy is provided by the Sun.

being dependant on other parties to send a signal to listen to is an advantage. By sending its signal, compared to passive satellites, SAR can make observations during day and night. Even if this does not seem to be important in our regions, the higher the latitude (or the lower), the longer the night in winter. In Antarctica, this results in a night of several days or even months, making the passive imagery

almost impossible during winter.
Another advantage SAR has upon passive satellite is the frequency range used. When passive sensors mostly use visible and infrared frequency (wavelength in the order of a µm), SAR emits microwave frequency pulses (between 1 to 40 GHz). The frequency range is divided into several bands (fig 2.2). The most commonly used are L, S, C, X. There is no link between the name of the band and its wavelength. By working at such a high frequency, most of the time, radar satellites are free from atmospheric effects and clouds in the image as they penetrate through them.

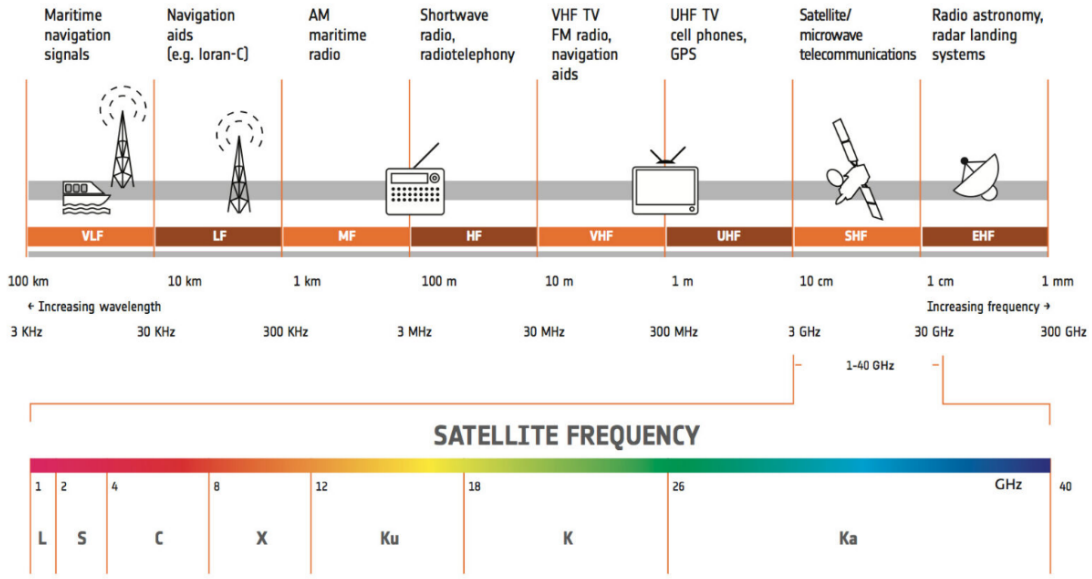

Figure 2.2: Frequency range from various applications. The frequency range of electromagnetic wave is very large. It can go from a few kHz to 300GHz. Usually, frequency range used in radar satellites ranges from 1GHz to 40GHz, corresponding to wavelengths of approximately 30cm and 0,7mm. To distinguish the frequency used by a satellite, the frequency range is divided into several bands of smaller range. A commonly uses band to observe the Earth is the C band, with a wavelength of about 5cm.

Because waves interact with objects bigger or of the size of their wavelength, depending on the band used, the signal emitted by radar satellites can penetrate through vegetation and soil. This way, the greater the band, the more penetration. However, care must be taken that humidity conditions also affect this property. The presence of effects caused by water will be discussed later in the section.
The acquisition geometry is a bit unique (fig 2.3). Like other satellites, radar satellite flies following the azimuth direction and its projection on the surface is called the nadir. Nevertheless, SAR broadly measures the time between the pulse emission and the return of that pulse. The range represents that time and is the distance between the sensor and the illuminated area. It is then impossible for

the radar to be directed under the pod, otherwise, it would confuse its left and right. The satellite, therefore, moves looking at one side. The length between the closest illuminated point and the farthest is the swath. Swath and azimuth define the coordinate system of the image: azimuth = Y and range = X.

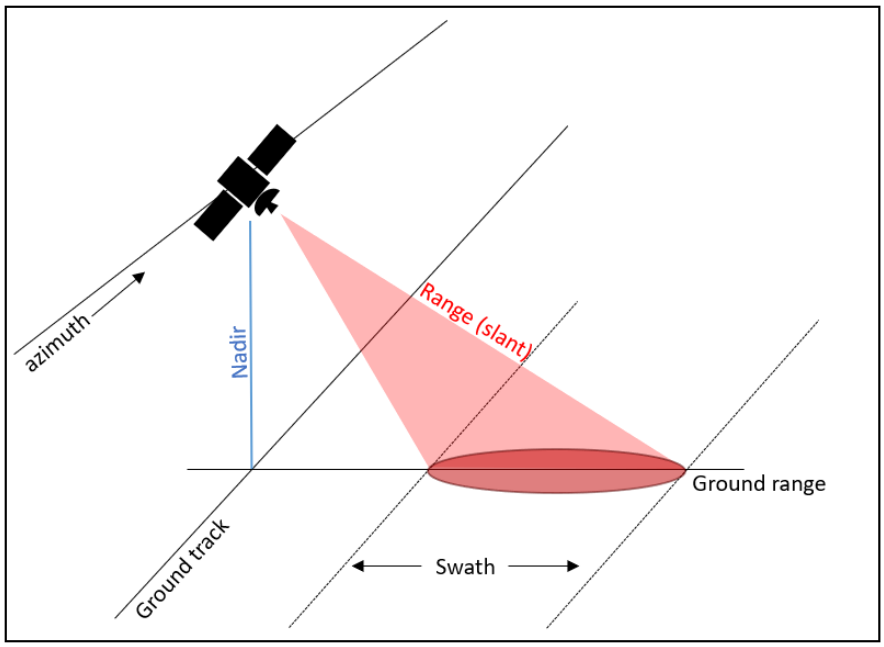

Figure 2.3: Schematic of a radar satellite acquisition geometry. A satellite flies along the azimuth direction, aiming the Earth in the range direction. The projected position of the fly direction is the ground track and the direction of the satellite's projection on the ground is the nadir. Swath is the length in which the data are recorded.

To create an image scene, SAR needs to transform many pulses reflected by every single target of that scene and received by the antenna. The processing can be considered as a two-dimensional operation: the range focusing and the azimuth focusing. For the range compression, the signal is multiplied by a complex conjugate of the spectrum of the transmitted chirp in the frequency domain. It is almost equivalent to a convolution in time domain but with less computation load. The result is information on the distance between the sensor and the point on the ground. The azimuth compression follows the same reasoning but following a function of the range. After this processing, SAR images are called "Single Look Complex", the images containing amplitude and phase information.
The resolution of such images is variable regarding range or azimuth (fig 2.4). When talking of resolution, resolution and pixel size should not be confused. Resolution is the smallest distance between two points that can be detected separately. Pixel size is the distance between two pixel's centre in the image, being the sampling in the signal. The slant-range resolution is the simplest of the two resolutions.

As seen in fig 2.4, it can be easily approximated by:

$$\delta_r = \frac{c \cdot \tau}{2cos(\theta)} \tag{2.2}$$

With c the speed of light, τ the duration of the pulse and θ the complement of the incidence angle i. i Being variable for the same scene (its value increases with distance from the sensor), the range resolution is variable inside the scene. Causing some geometrical distortions that can be corrected. In more precise terms,

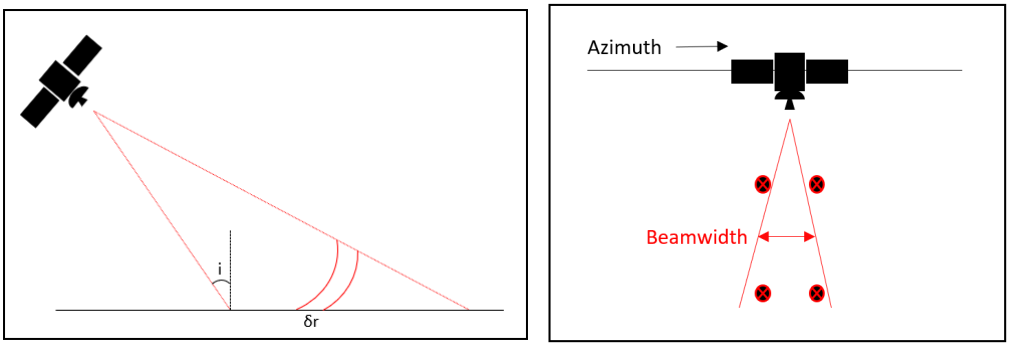

Figure 2.4: Range and azimuth resolutions. The left schematic represents the explanation for the range resolution. For two objects to be distinguished, they have to be distant for more than δ_r or else they will participate in the same backscatter. The incidence angle, i, varies inside the swath, making δ_r varying too. The right schematic is an example for understand the azimuth resolution without the synthetic aperture technology. For two objects to be distinguished, they have not to be inside the same beam. As for the range, the azimuth resolution decreases with range because beamwidth grows with range.

because SAR does not really use simple pulses but use frequency-modulated pulses waveforms, the concept of bandwidth is used. The amplitude of the pulse is constant during the time of the pulse but the frequency is variable over time. The ratio between this frequency and time give the chirp rate. Chirp rate, k_r, is the base of the definition of a bandwidth:

$$B_r = k_r \cdot \tau \tag{2.3}$$

The range resolution then becomes:

$$\delta_r = \frac{c}{2B_r} \tag{2.4}$$

For a fixed time emission, the bigger the chirp rate, the bigger the bandwidth, the lower the resolution.
If the range resolution is quite simple and the characteristics of the wave used allow

reaching resolution of a few dozen meters, azimuth resolution is more complicated. To differentiate two different objects, they should not be in the same beamwidth (fig 2.4). Beamwidth (angular diameter of the beam) can be approximated by the ratio of the wavelength used and the length of the antenna:

$$\Phi_r = \frac{\lambda}{d_a} \tag{2.5}$$

And assuming a range distance r_0 from the antenna to a ground point, the azimuth resolution is:

$$\delta_a = \frac{\lambda}{d_a} = \Phi_r \cdot r_0 \tag{2.6}$$

Azimuth resolution has been a major drawback for active airborne and spaceborne systems. Following equation (2.6), to obtain a resolution of several meters when flying thousands of metres (or kilometres for satellites) and using micro-wave, the size needed for the antenna is gigantic and not convenient. This limitation was overcome by two new majors techniques developed during the fifties and sixties. The first one is called the Doppler beam sharpening. The second one, using the principle of the first, is the technique SAR has its name based on: the synthetic aperture (SA, fig 2.5). SA aims to create a longer, synthetic, antenna from the physical antenna (Cutrona et al., 1961).

To form the antenna, all the pulses in which an object is visible is used and are treated all at once. By adding all those together, a kilometre-long antenna is artificially created from a physical antenna of a few metres long. During the time an echo from an object can be listen to by the SAR, the position of the object is reached by using the first technique, Doppler beam sharpening (Wiley, 1985).

To find the position of the object, not only the amplitude of the echo is examined, the frequency is used too. According to the Doppler effect, if a relative movement exists between a transmitter and a receptor, the receptor will receive the transmitted wave with a higher frequency if the two objects get closer or with a lower one if they get distant. This phenomenon is exactly what happens with the echo. SAR is in motion with respect to the backscattering object and perceives the echo with a different frequency for each pulse. By applying this technique, the beam is sharpened (less broad) and δ_a reaches a resolution of a dozen metres as for δ_r. However, SA leads to interesting conclusions. The length of SA is given by:

$$L_{sa} = \Phi_r \cdot r_0 = \frac{\lambda \cdot r_0}{d_a} \tag{2.7}$$

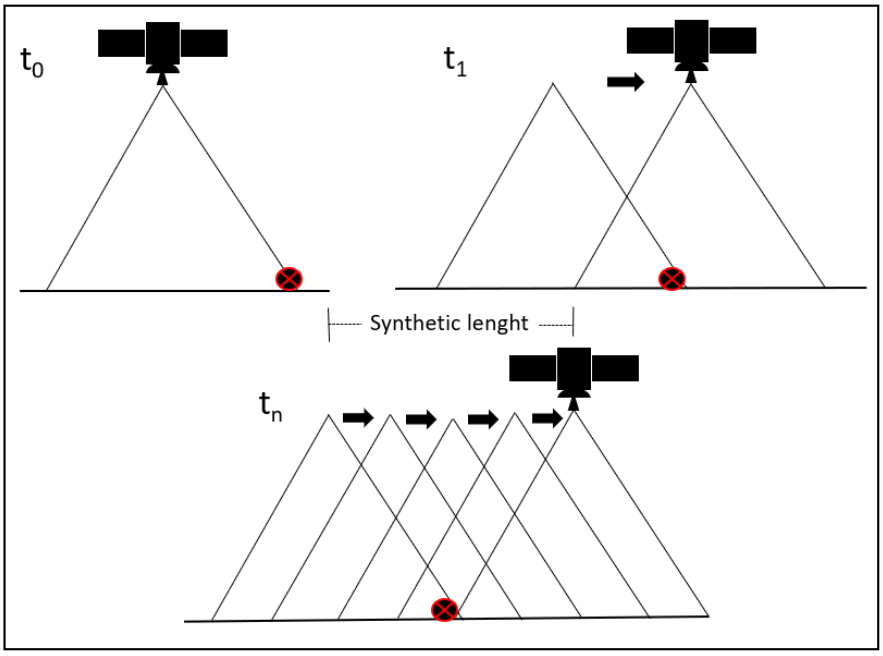

Figure 2.5: Synthetic aperture radar technique. Synthetic aperture (SA) technique consists in the creation of an artificially longer antenna. It is constructed for a ground object from all the acquisitions in which the element is visible. The technique is used with Doppler beam sharpening to enhance the azimuth resolution, limiting factor of the radar imagery.

By combining equations (2.6) and (2.7):

$$\delta_a = \Phi_{sa} \cdot r_0 = \frac{\lambda \cdot r_0}{2L_{sa}} = \frac{d_a}{2} \tag{2.8}$$

To get a better azimuth resolution, equations (2.6) required a longer antenna but equations (2.8) says the opposite. The paradox is solved by thinking that a smaller antenna can distinguish an object for longer since its beam will be larger, resulting in a longer SA. It is important to note that both resolution do not depend on the distance to the ground, allowing the use a satellite. Nonetheless, sensor still needs to be able to catch an echo that is not too noisy, thus the signal have to be strong or the sensor to be close to the Earth.

There are 3 base modes for SAR to record images: strip map, scanSAR and spotlight. Strip map is the standard model. The pattern is fixed to one swath resulting in a single continuous strip. The scanSAR mode is used when a wider swath is required. The antenna elevation is variable, allowing the creation of multiple sub-swath. Each sub-swath is illuminated by pulses but with a shorter time than in strip mode. ScanSAR has a larger swath wide but worst azimuth resolution than in strip map. Spotlight mode is used when a better azimuth resolution is

needed. The antenna is fixed to a certain point on the ground, resulting in a longer synthetic aperture time, giving a better resolution. Consequently, a SAR's path operating in spotlight mode is not a continuous image but rather individual images all along the path. It is possible to swap between each mode but the change is not instantaneous. During the time required for the switch, data cannot be recorded. With Sentinel-1, scanSAR is enhanced in TOPSAR. The resolution and coverage of scanSAR are kept but with less noise. To do so, the SAR beam is tilted in range to swap between the sub-swath but also in the azimuth direction to avoid scalloping. Images resulting from TOPSAR are IW and EW images.

Images Distortions

The acquisition geometry and the method of acquisition itself can causes image distortions. The most commons are shadows, layovers and foreshortenings. The shadow effect (fig 2.6) is almost the same as the effect clouds can have in passively recorded images. Either with passive or actives techniques, to have a returned signal, you need the energy to reach the ground. In certain geometries, a part of the scene can hide another. By obstructing the beam no illumination will reach ground and the corresponding range will appear black in the image.

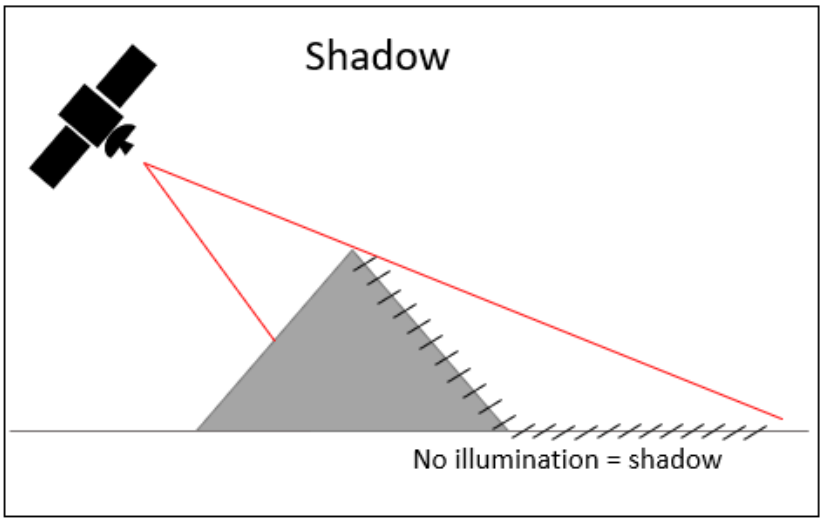

Figure 2.6: Shadow effect. When there is an obstacle between the sensor and a ground zone, no signal can pass through. SAR images are based on the record of the backscatter of this signal. Thus is no signal reach the ground, nothing is recorded and the corresponding range will appear black in the image.

To understand the two distortions presented hereafter, it is to remember that the X axe for SAR images represents the range between the sensor and the ground. In some cases, the top of an object and the bottom of it are almost at the same range. The two extremities are then displayed closer than they should. The object

looks compressed or the slope is steeper. This effect is called the foreshortening effect (fig 2.7).

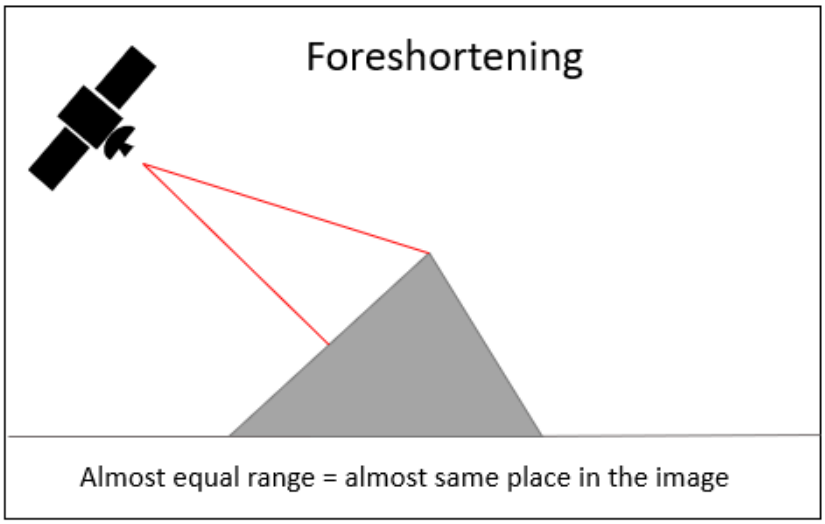

Figure 2.7: Foreshortening effect. The effect of foreshortening is affecting topography. The pixel is placed on the range axe with report to its distance to the sensor. If two points are at the almost same range, they will be represented next to each other in the image even if more distance separates them in reality. The element affected by foreshortening will look shorter/compressed.

Layover is a case of extreme foreshortening. The top of the object is detected before the bottom. When looking in the image, the object looks to be laying on the ground. In fig 2.8, the layover is illustrated by an image of the Eiffel tower. Because the echo of the top of the tower is received first, the tower appears tilted, laying over the Seine.

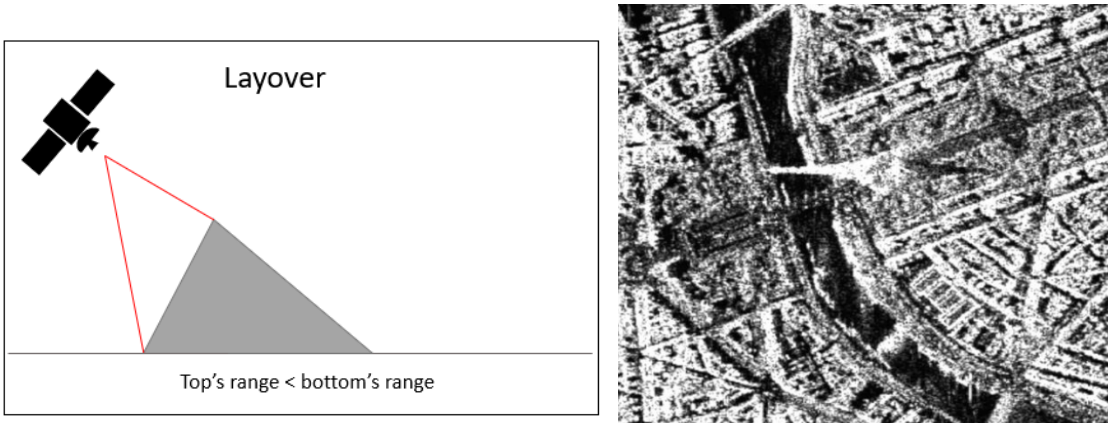

Figure 2.8: Layover effect. Layover is a special case of foreshortening. Top of a tall elements of the scene is closer to the sensor than the bottom. Following the rule that image is constructed in range with the distance, the top appears first in the sensor direction. The right image illustrates layover with the Eiffel tower that seems to be laying on the side.

Observable

As explained before, RADAR observes the backscattered part of the energy emitted. But all surfaces do not scatter in the same way. Here we describe the principle observed scattering (fig 2.9).

1. Including a large spectrum of scattering mechanism is the surface scattering. The beam is directed to the ground and a part of the energy comes back to the sensor, the rest is scattered in all directions. The way the wave is scattered depends on ground properties such as roughness, humidity or sloppiness, and emitter properties as wavelength or polarisation. These influences will be discussed later. Surface scattering occurs on non-vegetated grounds for example.

2. Specular reflection is what could be called "mirror effect". The major part of the power is reflected with the opposite incidence angle. Almost no energy is recorded in that case. Specular reflection occurs with a smooth surface (for the wavelength). Given calm water and a large area covered in concrete almost no backscatter occurs. Sometimes, specular reflection can cause double bounce. It occurs when two surfaces favourable to specular reflection form a 90° angle. The signal bounces on a surface then on the second one, before being redirected to the satellite. Buildings and tree trunks are likely to produce double bounce. Pixels where double bounce happens, appear brighter because a lot of the energy travels back to the sensor. Specular reflection can be seen as a particular case of surface scattering where the energy is scattered in one direction.

3. The last type of reflection discussed here is the volume scattering. When a radar wave penetrates a heterogeneous medium, the signal bounces on every ground target. The resulting scatter is uniform in every direction. Such scatter occurs with vegetation or fresh dry snow.

The energy backscattered by the ground can be calculated from the energy emitted by the antenna. The relation between the two is linear, which means that the backscattered energy is proportional to the emitted energy. The equation that links the two is called the radar equation. It can be written and explained in different ways. Here the presentation of the equation follows the course "Principes fondamentaux de la rétrodiffusion radar" from EO college (EO College, 2021).

$$E_r = \frac{E_s \cdot G^2 \cdot \lambda^2 \cdot (\sigma^0 \cdot A)}{(4\pi)^3 \cdot (c \cdot t)^4} \tag{2.9}$$

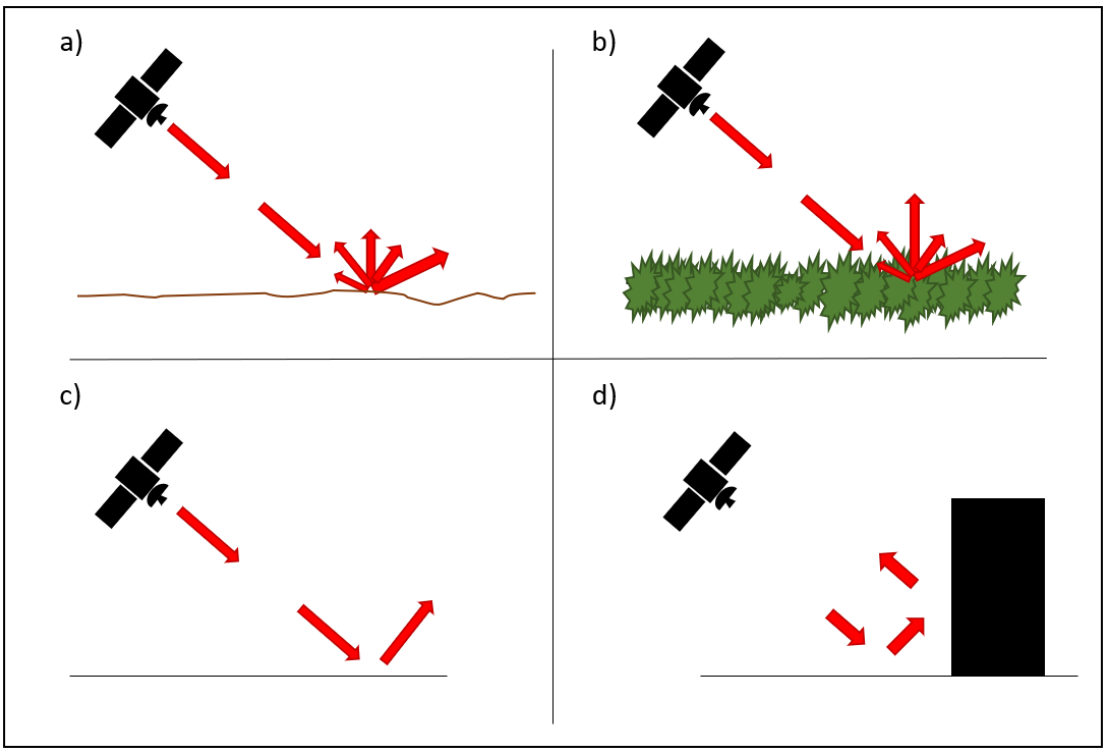

Figure 2.9: Types of backscattering. Image a) represents surface scattering. The energy is emitted towards the ground and the backscatter occurs in every direction. The intensity depends on ground and wave properties. b) Is volume scattering. It happens with heterogeneous media such as foliage or dry snow. c) Is a typical case of specular reflection, almost no signal come back to the sensor. d) Represents double bounce, two perpendicular surfaces causing specular reflection to send the majority of the signal back to the sensor.

Some parts of the equation are more complex than others, but they form the most important equation for SAR imagery.
E_s is the energy emitted for a pulse. This factor is decreasing by a factor of $4\pi R^2$ because the energy is distributed as a sphere doing a round trip to the Earth. This decrease is taken into account with $(c \cdot t)^4$ as the radius of a sphere = c · t/2. The diminution of E_s explains why SAR mainly used low Earth orbit. Deeper orbits would not allow having an echo powerful enough to have clear information on the target.
G is the gain of the antenna. The variable is used to take into account that the antenna does not emit and receive in the same way for all the directions. Square value means the gain is the same for emission and reception.
λ is the wavelength. The choice of λ is very important because, as explained after, it has a relative influence on σ_0. $\frac{\lambda^2}{4\pi}$ is used in the equation to link G to the effective antenna surface at the reception.

A is a surface term. It can be considered as the size of a pixel or the size of the zone illuminated by the antenna.
σ_0 is the backscatter coefficient. It translates the ratio of the energy scattered back to the antenna and the energy reaching the ground. It is independent of the surface as it is normalised by the apparent surface. Commonly, σ_0 is given in decibel as a lot of the collected data are clustered in the low values but some can have much higher values. σ_0 is the only variable of this equation varying with the target properties. The local characteristics influencing σ_0 are the roughness, the topography and the humidity.
The roughness has to be considered with the λ used as the interaction of the wave with the ground depends on the geometry of the soil and the wavelength. There are several methods to calculate the roughness. Rayleigh criterion states that soil is considered as rough if:

$$h > \frac{\lambda}{8} \cdot cos(\Theta) \tag{2.10}$$

With Θ the incidence angle and h the mean quadratic height. A smooth surface will be more likely to cause specular reflection and in the process, a small backscatter coefficient. In the opposite ways, a rough surface tends to create surface scattering and scatters the energy back to the radar.
Topography will influence σ_0 at the cm-scale and at the kilometre-scale. Indeed, as seen in the part dedicated to the geometrical distortion, topography tends to create distortions and shadows that disrupt the images. But topography also plays a role in the roughness. Incidence angle is present in equation (2.10). A steeper slope will appear less rough and will tend to create specular reflection, leading to higher σ_0.
The last parameter is moisture. In reality, it is not the humidity that influences the echo, it is the water content through the change in dielectric constant. The dielectric constant changes the electric characteristic of the surface and thus enhances its capability to reflect the radar signal. When water is in a medium, it will change its conductivity and increases its permittivity. Yet, permittivity characterises the interactions between the electric field of the electromagnetic wave and the molecule constituting the medium. When permittivity increases, σ_0 increases too. The explanation comes from the Frenel law: when an electromagnetic wave runs through a medium, the ratio of the reflected field and the incident field is equal to the ratio of indexes (the transformation between field and power is a square root). In the case of SAR, the indexes in the ratio are the dielectric constants. It is demonstrated that when the medium is wet, this ratio increases and thus, to keep the equality, the reflected power too.

σ_0 is the most used coefficient resulting from the calibration of the images but it is not the only one. β_0 and γ_0 are also two other coefficients that can be used. The difference between them is related to the area used during the calibration (see fig 2.10). γ_0 is a coefficient created to remove the effect of topography by using the local incident angle and making a comparison of images coming from different orbits or tracks possible (Small, 2011).

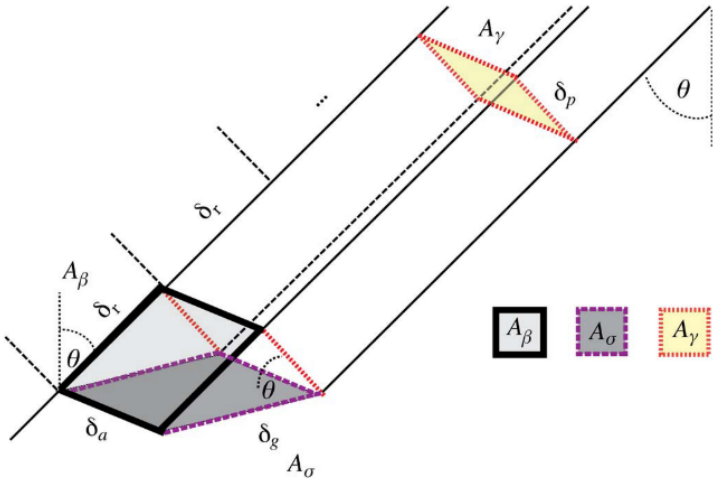

Figure 2.10: Construction of σ_0, β_0 and γ_0 (Small, 2011) The 3 surfaces (A_σ, A_β and $A_\gamma 0$) are the surfaces used to normalise the backscattered energy and create the corresponding coefficient.

After understanding what is displayed in a SAR image, the analysis of the data is still to be done carefully. Active imagery tends to present a great variability between neighbours pixels. This effect of "salt and pepper" is called speckle (fig 2.11). It is caused by the resulting echos created by targets inside the same pixel. The interference is possible because the SAR signal is coherent, it is stable in phase. Then the targets answer inside a pixel can be added together. The sum of the contributions can be very variable between two pixels next to each other as they can randomly be constructive or destructive. Because its mathematical expectancy is null, the speckle effect can be mitigated by two principal means: Spatial and temporal filtering. For example, the multi-looking technique consists of taking the mean of some images of the same scene but taken from different angles. Convolution windows can also be used to mitigate speckle. The bigger the window, the smoother the images but the more loss of information.

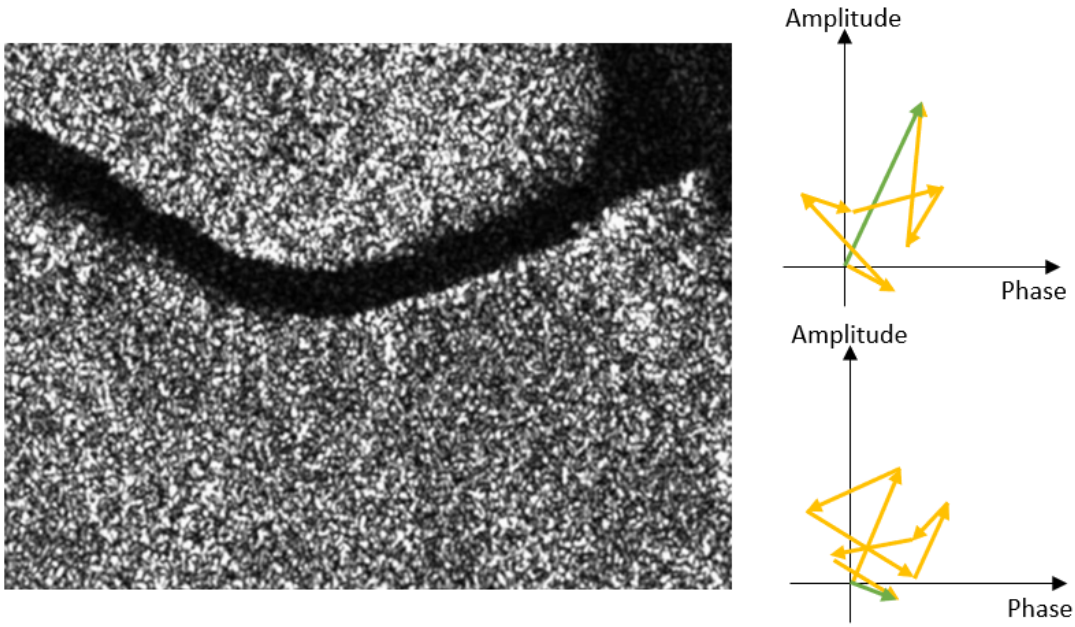

Figure 2.11: Speckle effect in a forest in Gabon. The two graphs represent how constructive and destructive contributions can gave different results.

Polarisation

Polarisation is the direction of the electric field of the electromagnetic wave. Because SAR emits its proper wave, the polarisation of the emitted and the received wave can be chosen. With SAR, it is linear polarisation that is used. There are four ways of using it:

- HH: emitted and received waves are in horizontal polarisation.
- VV: emitted and received waves are in vertical polarisation.
- HV: horizontal polarisation for emitted wave, vertical for the received ones.
- VH: vertical polarisation for emitted wave, horizontal for the received ones.

HH and VV are called parallel polarisations, HV and VH, crossed polarisations. Polarisation is frequently used to segment and classify elements. Anthropological elements tend not to depolarise the electromagnetic wave but vegetation does. Because the depolarised wave is always a fraction of the original, crossed polarisation has a lower mean power. The structure of the target will influence the backscattered energy as horizontal structures will react more with H polarisation and verticals with V. Ratios of polarisation are used to create discriminatory thresholds to create classifications.
The explanations provided here only take into account the amplitude's part of

the complex signal that is the radar signal. Numerous SAR applications use the phase's part. Interferometry is using the difference in phase from several images taken from different positions to study topography or movements. Because interferometry is not used for the master thesis, it will not be developed.

2.4 Melt Detection with SAR

The classification of SAR images is based on the scattering mechanism occurring. Dry snow produces volume scattering and relatively higher σ_0. Meltwater will increase the permittivity of the medium and consequently increase the backscattered power. But it will also make the medium smoother, resulting in a mirror effect and thus a very low σ_0 in the image. In the fig 2.12 the effect is clearly illustrated on the ice shelf. The northern part of the ice shelf gets darker between the two dates. Several ways of creating a discriminant value for SAR images have been developed (Nagler & Rott, 2000; Nagler et al., 2016; Liang et al., 2021; Buchelt et al., 2021; Koskinen et al., 1997). Most of the time, it is not a threshold on σ_0 that is used but a threshold with an index. Depending on the area of the analysis (Greenland, sea ice, Antarctica, ...) the construction of the index and the values of it change. For example, Winebrennernelson et al. (1994) used a flat threshold of -14 dB to study melt in sea ice. Nagler and Rott used a ratio between the images and a reference image of -3 dB (logarithm of a ratio is the difference of the logarithm) in 2000 and a -2dB for the same ratio but weighted proportionally to the polarisation and incidence angle in 2016. Lievens, coordinator of the C-SNOW project at the KU Leuven university, also used a ratio between HV and HH σ_0 in 2019 to study the state of the snowpack (Lievens et al., 2019).
During the redaction of the thesis, two articles on the subject have been published. The first article (Buchelt et al., 2021), used an adaptive threshold in space and time but not in the form of a ratio. The start of the melt season is defined by the lowest backscatter of the season and the study continues until the end of the melt season. As this work is based on the observation of melt, we do not go further. The article states that the optimal threshold differs between the years and the polarisation. The optimal and global way to detect melt would be using a threshold of 4dB, with HV polarisation. Some assumptions had to be made in this case. First, 4dB is a lot more than the -2 and -3 from Nagler (Nagler & Rott, 2000; Nagler et al., 2016) and the paper references threshold of 2 and 3 for the two precedent Nagler's papers cited. The value is thus certainly -4dB. Second, it seems like it is γ_0 that is used in the article. Thus, it cannot be followed as calibrating images

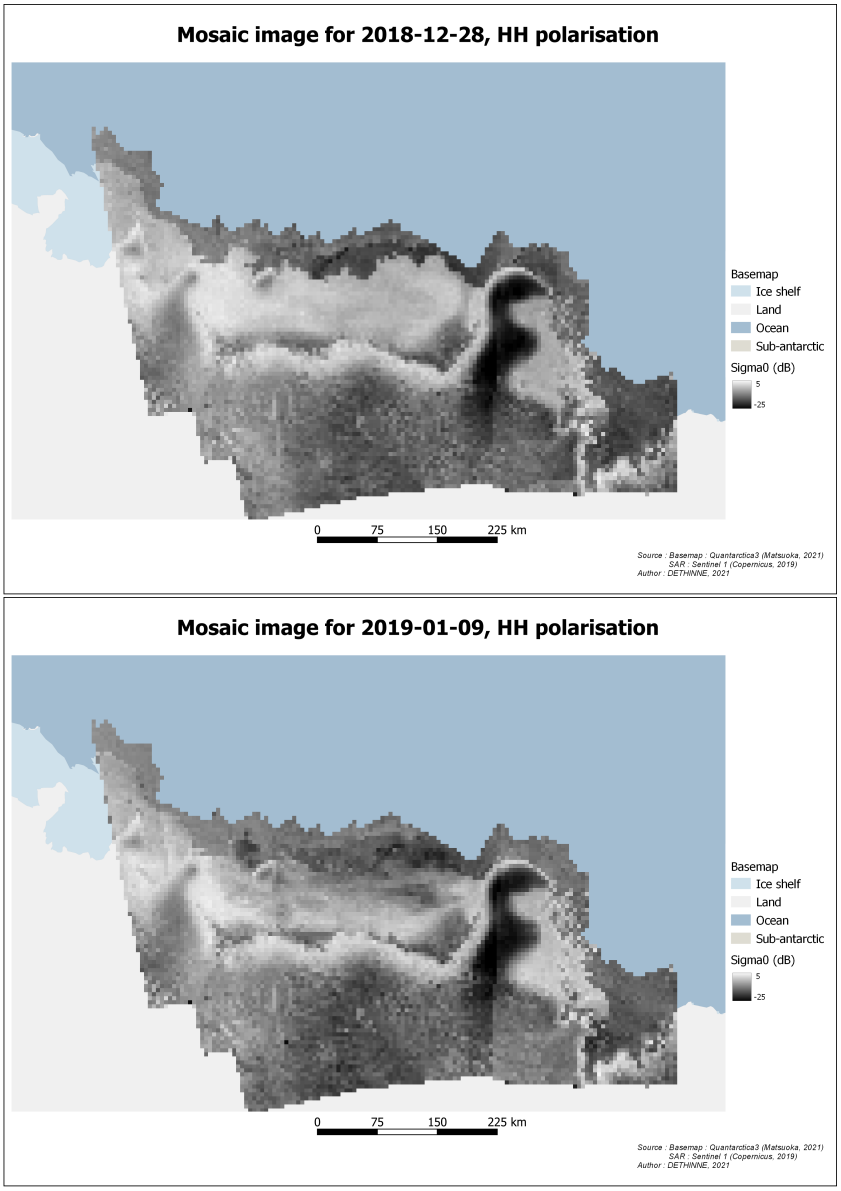

Figure 2.12: Effect of melt water on SAR σ_0. The top picture shows values of σ_0 just before the melt season. The ice shelf appear bright, because the values are high. The bottom one is during melt. The northern part of the ice shelf appear darker, σ_0 have drop with the presence of liquid water.

in γ_0 was too time-consuming and understood late in development. The second paper (Liang et al., 2021) is much more interesting as it is focused on mosaicking Sentinel-1 images over Antarctica and detecting melt in it. The common point with the other papers is that the threshold is based on a ratio. However, the ratio is not really formed with a fixed referenced image. The paper is based on the fact that there is not a lot of events that could cause the backscatter coefficient to change between two dates in Antarctica. Either the change comes from a variation in the geometry acquisition or from *in-situ* characteristics. Summer images

are then normalised with regard to an image from the same orbit, same time of acquisition but in winter when there is no melt. If changes have occurred, the cause is probably melting snow. This type of "co-orbit normalisation" could have been used in this master thesis as it is quite simple to implement, as far as the data are available. Such reasoning allows to clean the images from the darker zone in altitude or would have allowed to better understand what happens in the lake's zones that have a constant low backscatter (see further). In the end, the threshold used in Liang et al. (2021) is -2.66 dB for σ_0 images in HH polarisation.

Chapter 3

Methodology

As explained in the state of the art, using satellites to observe the melt is quite common nowadays. However, using SAR on a larger scale in Antarctica has only been done very recently in Liang et al.(2021). The subject stays quite interesting as it is still a challenge for the programming part as well as for the analysis part. Even more, because the subject links two disciplines, working alone turns out to be almost impossible. Collaboration is needed to create innovations and from innovations comes advancements. By linking glaciology and space sciences, this master thesis tries to contribute to the collective work that prevention and warning on global warming are. It can be by showing each disciple what they could bring to each other and the complementarity of the data. To archive this, the thesis will try to **answer 3 questions: How large the differences between the melt quantity provided by the two product are? Where are located the differences? When are they occurring ?**

In order to obtain the desired results, several steps are required. The first of them is choosing the data that will be used. Some data are more relevant to use than others. For example, as explained before, polarisation can have an impact on SAR data. Once the data is chosen, it needs to be treated. SAR and MAR data do not follow the same structure. One can be seen as a cube of data containing all the necessary information, the other is an assembly of spare data. The structure of the data is a barrier to a simple comparison. You cannot compare things that are not comparable. Transformations need to be applied to match SAR and MAR together. The match needed is in both spatial and temporal dimensions. The solution to this problem has been to create a mosaic with SAR images. The mosaic allows to interpolate SAR data's time to MAR data's time and to merge the information of images of multiple days together.

Once all data are correctly georeferenced, a threshold has to be considered for melt

in SAR. The assumption used is that water in the firn will change its properties. By adding liquid water to a surface that causes volume scattering, it will turn it into a mirror for the waves. Resulting in a lower echo. Such a simple hypothesis makes that noise and other effects can influence SAR to detect melt when there is not. The choice of the threshold can be made in different manners. Here the choice is purely made on previous studies. After all the previous steps, it is possible to compare the data. The comparison is focused on time series and spatial variability. Spatial variability can be studied through maps or index like the Moran index. A lot of precautions had to be taken before a clear and strong comparison. As it has just been said, external events can interact with one of the two data and make them incomparable. In order not to impute miss observations or problems in modelling, critical zones can be masked out of the analysis and explanations of the differences will be discussed when proved to be relevant. Uncertainties bring assumptions and hypothesis that will not be resolved in this work but open the subject to reflection.

Chapter 4

Data Presentation

4.1 MAR

MAR data is composed of NetCDF files. NetCDF is a common format used in climatology for the exchange of data. It can be seen as a documented multidimensional data cube. Two of the dimensions are the X and Y coordinate and another one is the time. Each file contains one of the six variables to be studied. Those variables have similar image size, pixel size and time resolution (see table 4.1). The variables are:

1. WA1: WA1 is the liquid water content of snow layers. The file is divided into ten bounds/layers of snow representing the first meter of depth. The boundaries are: 0cm, 5cm, 10cm, 20cm, 30cm, 40cm, 50cm, 65cm, 80cm and 1m. WA1 can be compared with SAR thanks to the ability of radar frequency to penetrate the soil.

2. RO1: Not a variable representing liquid water, RO1 is the snow density. Divided into the same layers as WA1, it is not used to be compared directly to SAR data. It is used to create a variable that represents the relative quantity of water in the snowpack together with WA1.

3. ME: ME variable is the melt variable. As SAR have strong interactions with liquid water, this variable should be the one that correlates the best with SAR in standardised conditions because melt is supposed to be the major source of water in the snowpack. Further testing will show that it not as simple as it seems.

4. RU: This variable represents the surface runoff. Runoff contains both runoffs caused by melt and by rainwater. SAR backscatter should change with both

of them but it is not the rain that is studied here.

5. SMB: The surface mass balance is linked with ablation phenomena and thus may be correlated with the radar cross-section. SMB is calculated as the thickness change of the snowpack. It can be approximated by the sum of all the processes that cause accumulation or ablation.

6. SU: Sublimation is the passage from solid-state to gas without passing by the liquid phase. If it is the liquid water that is detected with SAR, for the sublimation process to occur, snow needs heat as it is an endothermic reaction. If there is heat, there may be some melting too.

Variable	Unit	Image size	Pixel size	Frequency
WA1	kg/kg	750 · 720 km	5 · 5 km	1/day
RO1	kg/m^3	750 · 720 km	5 · 5 km	1/day
ME	$kg/m^2/day$	750 · 720 km	5 · 5 km	1/day
RU	$kg/m^2/day$	750 · 720 km	5 · 5 km	1/day
SMB	$kg/m^2/day$	750 · 720 km	5 · 5 km	1/day
SU	$kg/m^2/day$	750 · 720 km	5 · 5 km	1/day

Table 4.1: Mar data used.

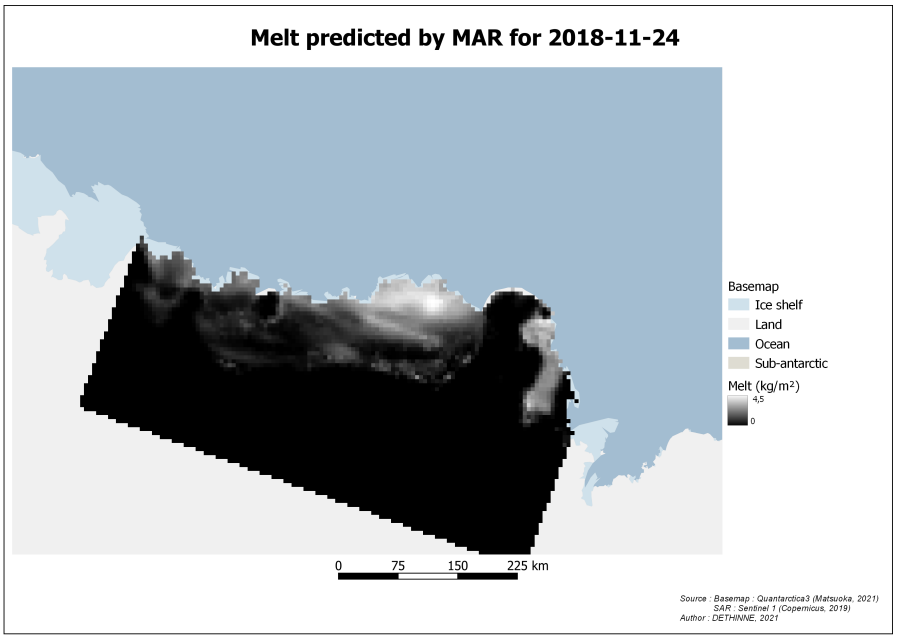

Figure 4.1: Cartography of the MAR variable ME at the date of 2018-11-24.

Multiple variables were provided but they are the only ones being compared with SAR. SAR detects waters and the variables WA1 and ME are perfectly fitting.

Other variables as AL2 (Surface Albedo) could have been taken into account but could not be included in the analysis to stay in the time and length allowed for the thesis.
Available images are centred on the Roi Baudouin ice shelf, once a day since 1^{st} January 2015 until 31^{st} December 2020. The value is a daily mean estimated at noon. Fig 4.1 and 4.2 represent example of ME and WA data for one day.

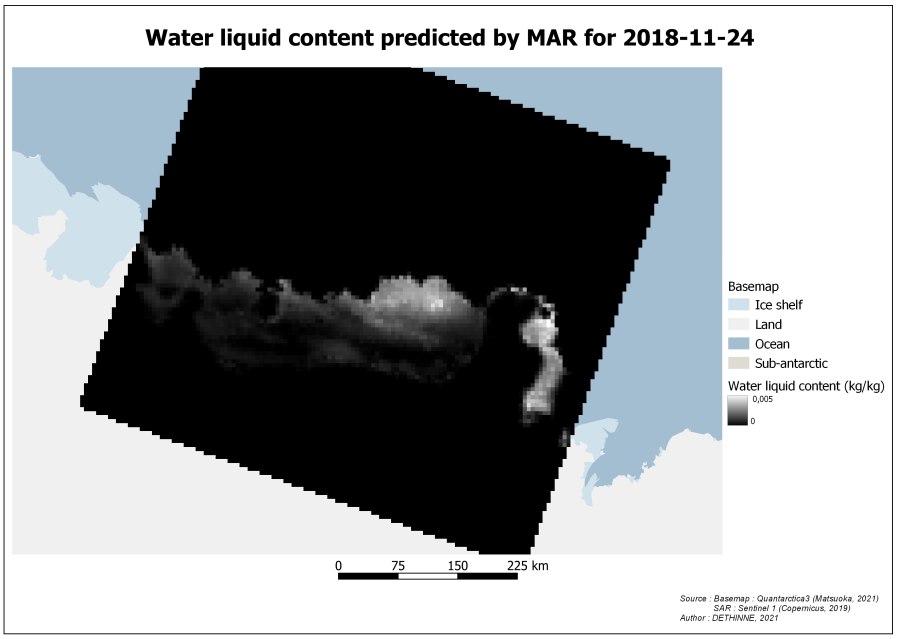

Figure 4.2: Cartography of the MAR variable WA1 at the date of 2018-11-24.

4.2 SAR

SAR images (fig 4.3) used are data from the Sentinel-1 mission. It refers to a constellation of two polar satellites. Sentinel-1 is the first mission the European Space Agency (ESA) is developing for the Copernicus initiative (ESA, 2019). Copernicus brings a paradigm shift in the use of space data. The program aims to provide, free, open-access and high-quality data (Copernicus, 2019). The two satellites constituting the constellation (S1A and S1B) work on the C band, allowing night and day imagery. With an orbit of 693 km, a revisiting time of 12 days and a near-polar sun-synchronous orbit, the S1A and S1B allows having images on a zone every 6 days. The first satellite, S1A, has been launched in April 2014 for a seven years mission. S1B has been launched two years later. In polar regions, polarisation is set on HH + HV or HH and the Interferometric Wide swath (IW) and Extra Wide swath (EW) mode are the two predefined modes of acquisition (ESA, 2019). In

general, the local time of passage of the descendant node is around 6 PM.
The data are retrieved from the Alaska Satellite Facility (ASF, 2021). To have the 6 days revisit time of S1A and S1B and not only the 12 days revisit of S1A, the analysis starts in 2016 and not in 2015 even if the data has been processed for 2015. in the end, 1417 images were used to conduct the analysis. They are described in the complementary material document (see section 8.1). Multiple paths are used to recreate an image of the MAR's data size. Indeed, the coverage of data collected for the paths are different and, to have as much data as possible, they are all taken into account. Still, SAR is the limiting factor comparison wise. MAR output resolution time can be set but SAR has physical limitations. Even if all the data possible is used, some dates show a lack of images resulting in holes within the comparison. Nevertheless, the spatial resolution and pixel size are a lot greater than for MAR. Mostly GRDH and GRDM products are used for this analysis. Such images have a pixel size of 10 by 10m and 40 by 40m respectively (table 4.2).

Polarisation	Coefficient	Swath mode	Pixel size	Frequency
HH	σ_0(dB)	IW and EW	$10 \cdot 10$m and $40 \cdot 40$m	1/6 days
HV	σ_0(dB)	IW and EW	$10 \cdot 10$m and $40 \cdot 40$m	1/6 days

Table 4.2: Type of SAR data used for the analysis.

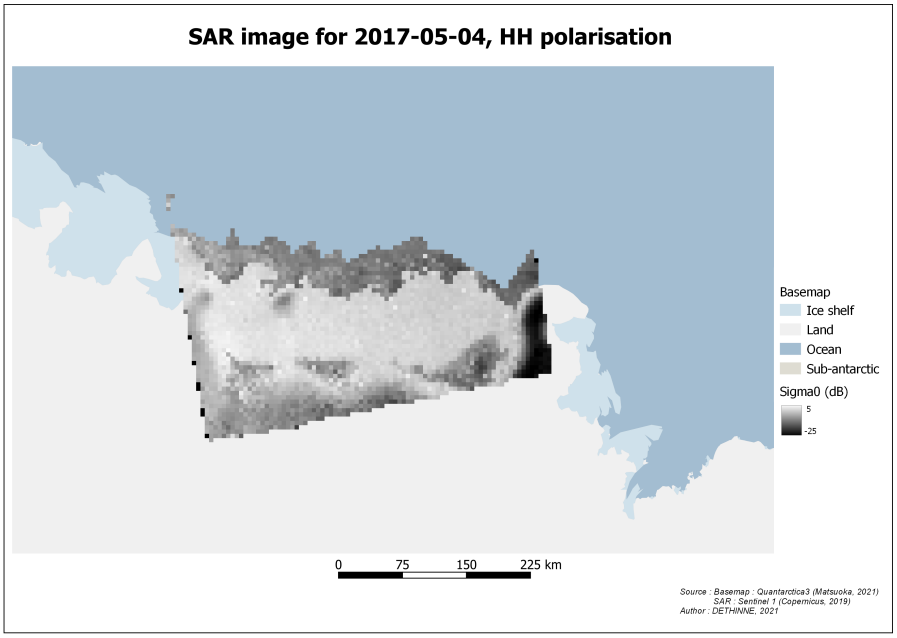

Figure 4.3: SAR image from path 88 after processing.

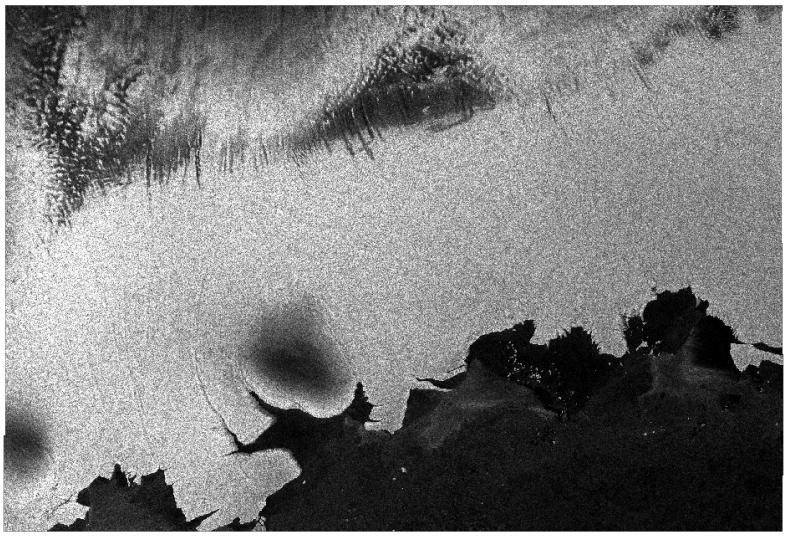

Figure 4.4: SAR image from path 88 without any processing.

Chapter 5

Data Treatment

The data treatment section is about the transformation of original data to readable raster data. The processing is completely different for the two types of images as the one for MAR is hand-made on Python and the one for SAR is made with the ESA SNAP software.
Another goal of the pre-treatment is to obtain georeferenced images with the same pixel size. Pixel size is fixed to 5000m because it is the MAR's basic one. However, as seen before, SAR technology can provide resolution up to 10m and resampling MAR to a greater resolution and downgrading SAR much less could have been an option to benefit from it. Limiting factor as processing time and RAM needed for the computation made the choice of a 5km resolution a fast first approach that does not take full advantages of the SAR potential.

5.1 MAR

MAR data is provided in NetCDF format. Working with .nc format obligates to learn new data's structure that is not usual in basic programming.
The Python script pre-treating M.A.R. is named Extract MAR (see complementary material, 2.1). The algorithm simply checks for every .nc files in a specified directory and create a .tif image for each time value of each file found.

5.1.1 Data Extraction

After several tests with different libraries, Xarray seems to be the best fitting one to read and extract data by opening the file as an array. The choice is mainly based on habits to work with data array rather than with dataset and dimension as NETCDF4 library does.

Because all NetCDF files do not have the same structure, it is not possible to automatically select the right variable. But provided NetCDF files are built with the same structure. It allows defining the first attribute as the studied variable. Thereafter, the data cube is read day by day and the values of the variable for each day is extracted before projecting the data. Slicing the data cube day by day allows working with one dimension in less, which is conceptually more simple.
For a given day, the array storing the variable is distinct according to the studied variable. That is to say, if a variable has layers, the array will be composed of three dimensions (latitude, longitude, value by layer) when it is only two for classical data. In order to recreate a simple 2D map from the 3D array, a weighted mean value of the layers is created by weighting values with the corresponding layer thickness.

5.1.2 Data Projection

Projecting MAR data has been one of the most challenging parts of the work for two reasons. First, as said before, working with NetCDF is not usual and second, because there is not a lot of libraries that help creating geographically referenced images from scratch.
Most of the libraries tend to only work with already projected images and only apply basic operations on them such as clipping or resampling. Another problem that had to be solved was the projection of the data. The .nc is defined with bounding coordinates and posting so each variable is given for every coordinate. However, those coordinates are local coordinates given relatively to the image's centre. Without knowing the centre's coordinates, it is impossible to project (x,y) to longitude and latitude. The only way found to do so was taking the right coordinates from another file with the same extent and copying them into the studied NetCDF file.
Once the (x,y) coordinates are copied, they are projected in longitude and latitude using the Pyproj library. The projection used is the Antarctic Polar stereographic projection (EPSG: 3031) as the studied area is in Antarctica, conventional WGS84 (EPSG: 4326) would not be convenient with all the deformations occurring near the poles. Using Gdal, by providing the proper metadata file, it is possible to create directly the .tiff files projected with the exact coordinates and the values from the NetCDF file.
To confirm the data projection, they are visualised in Qgis, within the Quantarctica project (Matsuoka et al., 2021). Some examples of images created are visible in the previous part.

A frame of No data is created around the data as the output raster is a square but the values are tilted inside. To create this mask, the nearest neighbours (NN) method is used. For each pixel of the new grid, its coordinates are inverted to get the old pixel corresponding. It allows to keep No data in the form of No data and not transforming them into 0 when interpolating the mask coordinates. However, the interpolation method used to get values for the new image is linear interpolation. Using linear interpolation rather than NN allows mitigating the deformations caused by the projection. Linear interpolation will also render a smoother image. Interpolation is made by inverting the new coordinates of a pixel to its position in the old system. The value is then calculated by two linear interpolations between the neighbour pixels (fig 5.1). Cubic interpolation has been ruled out of the projection because it causes spike effects at the margin of the ice shelf or near batches of melt.

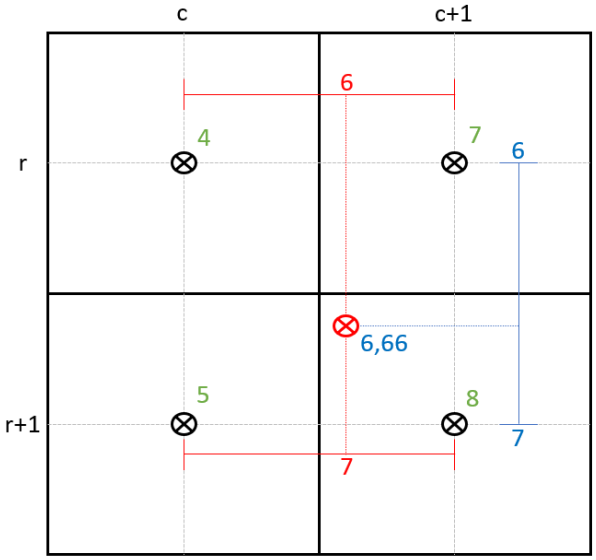

Figure 5.1: Example of linear interpolation. A first interpolation is made between c and c+1 in both rows. Then a second interpolation is made between r and r+1 but with the new values found.

The processing of MAR data files is pretty quick. To create images for one variable, one image a day, from 2015 to 2020 (2192 images) the treatment lasts for approximately 420 seconds.

5.1.3 Melt Binary Classification

Speaking of melt with the MAR variables is a bit of language abuse. Only ME represents melt, other variables are somehow a by-product of liquid water. But,

in order to compare SAR and MAR, some values need to be used as thresholds to permit discretization. For SMB, it seems natural that a threshold on the variable values have a less impact-full meaning as the change in surface mass can be caused by one of the other variables composing SMB than melt. Same for RU as the variable results of a complex interaction between several variables.
For the ME variable, a threshold of 0,1 mm/day is used. Firstly because the linear interpolation use to create the image can cause small values where there should not be. Secondly, because a really small quantity of water does not cause enough change in reflection to be seen in the SAR image.
For the last two variables, RO1 and WA1, a pixel is considered as melt if:

$$0,1 \cdot (0,1 \cdot RO1[k = 1 : 10@ave] \cdot WA1[k = 1 : 10@ave]) > 0,1\% \tag{5.1}$$

With k the snow layer's number. The equation, outcome of a discussion with Mr Fettweis, simply stipulates that melt is considered when the water content of the first meter is superior to 0,1%. However, working with an averaged layer can be problematic. If by using C band, SAR products can penetrate through the first meter of soil, it is only possible when the snow is dry. If the first layer contains enough water, there will be no penetration and σ_0 will be low. But that does not mean that the average on the first meter will be greater than 0,1%. It is then a sensible analysis that as to be made, a lot of considerations have to be taken.

5.2 SAR

For MAR, the major data transformation was the projection of the data. For SAR, the treatment begins earlier in the processing chain. Some more steps have to be applied. Some as speckle filtering are typical to radar imagery, others as under-sampling are more commons. As opposed to MAR pre-processing, SAR pre-processing is more time and resource consuming. Simply when comparing the size of the data before the process: MAR = 6 files, 3 Go; SAR = 1582 files, 537 Go. 1582 files do not mean 1582 images as some files have HH and HV polarisation in them. The quantity and size of data have been a problem for the processing. In order to complete the processing of an image from the beginning to the end, more than 16 Go of RAM were needed. Because the process would take a few minutes by images and the computer used has 32 Giga of RAM, it was not possible to process multiple data at the same time. During the treatment, memory swap (use of virtual memory instead of physical) occurred two or three times, forcing to stop the ongoing process.

Time is a key factor for the choice made. Because I did not have permanent access to the computer at the CSL, it was easier to run a script that compiles in one or two days so it was possible to run another one during the next visit. 3 days were necessary to complete the processing of the 1582 images. It is a one-time process but it had to be done a second time because an error in the calibration graph builder (see next part) caused the majority of the images to be empty. The zone was also restricted to RBIS because of the processing. To cover RBIS, 1582 files are used. To cover the Dronning Maud Land, as discussed in the first instance, it would take more than 13000 images. It was not possible to store them with the storage capacity allocated to the project. Even more, it would have taken weeks to do the processing.

5.2.1 Image Pre-Processing

Image pre-processing is the core of the use of SAR images. The chain of processes that is applied to the images is the same for all the images, as well as for the properties of the processing tools. To simplify the operations, a graph is used (fig 5.2).

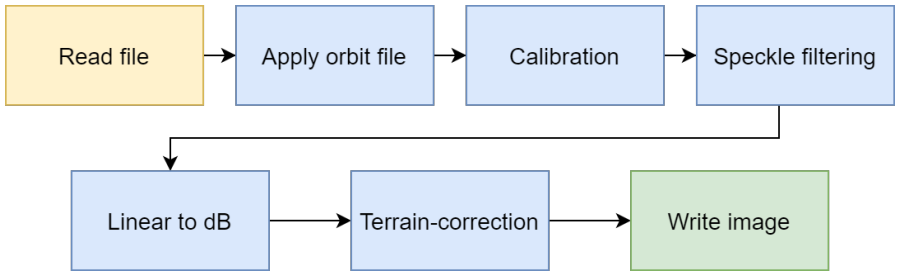

Figure 5.2: Graph builder used to process downloaded SAR images.

The first step is to read the image to process it. The read operation is used to open the files. In original data, orbit metadata are generally not accurate and can be refined. The second step is thus the use of the "Apply-orbit-file" function. More accurate positions and velocity vectors are provided to update the abstracted metadata of the product. All images do not necessarily have a correction to apply. A special input parameter prevents the calibration to stop if there is no file to apply.

The third step is calibration. Snap Help Toolbox informs us on what is done by the function. Uncalibrated images are sufficient for qualitative use but not for quantitative. Indeed, basic SAR image processing does not include radiometric corrections. Without the radiometric corrections, it is not possible to relate the value of a pixel to the radar backscatter of the scene. To simplify the sentence,

it gives a physical meaning to the values recorded by the sensor. The calibration step is also mandatory when measurements of different orbits are used together. The result of the calibration chosen here is σ_0 but it is possible to obtain γ_0 or β_0. However, the processing to obtain γ_0 takes more time and was dismissed. It is also possible to transform β_0 into γ_0 with the terrain flattening operation. The operation is supposed to make the analysis free from topographic effects. The assumption that the ice shelf is flat enough not to have strong topographic effects allows saving some time by using σ_0 directly. A graph that creates data with γ_0 has still been made and is shown in fig 5.3.

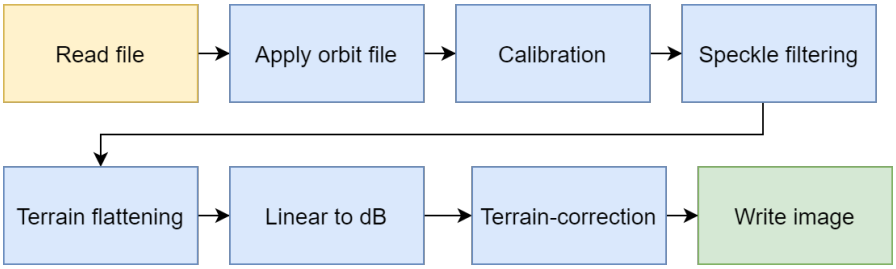

Figure 5.3: Graph builder used to create γ_0 images from downloaded SAR data. Not all the images were processed with this graph as it took too much time.

After calibrating the data, a necessary step for SAR data is speckle filtering. The filtering has the purpose to render a smoother image as explained before (see section 2.3.2). A Lee sigma filter type (Lee et al., 2009) is used with the basic parameters: 1 looks, a $7 \cdot 7$ window, 0,9 σ and a 3 by 3 target window. To reduce the speckle effect, the value attributed to the pixel by the filter is the average value of the neighbours whose value is within +- 2Xσ (standard deviation) of the tested pixel value. The step right after the filter is a simple transformation of the image value into decibels. Swapping linear values to logarithm has the advantage of better describing the small values and bringing the high values together. It is often used in SAR imagery to normalise the value distribution as linear images have a lot of small values and a long tail of higher values.
The last tool used before the creation of the transformed image includes two processes. Terrain correction, or Range Doppler Terrain Correction Operator, corrects the product from the geometrical distortions discussed in the state of the art (Small & Schubert, 2008). The geometrical distortions corrected can come from the topography or the acquisition geometry, as data not directly under the nadir of the sensor is distorted because the pulse has a length. To correct the image and correctly project the pixels on the ellipse, a DEM is required. Usually, SNAP have an automatic DEM download option but it is not accessible in Antarctica, the

software has no terrain model available there. Even if MAR topography is based on the "Bedmap2" DEM, the terrain correction is made with a model from the TanDEM-X mission. The choice made is purely made with report to the resolution of the DEM. TanDEM-X DEM has a 90m pixel size when the other DEM available have a kilometre pixel size.
At the same time, new pixel size is defined during the process. The pixel size is defined to match with MAR data. The resampling method used is bilinear interpolation. By going to a 5km resolution from 10m, a lot of information is lost and bilinear interpolation allows to take more of the values into account when calculating the new ones. In the first approach, resampling was implemented before the terrain correction to reduce the processing time. However, in certain cases, the data resulting from the processing chain would be filled with 0. There was no clear information on why it would do it so it was removed from the chain. In the end, a corrected, resampled and masked over the sea image is produced.
After this last step, the output image is renamed and registered. After the processing, the storage size of the images is greatly reduced. The diminution from 500 Go to 150 Mo is explained by the change in pixel size.
As there is a lot of images to be processed, it is not the desktop application from SNAP that is used but the engine. It means that it is not the application that is used to process the images but directly the macro-commands. The graph builder is a .XML files so it is possible to change its content. By using a .sh files, it is possible to change the directory for the input files as well as for the output files. Looping automatically on all the files rather than doing it by hand is then possible. Without this possibility, it would have been almost impossible to process that much data alone.

5.2.2 Mosaicking

As there is not a single SAR image that covers the entire continent, data are combined to create larger images. Combining the images also allows to interpolates the values to a certain date, at a certain hour. The creation of the mosaic is hand-made on python, using a few libraries to extract the data from the layers. The script Grid Creation contains the definition of a class named gridding (see complementary material, 2.3). The creation of the mosaic is based on this class. Another advantage of mosaicking the SAR images is that it allows a perfect co-registration with the MAR data. Indeed, the coordinates of the new pixels are based on the MAR's ones.
The principle behind the mosaic is quite simple but has taken a long time before

resulting in acceptable data quality. At first, a grid of point is created with Qgis on the zone the images have to be merged (fig 5.4). Then a first date is fixed and the images 12 days before that date and 12 days after are used to create a new image, interpolated in time (fig 5.5). The grid is created with Qgis only to have directly a visual representation of it and matching perfectly with the MAR data but it could have been done in Python too. The main library used to work in Python,

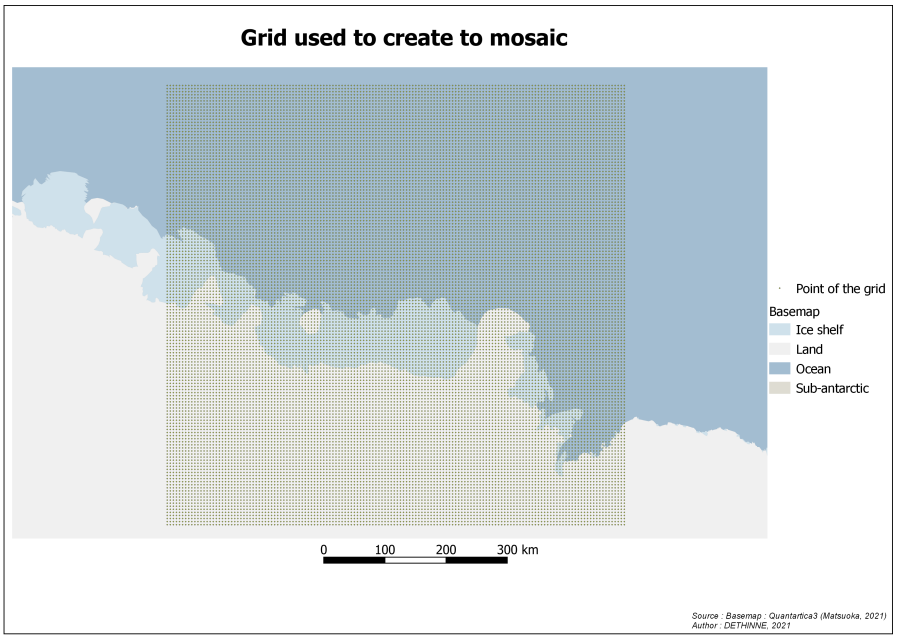

Figure 5.4: Point of the grid used to create the mosaic. Points are separated by 5km to keep the resolution. That is to say that a point is created in the middle of each pixel of a MAR data image.

as for a lot of scripts, is NumPy (C. R. Harris et al., 2020). Data extraction is made with the rasterstats library. The main objective of the script was to have a program that can work with provided tiff. This was made so even if MAR needed to be merged it can be done easily. That is why the functions used are as general as possible.

The script that needs to be run to create the mosaic (fig 5.6) is "Creation of Mosaic" (see complementary material, 2.4). The use of a second script to create the images is needed for being able to have the process in a separate file. As explained the script do the exact same action (so there is a loop) for every six days from the start date until it reaches the last image or a specified last date. In order not to create the grid object for each date, it is a dictionary that is created and substituted to the grid's one. The research for the values of the 12 previous and next dates is poorly optimised. The value of each grid point for each day is stored in the dictionary. This means that each point of the grid is registered even

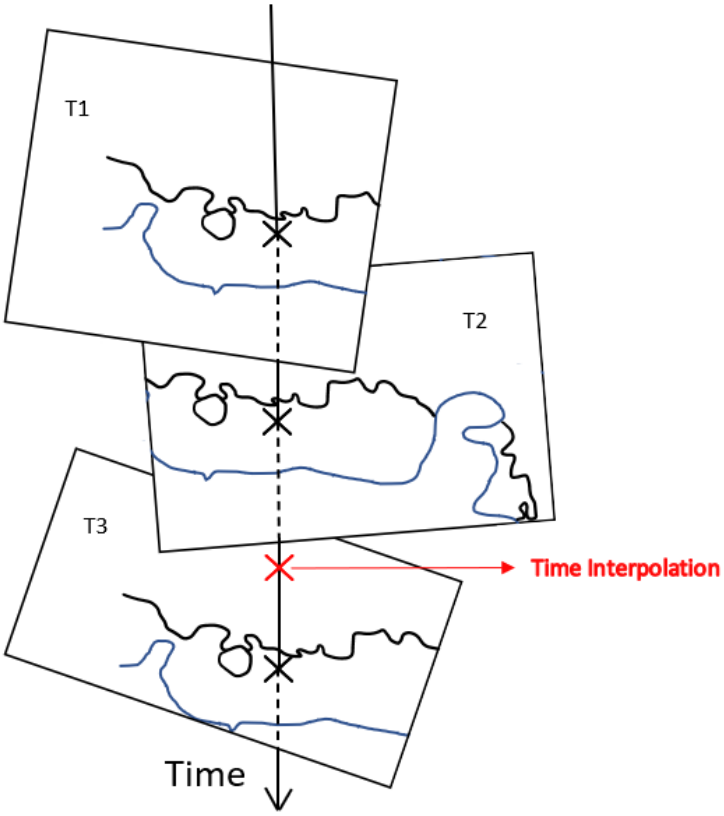

Figure 5.5: Time interpolation. For each point of the grid (fig 5.4), a new value is interpolated between all the images available for the interpolation. The figure tries to represent the axe the interpolation is made along, time.

if it is No data or a lot outside the studied area. Even more, by switching to the other date, the dictionary is reset and days that have already been analysed are erased and need to be analysed again. Those problems could have been prevented by clipping the SHP that represents the grid or just selecting the points that fall in the studied area (with the plumb line algorithm for example) and by only erasing the days that are not in the new interval and analysing the new days.

Once the data for the twenty-four days have been read, an algorithm performing binary search selects the first day before the date of the created mosaic and the one right after. If there are no images in the 12 previous or next days, it is the two closest images to the mosaic date that are selected for extrapolation. The two values and their timestamps are used to interpolate the value for the mosaic. As it is a pixel-wise analysis, the values of the neighbours are not taken into account, resulting in visible boundaries. The interpolation is made so the value of the mosaic is given for noon as the MAR data is. However, all the SAR images of RBIS are acquired near 6 PM. The daily variation is then not represented in the

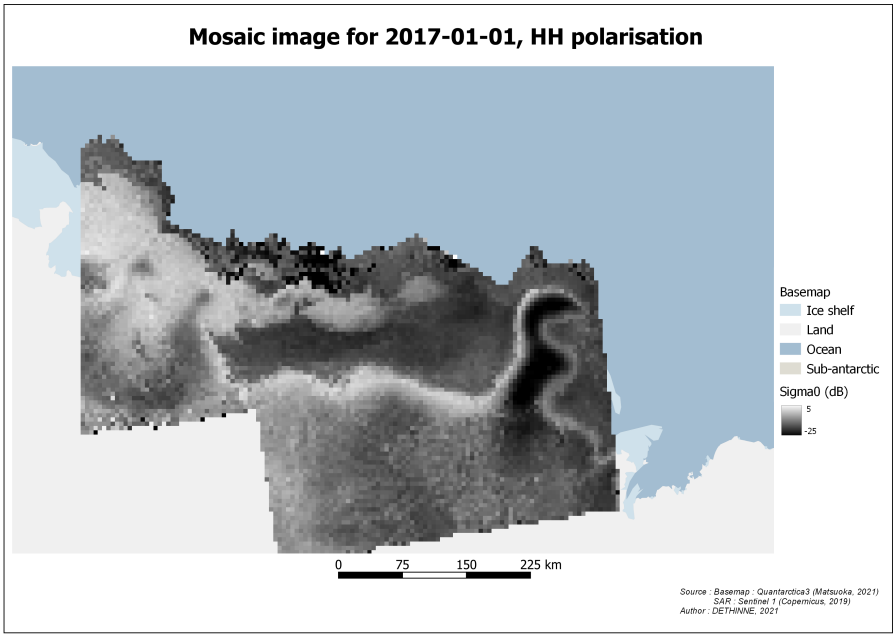

Figure 5.6: Image created with the mosaic script. The figure represents the mosaic created in the form of a map. Most of the errors are located in the sea that is removed later in the process.

data and a significant variation can be overseen (fig 5.7). However, the day cycle in the poles is less important and could be insignificant. It is a linear interpolation and not a quadratic or cubic. The used "iterp1d" function from the Scipy library only required two values for the interpolation when the other need at least three. This condition is not always fulfilled.
Created images have some problems that have not completely been solved:

1. There are holes in the images.
2. Boundaries are not smooth all the time.
3. There are some erratic pixels.

The first problem comes from data availability. A value is interpolated only if there are at least two images in the twenty-four days interval. Then some pixels only have one value and are not interpolated. Creating the mosaic on the same day path 59 or 88 is acquired could allow having an image over the ice shelf. Using this value as backup values could work. This solution is only useful for this situation and has been modified by having the mosaic date just between the date of path 59 and 88. The number of holes and missing values in the images is quite too big. After some researches, it seems like there was a computer problem making the communication between the machine downloading the SAR data and the data provider discontinuous. Images are then missing from the analysis because they

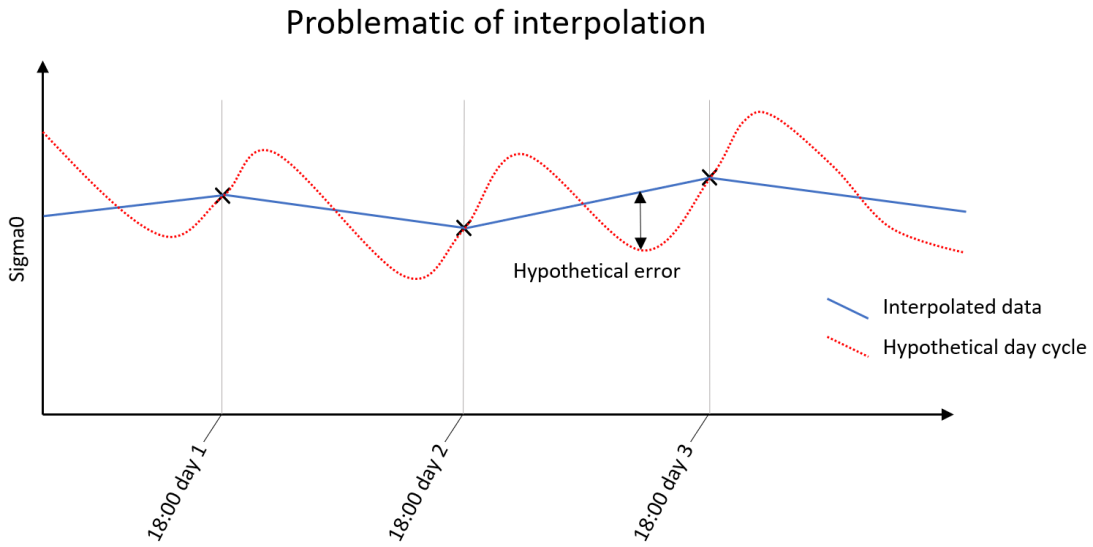

Figure 5.7: Day cycle. Linear interpolation is often performed between two acquisitions at the same hour. When interpolating the value at noon, an hypothetical daily variation can be overseen. Having MAR data at 18h, time of SAR acquisition could have help mitigating the potential error.

were not downloaded. This discovery was made late and only partially corrected by downloading path 88 and 59 from another computer. For the second problem, the function calculating the new values is not the same at all places as the images data varies upon the area. It causes batches of values of different order in the same images. To reduce the difference between the clusters of different values, a convolution window could be used to mitigate the boundaries. It was not used as, most of the time, the ice shelf values are often interpolated between two images that do not cut it. The erratic pixels are caused by side effects. Pixels at the edge of the base images may have unrealistic values. When it is a 10m by 10m pixel in a hundred-kilometre size image, it is not visible. During the under-sampling, some of those pixels stayed. Not to take them into account, a pixel value is not taken into the interpolation if its value is greater than 20 dB or lower than -30 dB. However, it happens that a pixel has a value just under that threshold and is taken into account for the interpolation or worst, for extrapolation. Convolution windows or using the neighbourhood during the processing could eliminate them. The problems are illustrated in the images in fig 5.8.

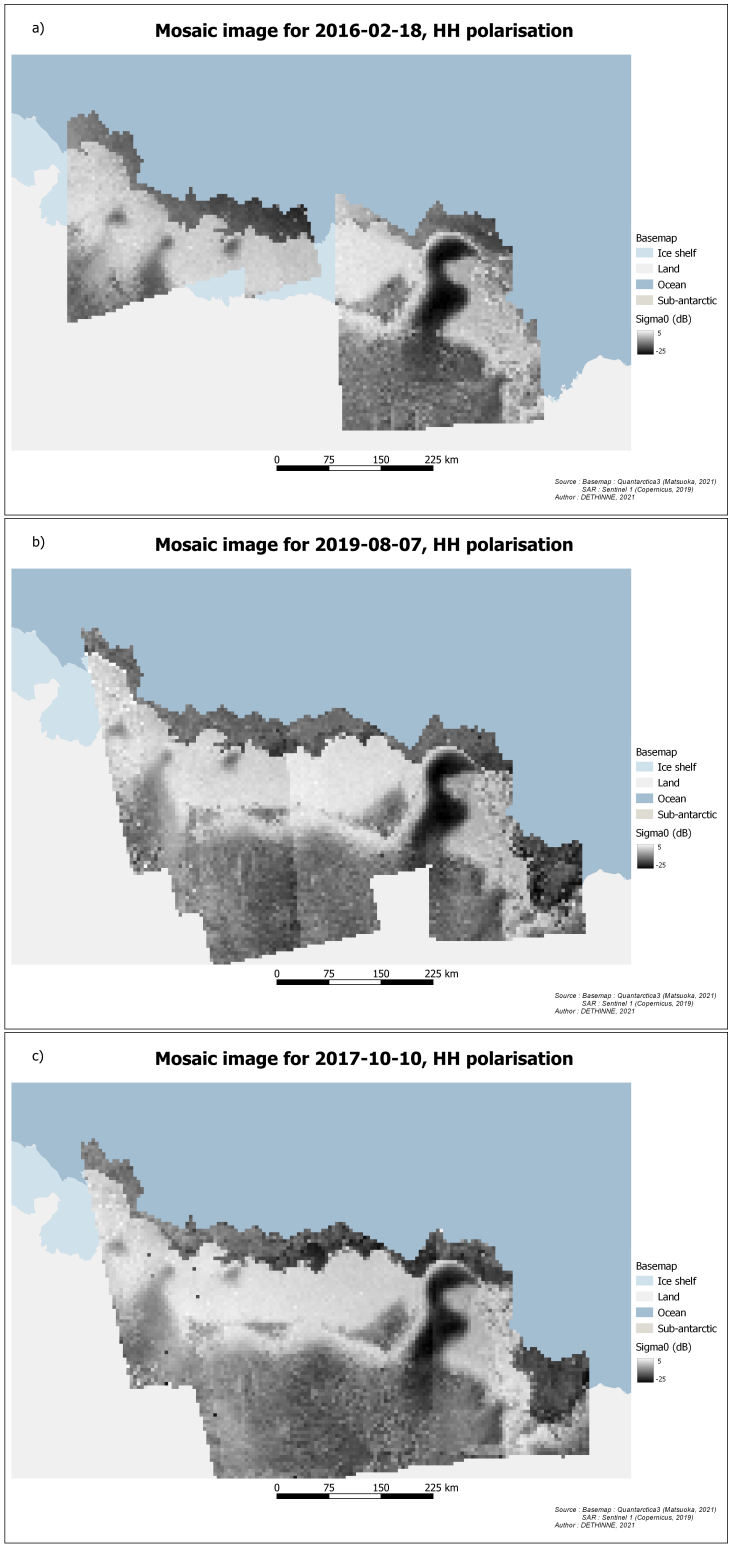

Figure 5.8: Different types of error that can be seen in mosaics. Image a) is the most visible error, the lack of data. When there are holes in SAR image, the comparison cannot be processed. More clear in other location than on the ice shelf, figure b) represents a boundary between two images composing the mosaic. The change in σ_0 can affect the repatriation of melt. By setting the date of the mosaic between the acquisition of path 88 and 59, there are only a few visible boundaries on the ice shelf. c) Is the most common error, erratic pixels. Most of the time, they are caused by wrong values at the hedges of original SAR data.

By under-sampling and interpolating the values, some effects are mitigated. Speckle, orbit and topography effects are reduced. Making some hypothesis less sensitive. Despite the measures taken, 3 images present irregularities that make them unusable. The images are for 2016/06/23, 2017/03/26 and 2017/04/01. Usually, the erratic pixels and the extrapolation problem are in the water or near the coast. However, for the three dates stated, there are too many problems inside the ice shelf to use them.
As explained before, the scripts are not optimised. A total of more than 30 hours is needed to create all the mosaics. Starting from first January 2016 to the last day of 2020, 521 images in tiff format are created. In the 521 images, 304 are with HH polarisation and 217 with HV. The difference comes from the fact that HV polarisation was available only since mid-2017. The images can be found in an annexe document.

5.2.3 Melt Binary Classification

After a long time of questioning and reading the literature, the choice of using a value of -2.6 dB as a threshold has been made. There was no external data to calibrate the melt with and "co-orbit normalisation" was understood too late to apply it. It is a quite simple but time and resource-consuming algorithm. For the normalisation to be efficient, it would have to be made on the not under-sampled data. Doing it after the creation of the mosaic is less impactful as there already has generalisation of the situation (interpolation, orbit mixing, and so forth). Choosing to interpolate SAR data to the time of MAR data may not have been the right way of managing the data. The mosaic and the interpolation of SAR σ_0 was in the first intention to create a SAR image that could cover the whole Dronning Maud Land. As there would have been the obligation to combine images from more than one orbit and day, the creation of the mosaic has a sense. Here, path 88 offers an image of the RBIS with 6 days revisit-time since the end of 2016. Using the only path 88 could have permitted the analysis on RBIS by taking MAR output at the time and date of the SAR images rather than doing the opposite.
Anyway, the goal is still to provide ways to compare SAR and MAR so the processing of the data is made as it would be done for a larger zone. The -2.6 value is chosen relatively close to value in Liang et al. (2021) but rounded to the lower value to be closer to the mean of -2 and -3 proposed by Nagler and Rott (2000 and 2016). The use of a basic σ_0 instead of a ration is not too problematic as the value of σ_0 on the ice shelf during summer is often included in [-1;1] dB as seen in fig 5.9. The threshold should be low enough not to cause false positives.

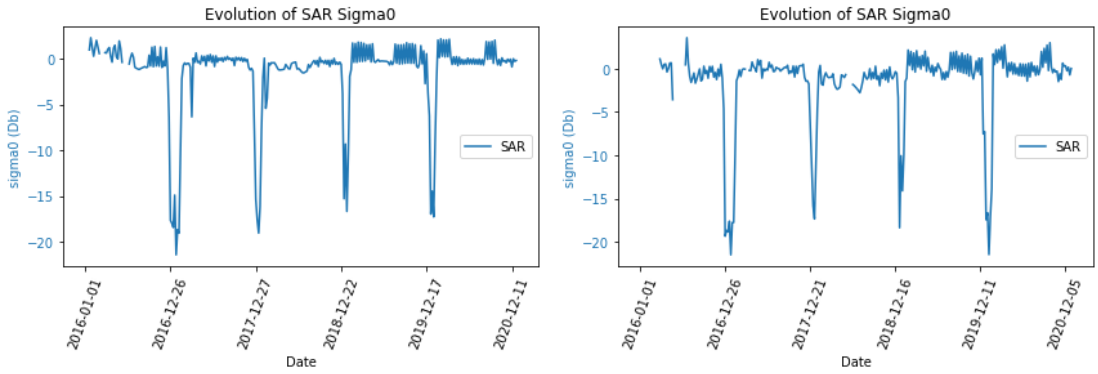

Figure 5.9: Evolution of SAR σ_0 during the studied period. The left graph is the evolution of the coefficient inside a smaller section of the ice shelf (figure 6.3). The second is the mean value of the ice shelf. Outside the melt season, there are small variations caused by the use of several orbits but the value stays close to 0.

In fig 5.6, most of the image appear in black. The low backscatter coefficient does not imply melt in all the scene. Indeed, the assumptions made are only valid on the ice shelf as there is no image normalisation. The -2.6 threshold is used to describe a decrease in backscattering for a zone that present positive or near 0 σ_0 in summer. But an object can have a low backscatter coefficient for another reason than the presence of water. In this manner, from a certain altitude and if the temperature is low enough, the surface is made of dry snow. The particle size of that snow is much smaller than the wavelength of the C-band used by Sentinel-1. The electromagnetic wave passes through it and exhibits a low backscattering coefficient (Liang et al., 2021). In contrast, if the ice shelf has higher σ_0, it is because melt and freeze occur depending on the season. The refreezing generates a large amount of ice with larger crystals. The size of these crystals matches with C-band, resulting in more scattering (Liang et al., 2021). Other zones with constantly low σ_0 are the three blue ice-covered areas on the ice shelf, just before the hillslope. Two hypotheses are made upon the low σ_0 there. The first is based on the information brings by Lenaerts et al.(2016). The sites are full of sub-glacial lakes. The presence of lakes can support the low backscatter as they act the same as liquid water. The "co-orbit normalisation" could prove this hypothesis. If it is perennial water, more meltwater would not give a significantly lower σ_0. The second hypothesis is based on the reunited data from the Quantarctica project. Even if there is a little shift, the 3 zones match with batches of blue ice (Hui et al., 2014) (fig 5.10). Characteristics of blue ice could provide fewer interactions with the radar signal. It stays an assumption as it is not verified in the course of this work.

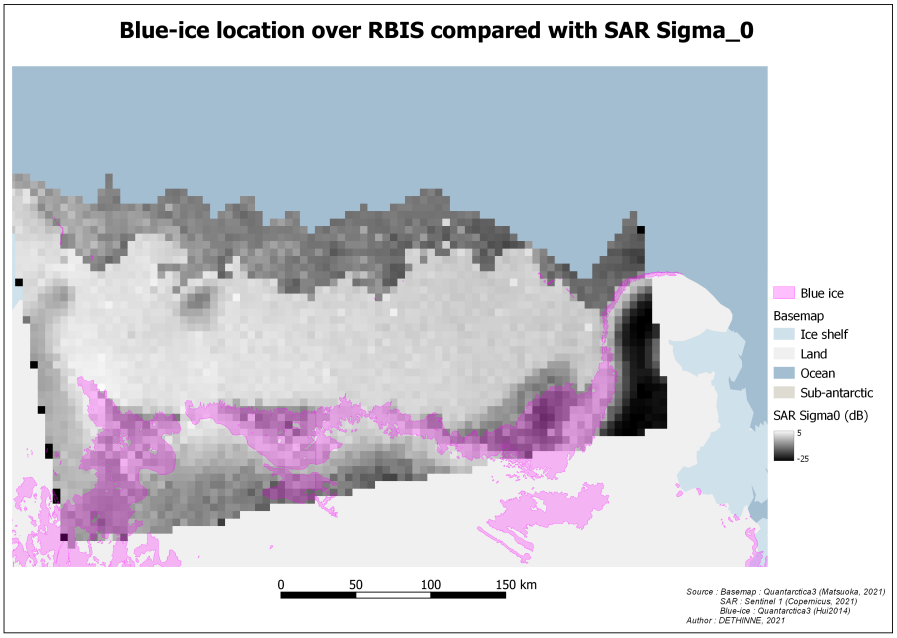

Figure 5.10: Location of blue ice according to Hui et al.(2014). Even if there is a small shift with the 3 clusters of lower values of σ_0, the location of both seems to match well.

5.3 Time Series

There are two types of time series that are built to study the evolution during time. They are constructed in the same way but with two different scripts. The first one is the simplest of the two and is created with the script Creation of Time-Series 1 (see complementary material, 2.7). The graph illustrates the variation of σ_0 and a MAR variable (fig 5.11). The values to be represented can either be the mean values of the image, the mean value of a zone or the value of a selected point. For SAR imagery, following the evolution of a single point is not always the best choice to summarise the evolution during time. Indeed, even if a filter is used, speckle can cause values to show undesired variations. This type of time series is used to compare the evolution without the influence of a threshold. To create it, every point of the defined zone is sampled and a mean value is calculated.
The second type of graph is a bit more complex. It represents the evolution of the percentage of the image that is covered by melt (fig 5.12). The script Creation of Time-Series 2 (see complementary material, 2.8) uses the comparison images to create the graphs. The construction of these images is explained in the next part. The script loops on each pixel of the image or the defined zone and counts how many pixels are under the SAR threshold and how many are over the MAR threshold. The count is divided by the total numbers of pixels. As some images are missing data, the values can be abnormally high or low. Unlike the previous

time series, this one is strongly influenced by the threshold choice.

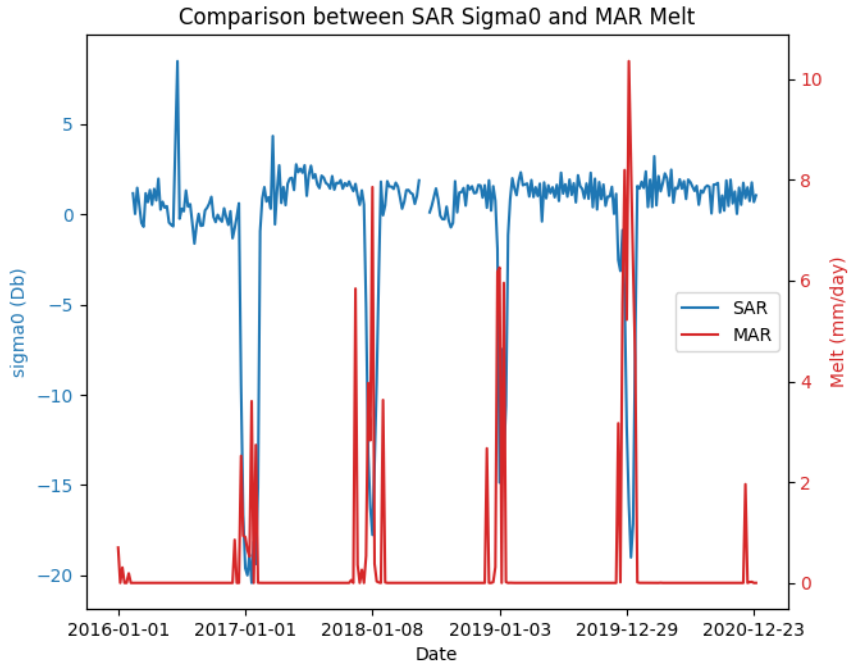

Figure 5.11: Evolution graph of SAR σ_0 and MAR ME.

In some graph, the line representing data is cut. There are two reasons for this. SAR data depends on the availability of the image, no image equals no mosaic equals no data for a date or a short period. But it can also come from the images removed from the analysis because they have too many problems with the interpolation.

5.4 Spatial Analysis

In geography a principle is often used: everything is related but closer objects tend to be more related than remote ones. In general, the concept of spatial autocorrelation is put forward to demonstrate the hypothesis. The term spatial expresses the consideration of the neighbourhood and autocorrelation the correlation of the variable with itself (Goodchild, 1986). To study the spatial distribution of the phenomenon, maps and indexes are used. Comparison maps were the first to be made. They were used to study the evolution 6 days by 6 days and have an easier visual interpretation. With one image every 6 days, for 4 years, with 5 variables to compare, there are 1525 maps only for HH polarisation. It was possible to create short videos of the maps to better study the time variation.

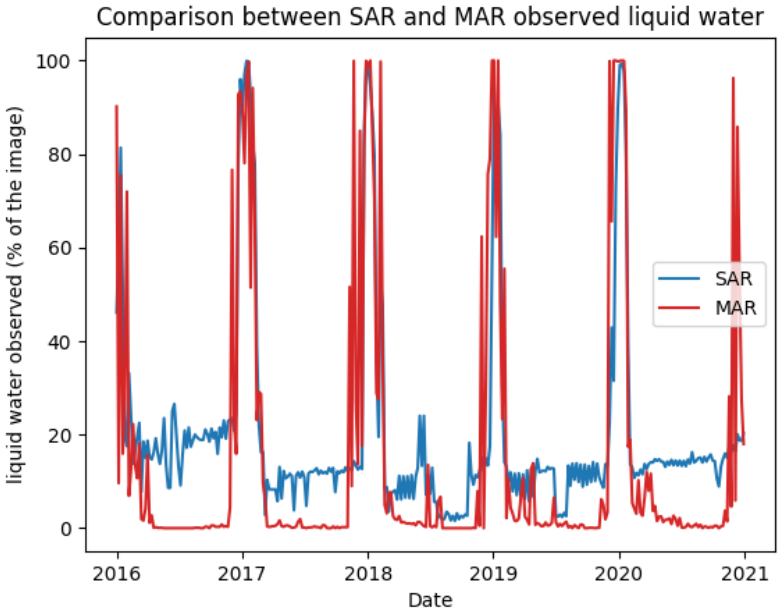

Figure 5.12: Evolution graph of the detected melt and modelled melt.

Comparison maps (fig 5.13) are created through the "Creation of Comparison Maps data" script (see complementary material, 2.5). SAR and MAR data have been perfectly co-registered and the grid used to sample the value is exactly the same. Keeping the values that are outside the mosaic as well as No-data allows an easier treatment in this part. The zip function in Python allows parallel iterations on multiple data tables. As each value of the grid will be iterate, there is no need to keep the ID of the point tested: ID = index of the iteration, making the re-projection of the data easier.
A pixel-wise comparison is made between SAR and MAR. Depending on the value of SAR and MAR, 4 cases represent by 4 qualitative outputs can be identified:

- SAR => th_{SAR} and MAR <= th_{MAR}: No melt/liquid water is detected in both pixel
- SAR < th_{SAR} and MAR > th_{MAR}: Melt/liquid water is detected in both pixel
- SAR => th_{SAR} and MAR > th_{MAR}: Melt/liquid water is only detected by MAR
- SAR < th_{SAR} and MAR >= th_{MAR}: Melt/liquid water is only detected by SAR

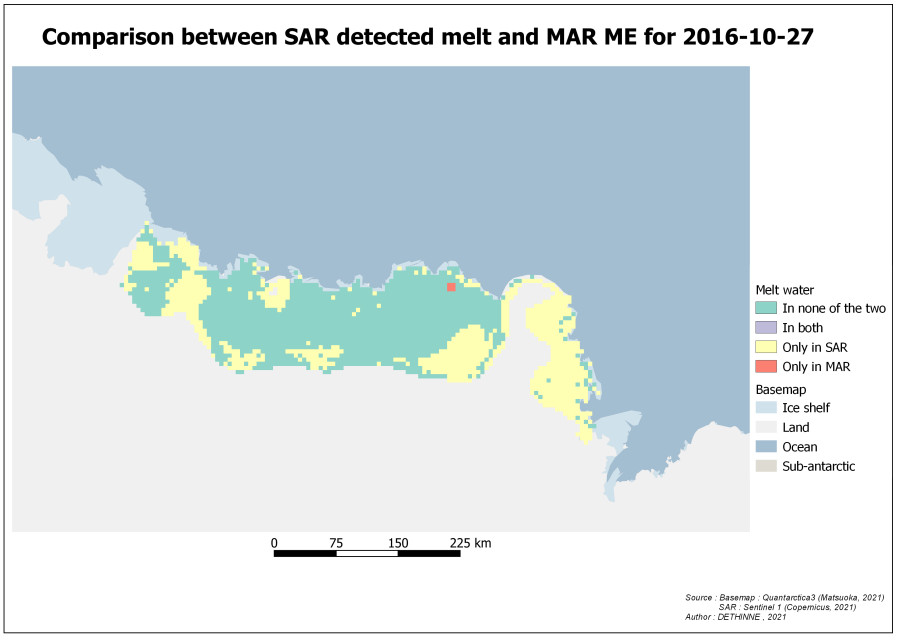

Figure 5.13: Example of a comparison map created. The variable compared are SAR σ_0 and MAR ME.

In practice, values of either 0,1,3 or 4 are assigned to pixels, depending on which of the four cases they fall in. The output raster is thus filled with those four values. The establishment of the maps was not done by hand as it would have taken hours and hours. The python console integrated into Qgis allowed the creation of all maps. The implementation of the script (Creation of Comparison Maps in Qgis, see complementary material, 2.6) was laborious. The class and methods from the PyQgis library are a bit hard to handle for a new user. To reduce the time spend on the script and accelerate the implementation, some short-cuts are taken. The layout is predefined in a template (.qpt) and only the title and the raster to be represented are changed with the script. Style files (.qml) are used to give the right colours to the base map and raster. The raster's style file can be seen as a look-up table in which the 0,1,3 and 4 values are linked to the qualitative meaning as well as a colour palette for the graphic representation.

Two other types of maps are created on the same pattern: a first representing the correlation between σ_0 and the MAR variable, a second representing probabilities. The correlation coefficient, based and the covariance, evaluates how two variables simultaneously evolve. The coefficient is ranging from -1 to 1, the closest to the units, the strongest the correlation. A negative coefficient is expected as when melt quantity grows, backscatter decreases. For the probabilities, two are calculated: the probability of having SAR and MAR giving the same information for the pixel and the probability of melt being modelled by MAR, knowing SAR has detected

melt. The probabilities are simply computed following probabilities rules with data being the sum of all observations during the studied period. The probability of both pixels giving the same information is:

$$P(x) = \frac{\#0\&1}{\#days} \tag{5.2}$$

The probability for MAR modelling melt knowing SAR detects it is:

$$P(MAR|SAR) = \frac{P(MAR \cap SAR)}{P(SAR)} \tag{5.3}$$

This type of conditional probability is used to express the link between SAR and MAR. A high probability will states that when SAR has detected water, there is a great chance that MAR will have too. However, high probability does not confirm that they are perfectly linked. As if MAR always models melting, P(MAR ∩ SAR) will be higher but does not mean that it corresponds well with SAR.
In the same way as comparison maps, they are constructed by looping on each pixel values but by calculating an index over the years and not for every day. The choice of thresholds also influences the values and can change the result and the interpretation that is made out of it. The three maps are constructed with the script Creation of the Spatial Analysis Data (see complementary material, 2.9). The compilation time is a bit long as for the previously explained comparison script. The timing is explained by the number of loops that are used when they could have been simple linear operations.
The statistical significance of the spatial variation of the variable is demonstrated with two well known indexes: Moran's I and local Morans's I (LISA: Local Indicator for spatial association). Moran's I compares a local spatial covariance with the global variance of the same variable (Goodchild, 1986):

$$I = \frac{n \sum_i^n \sum_j^n w_{i,j}(x_i - \overline{x})(x_j - \overline{x})}{W \sum_i^n (x_i - \overline{x})^2} \tag{5.4}$$

The formula is inspired by the correlation's one but the ratio is weighted. The weight W is a matrix taking the topology into account. There are two main ways of considering contiguity for the matrix: rook and queen (fig 5.14). Rook contiguity simply means neighbour by one side when Queen is by one point. Different orders of contiguity can also be used. The order of contiguity means the order of the neighbours to take into account. Direct neighbours = first order, neighbours of first order of first-order neighbours = second order and so forth.

The value of I can be either positive or negative. A positive I is a witness of similar

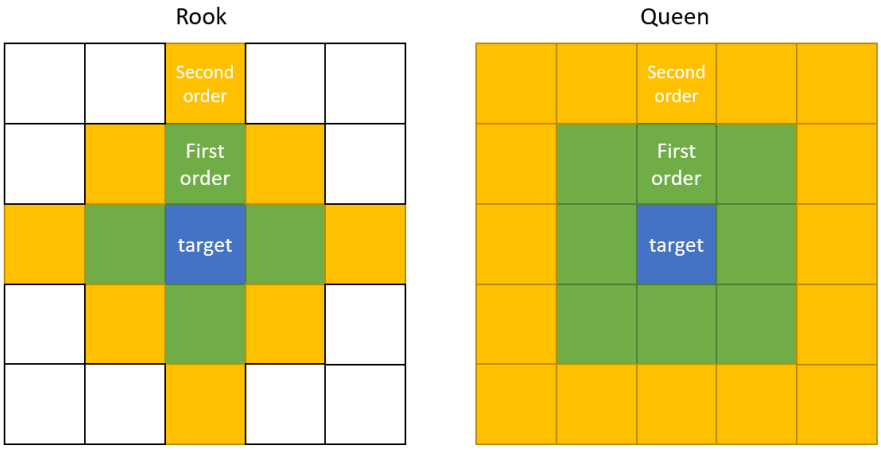

Figure 5.14: Schematics of the two types of contiguity. Left is rook and right is queen. Pixels in blue are the pixel the neighbourhood is defined, green is for neighbours of first order and yellow for the second order.

values being close to each other and negative when they tend to be dissimilar. A zero value is a synonym of independents and randomly arranged values. Moran's I statistical significance is tested by permuting randomly the values of the entities. If the same Moran's I is found regardless of the position of the values, the absence of spatial autocorrelation is retained. On the opposite, if the value is found only in that case, spatial autocorrelation is concluded as significant.
LISA index is no more than the calculus of the I but for one entity instead of the I for all of them. The formula is thus similar:

$$I_i = \frac{n(x_i - \overline{x}) \sum_j^n w_{i,j}(x_j - \overline{x})}{\sum_j^n (x_j - \overline{x})^2} \tag{5.5}$$

In other words, the sum of the I_i divided by the number of entity is equal to the global Moran's I. The advantage of LISA is that it can be mapped and shows where the strongest and lowest autocorrelation occur.
Together with the index, the Moran scatterplot represents the autocorrelation. The plot consists of four quadrants separated by X and Y axes. The X axe is the standardised value of the pixel ($\frac{(x-\overline{x})}{\sigma}$) and Y the mean standardised value of the neighbourhoods. The interpretation of the scatterplot is done by looking at the quadrant of each point or by the linear regression line. For the first (third) quadrant, X and Y positive (negative) are synonymous with positive autocorrelation (high (low) value entity in the middle of high (low) values). Entities located in the first quadrant are called "high-high" and "low-low" when in the third. For the second (fourth) quadrant, X negative (positive) and Y positive (negative), for

their part, are synonymous with negative autocorrelation ((low (high) value entity in the middle of low (high) values). The slope of the linear regression line is proportional to the Moran's I.
The processing of Moran is not completely automated in a script. An open-source software, Geoda, is used to create the weight matrix and perform the Moran's I. However, the software required a shapefile and the data is in a raster form. Once again, Qgis is used to vectorize the data in the form of a shapefile. Defining the neighbourhood of a point through boundaries may prove to be impossible as a point is in 0D. It is then a distance threshold that is used if the data is recorded as points.

Chapter 6

Comparison

Being able to compare the two sets of data is the results of a complex road. SAR images and MAR needed different treatments and approaches. This normalisation step took more time than expected due to multiple reasons as a lack of knowledge that needed to be caught up or the quantity of data. Following the advice of the people helping me, Quentin Glaude, Charles Amory and Christoph Kittel, it has been decided to apply a mask on the zone studied for the two time series in graph form. As explained before, there are some zones that present particularities concerning the radar backscatter. The zone was then limited to 400m of altitude (as temperature get lower in altitude, there should not have melt there) and even reduce to the ice shelf limit given in the Quantarctica project.

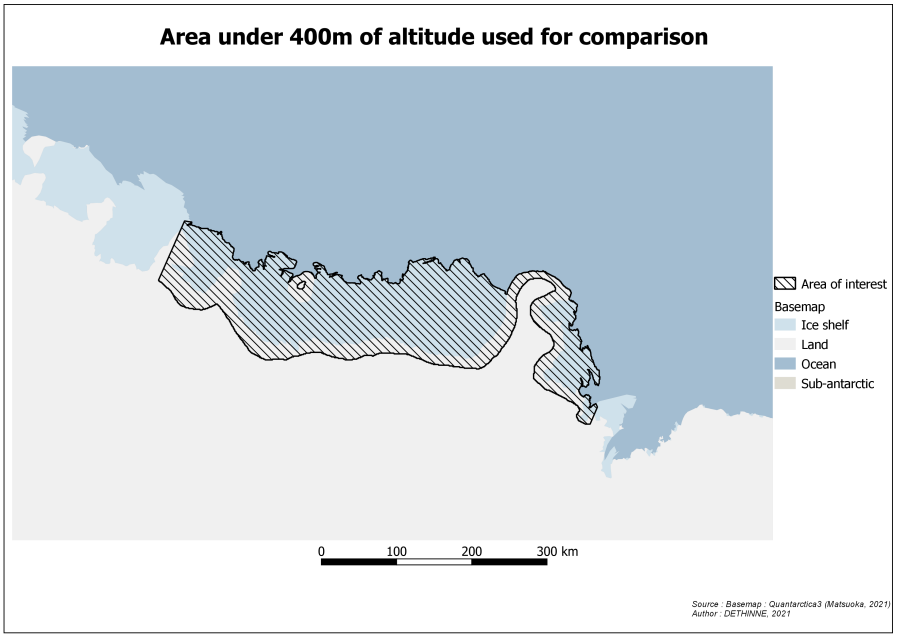

Figure 6.1: Area used to create the comparison maps. The area is limited to all land under 400m of altitude.

The first cut to 400m is kept to create the maps as the slopes do not interfere with the visual analysis. The second lowering was necessary for the graphs as MAR and SAR do not give the same information outside the melt season. This effect is still visible in the evolution of the percent of melt detected by SAR through the constant plateau in winter. With the same explanation, the three places with blue-ice and lakes were also excluded from the temporal analysis. The problems generated by a σ_0 lower than the SAR threshold during all the year could have been corrected by the normalisation proposed by Liang et al.(2021) but it would have taken too much time. Another solution applied to override the more complex boundaries between the physical elements was to restrain the analysis to a smaller region inside the shelf.

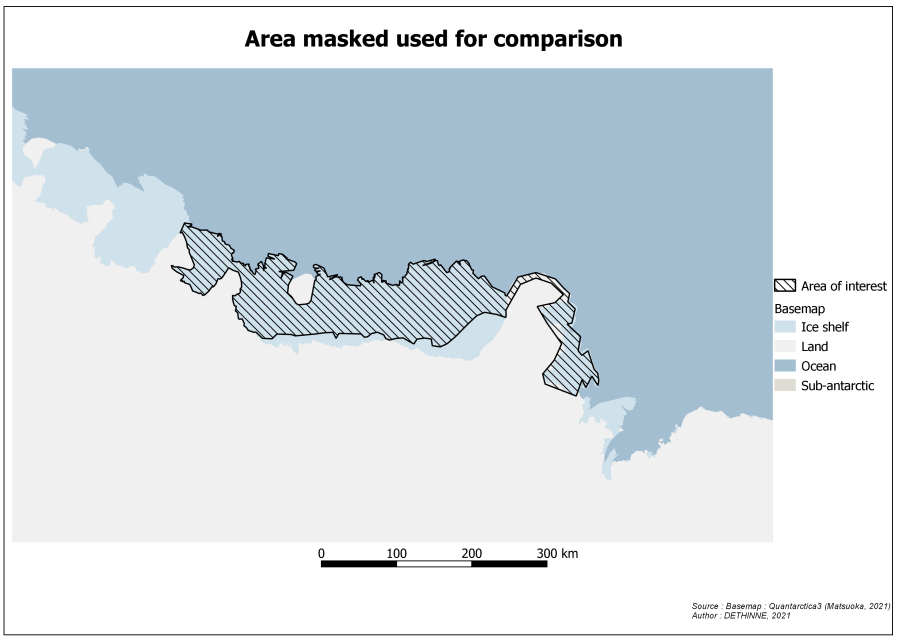

Figure 6.2: Masked area. This area is used to create the time series. The differences with the area in figure 6.1 are that the area is limited to the ice shelves and the three parts containing lakes are removed.

To answer the questions of when, where and how many differences, the MAR variables are directly compared to SAR. However, the analysis is focused on the ME variable as well as the melt index built with WA1 and RO1 (referenced by "WR" hereafter) as they are the products characterising melt. Still, all the tools for comparison are presented in annexes 8.3.

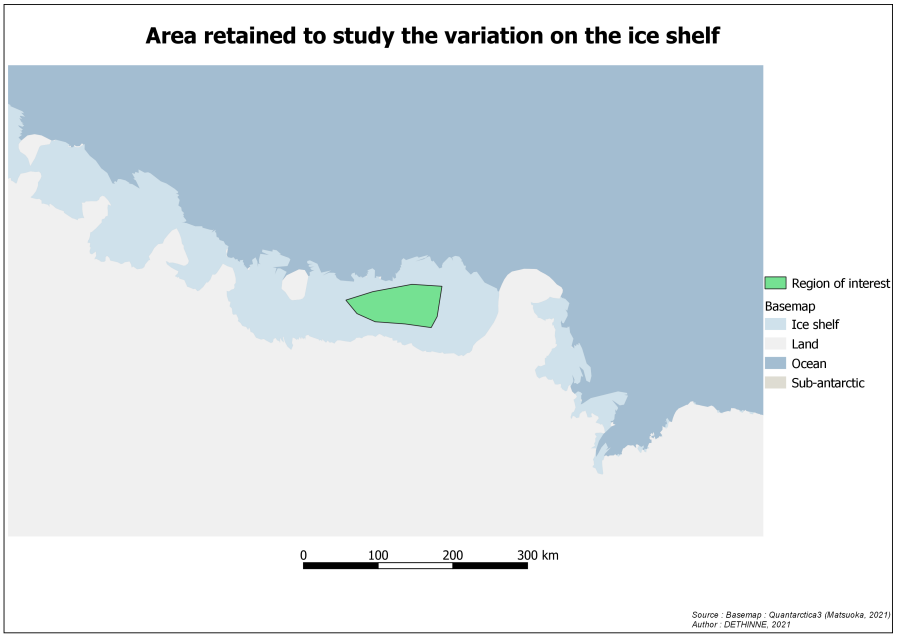

Figure 6.3: Zone used to study variation over the ice shelf. The region is used to try mitigating side effects at the boundaries of the physical elements as slopes or coastline. It has been chosen randomly inside the ice shelf.

6.1 Temporal

Temporal variations are studied with the two time series graphs created (fig 5.2 and 5.3). By plotting the percent of the image covered by melt, it is also possible to try quantifying the differences between SAR and MAR. Analysing the graphs is not very accurate if done alone. To complement the analysis, external data as the comparisons maps and the base images are used too. Some generalisations are made in the text. The melt season starting at the end of year X and finishing at the beginning of year X+1 is called year X+1 for example. The SAR data, as well as σ_0, are also referenced by "SAR" when there cannot have confusion.

SMB

The first variable to be analysed is the surface mass balance. The choice to keep

SMB as a part of the analysis was based on the hypothesis that when melt occurs, the mass balance is negative and positive else. However, the reality is more complex. There is a lot of other components influencing SMB and a simultaneous variation is not visible in figure 6.4. Nonetheless, when strong episodes of melt

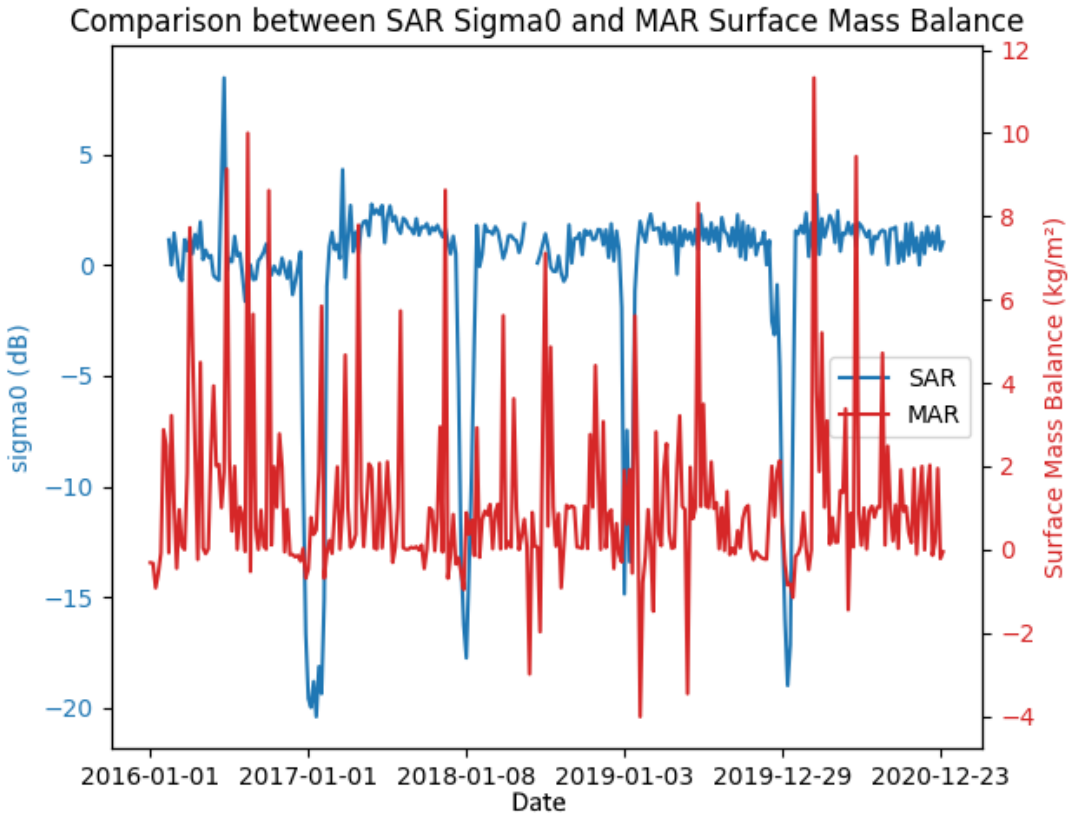

Figure 6.4: Evolution of σ_0 and SMB. SAR σ_0 values are represented in blue and MAR SMB in red. There is no clear correlation between the two variables in this graph made in the restricted zone on the ice shelf. Lower σ_0 does not correspond with lower SMB and higher SMB does not correspond with higher σ_0. The only observation to be made is that when there is a lower σ_0, SMB tends to be small.

happen in SAR, SMB is quite low. It is also to note that negative values do not correspond with the surface melt detected by SAR. Two main possibilities can explain the difference between SAR σ_0 and MAR SMB. First, SMB image could have wrong values. The NetCDF file containing the SMB values was divided into two bounds informed as depth. The first layer, supposed to be the first meter of depth, is the one used. As there was neither confirmation nor denial of this information being the one to be the most relevant, it is the one presented. The second possibility, more realistic, is simply that surface melt does not have a strong impact on SMB. As explained previously, SMB is calculated as the sum of all the processes that cause accumulation or ablation. These events could have no influence on σ_0

but a strong one on SMB. For example, strong katabatic winds occurring at the bottom of the slope leading inland have an impact as an ablation process but are not visible throughout the radar backscattering coefficient. Same for the accumulation process, snowflakes are smaller than the 5cm C band wavelength and thus do not cause backscatter.

ME

ME variable is the closest variable of what is detected during melt binary classification of SAR images. The link between the two variables is visible in figure 6.5. For the four complete melt seasons that can be seen on the graph, the increase in ME corresponds with a decline of σ_0. This observation makes perfect sense as explained multiple time before, the presence of liquid water in the snowpack results in a diminution of the backscatter coefficient recorder by SAR's sensor. Two other observations can be made regarding the graph (fig 6.5). First, The quantity of melt does not seem to be correlated with the σ_0 value. No matter the quantity of melt modelled, σ_0 reaches almost the same value of -15/-20 dB. This observation

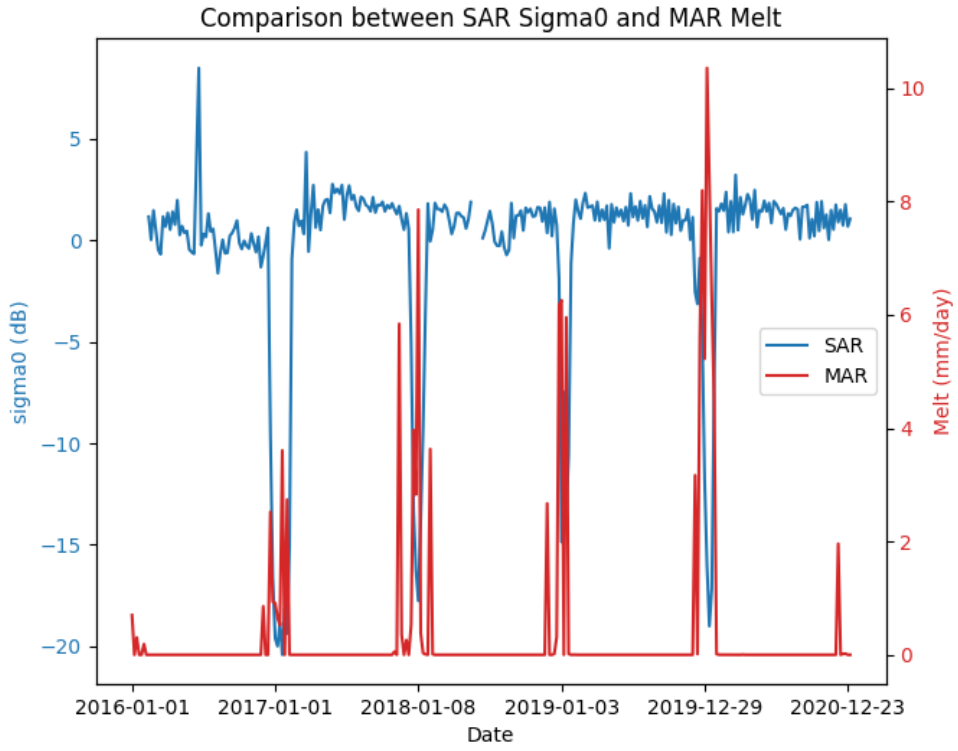

Figure 6.5: Evolution of MAR ME and SAR σ_0. The variation of the two variables seems correlated, low σ_0 corresponds to high ME as expected. A gap of a few weeks can be seen between the rise of ME and the decline of σ_0. The time gap can be explained by the freeze/thaw cycle that is not perceived by SAR. SAR σ_0 reaches -15/-20 dB no matter the quantity of melt modelled.

may confirm that the threshold choice for SAR does not have an impact that will change the conclusion of this work. The drastic change in σ_0 can be either because the change in scattering is more binary than continuous or because the images were taken when there is already a lot of liquid water in the snowpack. The last explanation corresponds with the second observation. There is a recurring pattern that appears on the graph: MAR models melt 6 to 12 days before the decrease in σ_0. Once again, there are two hypotheses for this pattern, one regarding SAR and one regarding MAR. Either a certain quantity of water is needed for volume scattering to turn into specular reflection or MAR tends to model melt too soon. The first assumption is the privileged one. When snow and ice melt, some water can percolate deeper in the snowpack and/or refreeze before the satellite passes.

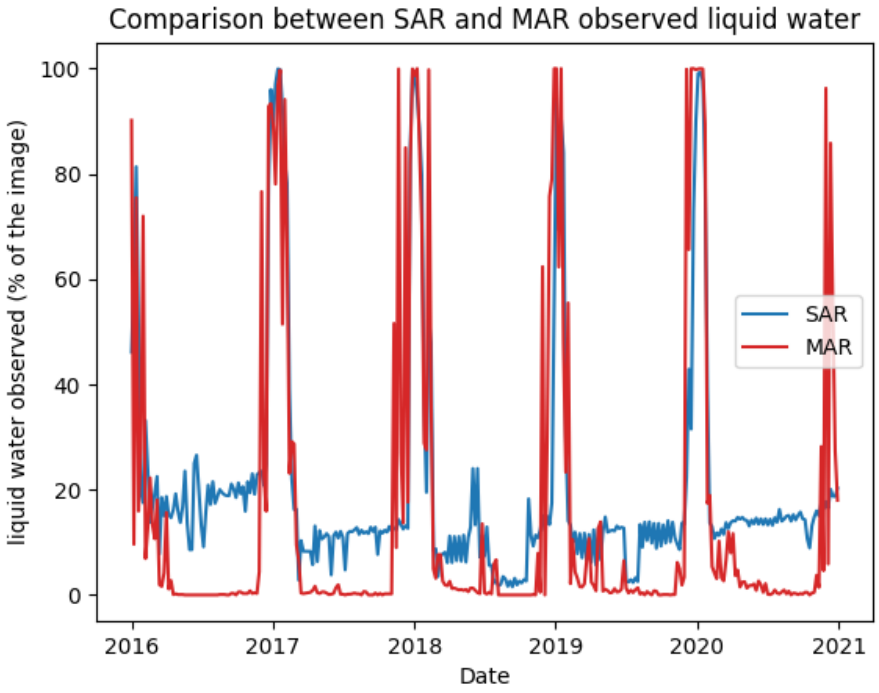

Figure 6.6: Evolution of quantity of meltwater detected by SAR and MAR ME in the whole studied zone. As for the temporal analysis, MAR has higher values before SAR but once SAR starts detecting melt, the two are about the same value. In general, the constant melt detection out of summer in SAR comes from the Prince Harald ice shelf.

The quantitative analysis is more or less the same as the temporal one. Melt modelled by MAR is occurring a week or two before SAR detects melt, the quantity of melt is greater for MAR before the two get similar (fig 6.6). More visible than in figure 6.5, especially in the graph representing the evolution in the smaller zone (fig 6.8), the end of melt season of 2016 and the start of the 2021's one are dissimilar in SAR and ME. If the explanation of 2021 is certainly the same as why MAR

models melt before SAR detects. For 2016 the explanation is still to be found in the availability of data: the mosaics are not full in 2016. It is the reason why the difference is less clear for the image, with the zone, a few pixels with different values give a large difference of melt coverage. Figure 6.6 also shows a problem described in the melt binary classification for SAR, a constant detection of melt, even during winter. When looking at the comparison map, it is clear that the majority of constant melting in SAR is coming from the Prince Harald ice shelf (see fig 6.7). The reason for the lower σ_0 there is not determined but the change does not come from the mosaicking as it is already present in the non-merged images. A comparison with HV polarisation has also been conducted (fig 6.9). The

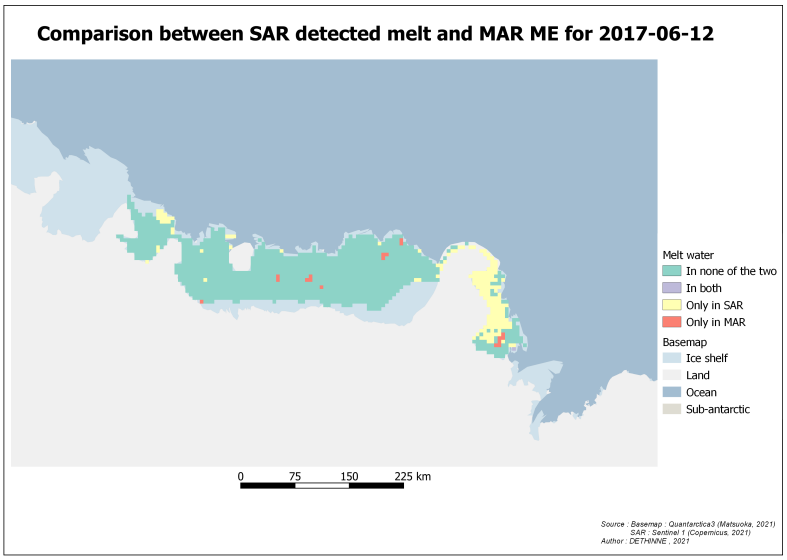

Figure 6.7: Comparison map for 2017-06-12. The East part of the map, Prince Harald ice shelf, appears in yellow, meaning that SAR detects melt but MAR does not model it.

threshold used for SAR is -5dB in that case. The value is randomly chosen as the double of the HH threshold but rounded. The comparison is the same as for HH except that there is more variability in the surface covered in winter for SAR. The variability is explained by the poor choice of threshold as the lack of HV images.

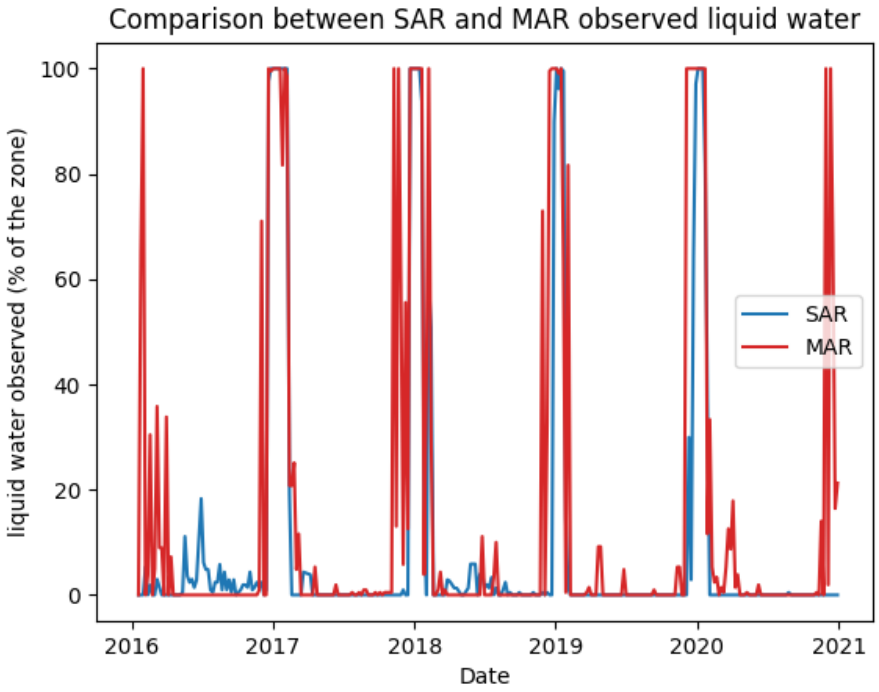

Figure 6.8: Evolution of quantity of meltwater detected by SAR and MAR ME in the limited area. As for the temporal analysis, MAR has higher values before SAR but once SAR starts detecting melt, the two are about the same value. For 2016 and 2021, SAR detects no melt in opposition to MAR.

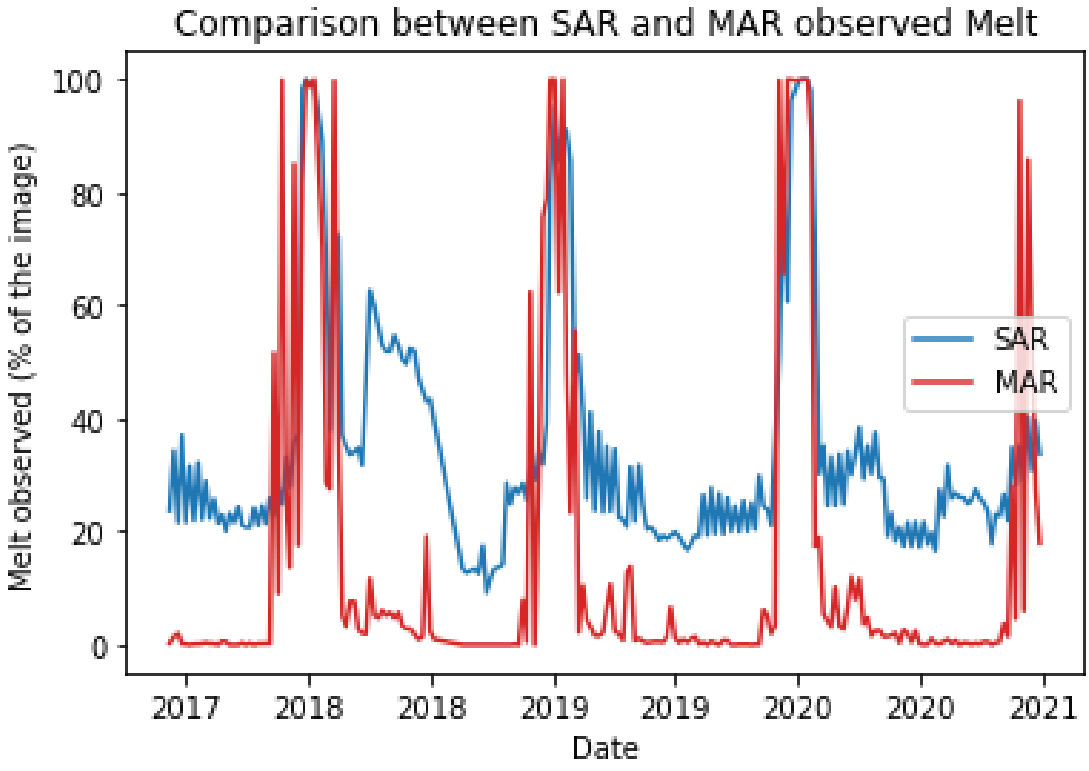

Figure 6.9: Evolution of quantity of meltwater detected by SAR and MAR ME in the whole studied zone with HV polarisation. The analysis is the same as for HH polarisation.

WR

WR is the other variable that is supposed to represent melt with MAR data, based on the equation 5.1. The difference between WR and ME is that the variable ME is the quantity of melt that is produced during the day when WR is built with WA1, representing the quantity of water in the snowpack. Then the quantity of water given by WA1 is water that did not refreeze whereas for ME it can be the case. The variable is built during the creation of the graph or the maps. No files are containing the values of WR upon the ice shelf, only binary classification of melt/no melt as comparison raster is created. It was thus not possible to create a graph representing the evolution in value, only the surface of the modelled melt.

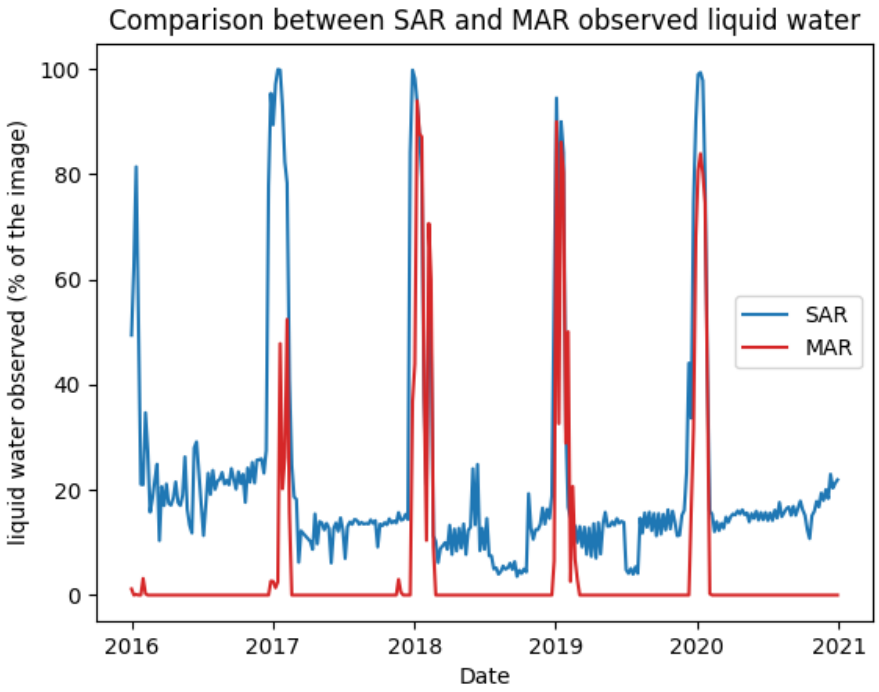

Figure 6.10: Evolution of quantity of meltwater detected by SAR and by WR index in the whole studied zone. The comparison is a little bit opposed to the comparison with ME as WR tends to model less melt and later than SAR detects it. In 2016 and 2017, the difference is blatant. In general, the constant melt detection out of summer in SAR comes from the Prince Harald ice shelf.

The observations made with ME are not valid with WR. Some can argue that is even the opposite. SAR observes melt before WR is considered as such (fig 6.10). The explanation may come from the inability of SAR to get through liquid water. If there is water in the top layers, σ_0 will be reduced as specular reflection can occur. As an average value of the first metre of snow and ice is used to

calculate WA1 and RO1, this does not mean that WR will have a sufficient value to be above the threshold. The difference with ME can, therefore, explains the difference in behaviour observed here too. Interestingly, the peaks observed for ME in early 2016 and 2021 are not present in WR. While it corresponds with SAR observations for 2021, a smaller melting episode was still observed by SAR in 2016. When looking at the evolution in the smaller zone (fig 6.11), the same observations can be made. Again, the SAR's variation in 2016 and 2018 are likely caused by the detection of melt on the Prince Harald ice shelf or erratic pixels. Yet, in 2018, ME have small values when SAR observes a small amount of melt but not WR. For the quantitative analysis, in the global area, the surface of the melt is slightly

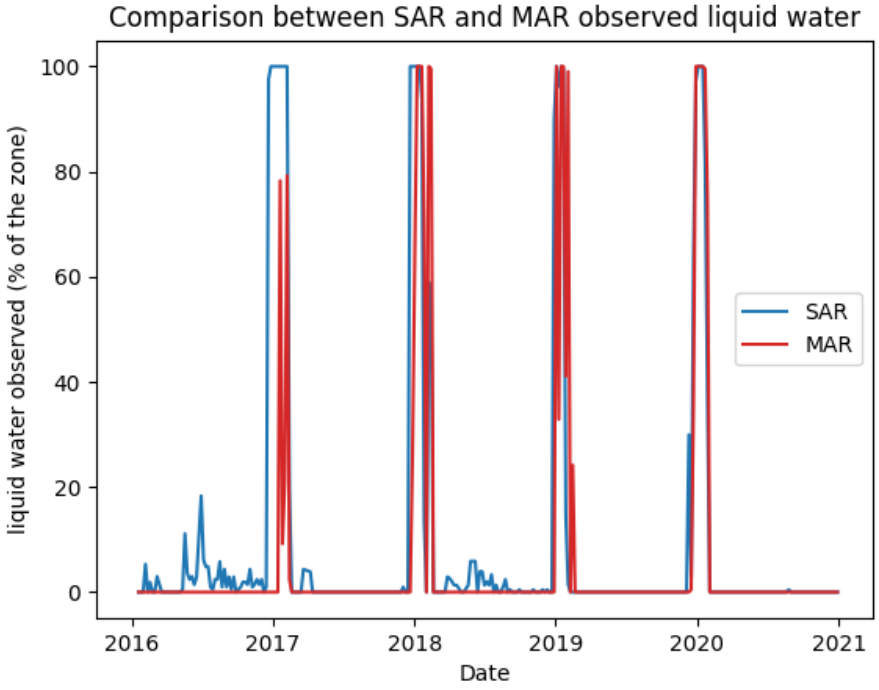

Figure 6.11: Evolution of quantity of meltwater detected by SAR and by WR index in the limited area. There are fewer differences between SAR and WR in the limited zone than in the image. The timing and quantity are similar for 2019 and 2020, a bit shifted for 2018 and 2017. The melting detected by WR is still lower than for SAR.

lower for WR in 2018, 2019 and 2020 (5 to 10%) but in 2016 and 2017, there are much bigger differences. The melt in 2016 is not modelled with WR and only half of it in 2017. The differences can come from the choice of the 0,1 value as a threshold, perhaps SAR detects meltwater before.

By looking at the second graph (fig 6.11), the differences are smaller, in time and quantity. The same percentage of melt is observed for 2018, 2019 and 2020, nothing for 2016 and 2021 and fewer for 2017. In 2019 and 2020, the start and the end

of the melt are the same for the two variables. Nonetheless, in 2017, weeks pass before SAR and WR both have melt. The last graph represents the comparison with HV again (fig 6.12). The observations are the same as for HH polarisation: less melt surface and a bit later in time.

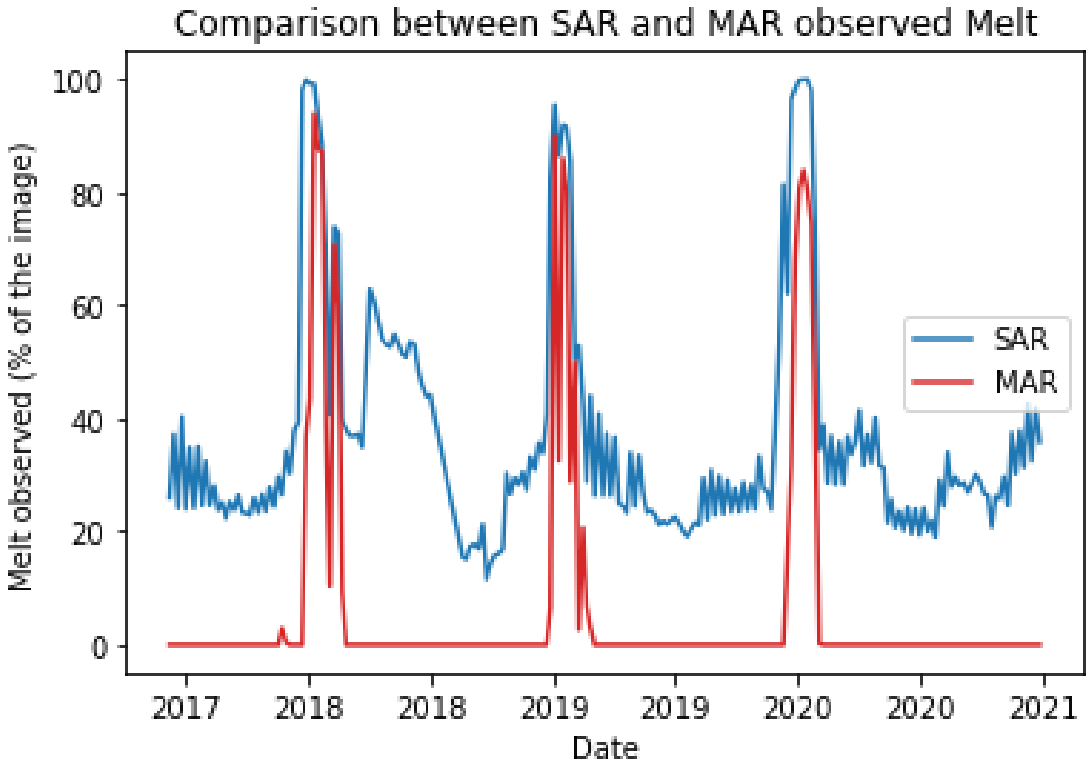

Figure 6.12: Evolution of quantity of meltwater detected by SAR and by WR index in the whole studied zone with HV polarisation. The analysis is the same as for HH polarisation.

WA1

In a manner of readability, page layout and for keeping the analysis focused on the two previous variables, the graphs for the three next ones are move to annexe 8.3.2.

As for WR and ME, WA1 is strongly correlated with σ_0. The same pattern as for ME can be observed: SAR σ_0 detects melt after WA1. The time difference is only visible when looking at the surface covered by melt. Quantity and time extension of the presence of liquid water on the snowpack is relatively high because the threshold is set to 0 for this variable. It results in a modelisation of water that begins before the detection of melt by SAR and finishes after for each melt season. The explanation can be the same as for ME, either MAR models too soon or the SAR needs enough water in the top layer to stop volume backscatter. The

observations made on the whole zone are also applicable to the restricted zone. The comparison with WA1 is marred by two problems. The first is the empirical threshold of 0. As soon as a pixel have a value, even the smallest possible, the pixel is considered as melt. The quantity of melt is thus artificially emphasised in comparison to the other MAR variables. The second is the definition of WA1 itself. The variable gives the quantity of water present in the snowpack. However, even if the basic file gives it as per depth layer, the value is averaged and this information is lost. If the water is only present in-depth, the layers above it still participate in volume scattering and therefore, a higher σ_0 than if the water would have been in the top layers.

RU

The quantitative and temporal comparison of RU with SAR σ_0 is less reliable and significant with the two graphs used here. Indeed, for some years, most of the surface runoff occurs in the zones that have been masked before the creation of the time series (fig 6.13). If the graphs do not provide much information, the location

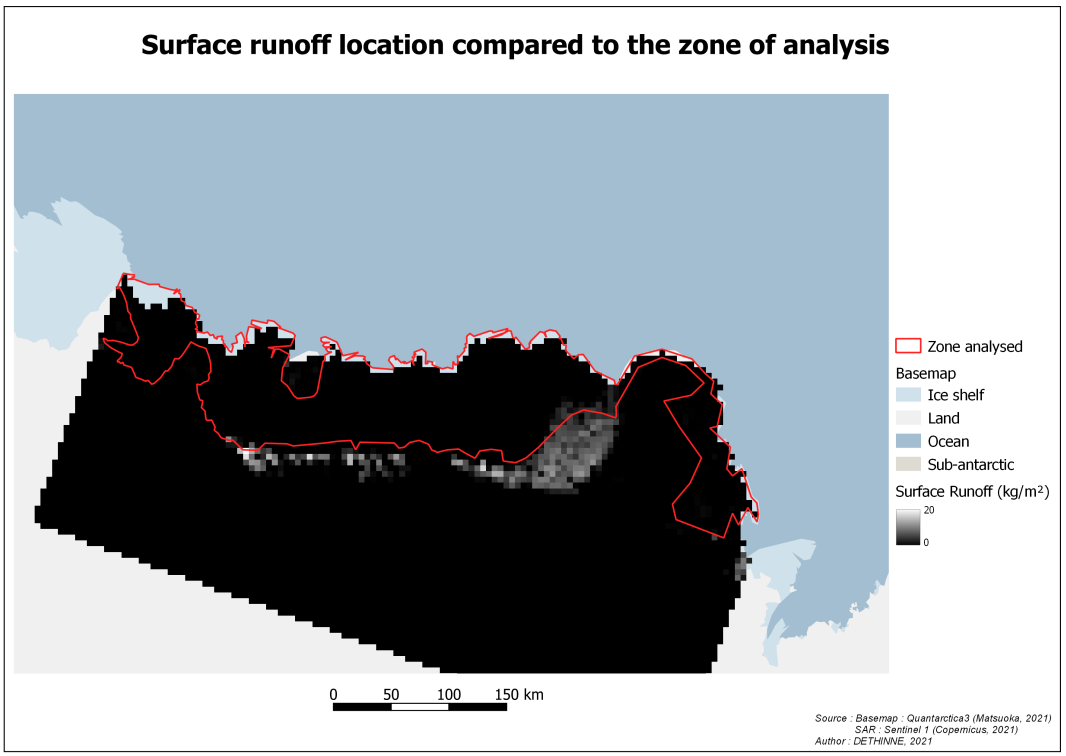

Figure 6.13: Location of RU in relation to the area of interest. Most of the values are outside the area studied with the graphs.

should lead to interesting spatial analysis for this variable. It also supports the fact that some phenomena happen in the masked zone and that they could have

been seen with SAR, with a satisfactory normalisation. Nonetheless, as for the precedent variables, either for the global area or the smaller zone, RU seems to follow the same variation as σ_0 but at a smaller scale. The small event recorded by SAR during the 2018 winter is even represented in RU data.

SU

Once again, low values of σ_0 correspond to high values of the MAR variable. The growth in sublimation is more continuous than the decrease of σ_0 but the peaks correspond with each other. As for WA1, SU covers the images faster than melting detected with σ_0, for a longer time and a shorter intensity. There is some variation in SU. The variation makes that sometimes during winter, the values are over the threshold. It results in some images covered totally by values of SU over that threshold at all time of the year. Outside of the peaks, the relation is less clear.

6.2 Spatial

As explained before, the spatial analysis is made with another open-source software: *GeoDa*. To have a better view of the situation, the zone used is the entire zone under 400m of altitude. The comparison with SMB is not conducted for two reasons: first, temporal analysis was not conclusive and second, without a threshold to use, it is not possible to calculate the probabilities described previously.
The data and maps presented shortly after may contain bias. To construct correlation and the two probabilities, every image is taken into account. Days, where no event is detected, are also taken in the count, resulting in a higher value than if only the melt season was taken into account for the correlation and the first probability. The second calculus of probability tries to prevent this bias by only taking into account the days where SAR detects melt by using a conditional probability and assuming a dependence between the two variables. The resulting probability can be interpreted as "what is the likelihood of MAR modelling melt when SAR detects it".

ME

First, it is the correlation of ME with σ_0 that is analysed. The expected result is a negative coefficient as σ_0 decreases when melt increases. The observations made with the comparison maps are flagrant on the correlation map (fig 6.14). The centre of the ice shelf and the coastline present a relatively high and negative correlation (between -0,6 and -0,7) whereas slopes and blue ice zones are close to 0. With a

p-value of 0,0001, the Moran's I of 0,786, statistically significant, confirms a strong spatial autocorrelation in the correlation between the two variables. Interestingly, the spatial autocorrelation conducted with LISA (fig 6.15) shows highly significant low-low values on the ice shelf but also highly significant high-high values near the slopes and in altitude at the far south of the zone.

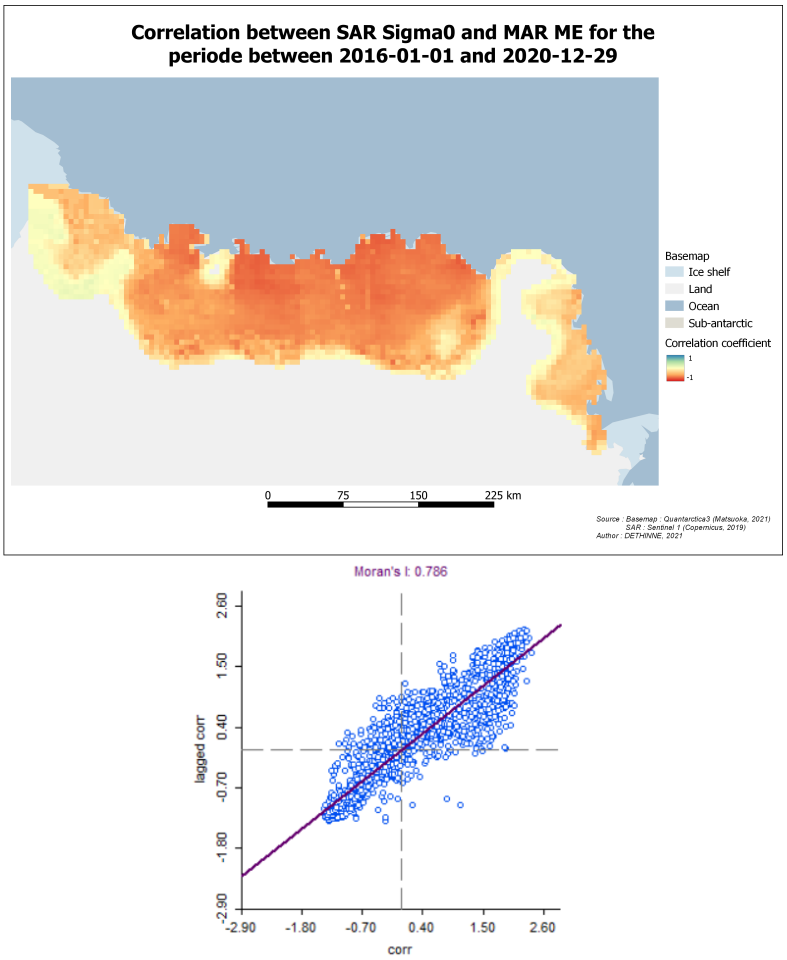

Figure 6.14: Correlation map between SAR σ_0 and ME. The major part of the ice shelf have higher correlation values (-0,6 to -0,7) than areas with slopes (near 0). The spatial autocorrelation is confirmed by a Moran's I of 0,786.

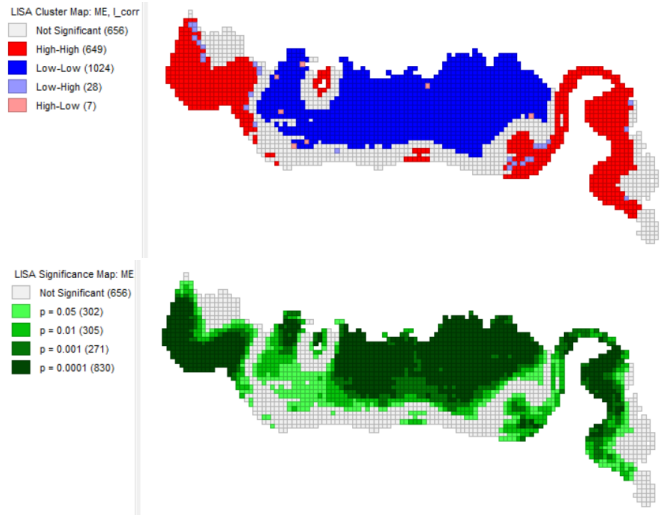

Figure 6.15: Local Moran's I map (top) and its statistical significance (bottom) for the correlation map between SAR σ_0 and ME. Areas pinpointed in the precedent maps turn out to be the zones that have the most significant spatial autocorrelation.

The probability of having the same information makes the non-concordance between σ_0 and ME in some zones even more apparent (fig 6.16). On RBIS, there is a high probability for the two data to deliver the same information (90%) but on slopes, Prince Harald ice shelf and at the three masked zones, the probability gets lower (around 20-30%). However, Moran's I, even if still statistically significant, is lower with 0,697. Local Moran's I also shows that the zones described have statistically significant local spatial autocorrelation (fig 6.17). These two short analyses have permitted us to conclude that concerning ME and σ_0, they are mostly similar and linked on the majority of the ice shelf but there are some zones where it is not the case.

The last spatial analysis concerning ME is about the probability of having MAR modelling melt when knowing SAR observes it (fig 6.18). The observations to be made with this probability are relatively the same as the precedent. However, the probability is not as smooth. Values behind the ice rise are 10% lower than at the eastern part of the shelf. Again the variables is spatially autocorrelated (I = 0,775). Despite the differences in the values, LISA (fig 6.19) also displays the same significant zone of high-high on the ice-shelf and low-low for the zones that are less likely to have the same values.

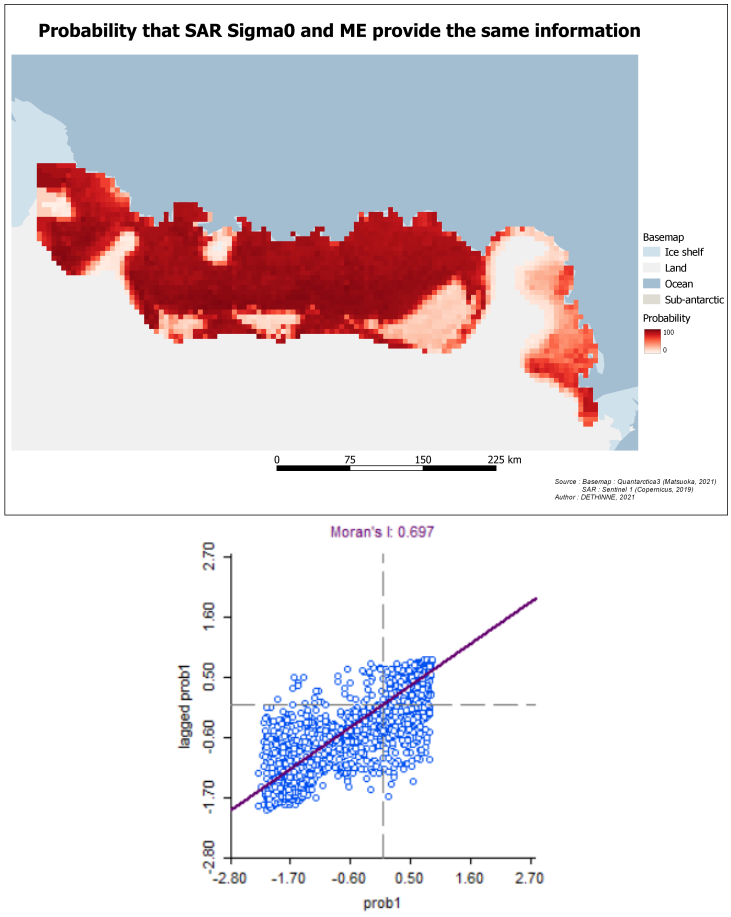

Figure 6.16: Probability map of SAR σ_0 and ME corresponding together. The major part of the ice shelf shows higher probabilities (about 90%) than area with slopes and blue ice (about 20%). The spatial autocorrelation is confirmed by a Moran's I of 0,697.

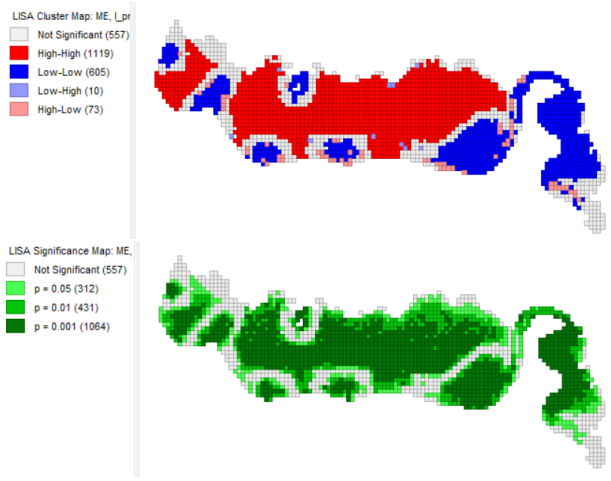

Figure 6.17: Local Moran's I map (top) and its statistical significance (bottom) for the probability map of SAR σ_0 and ME corresponding together. Areas pinpointed in the precedent maps turn out to be the zones that have the most significant spatial autocorrelation. The zones are better separated by this variable.

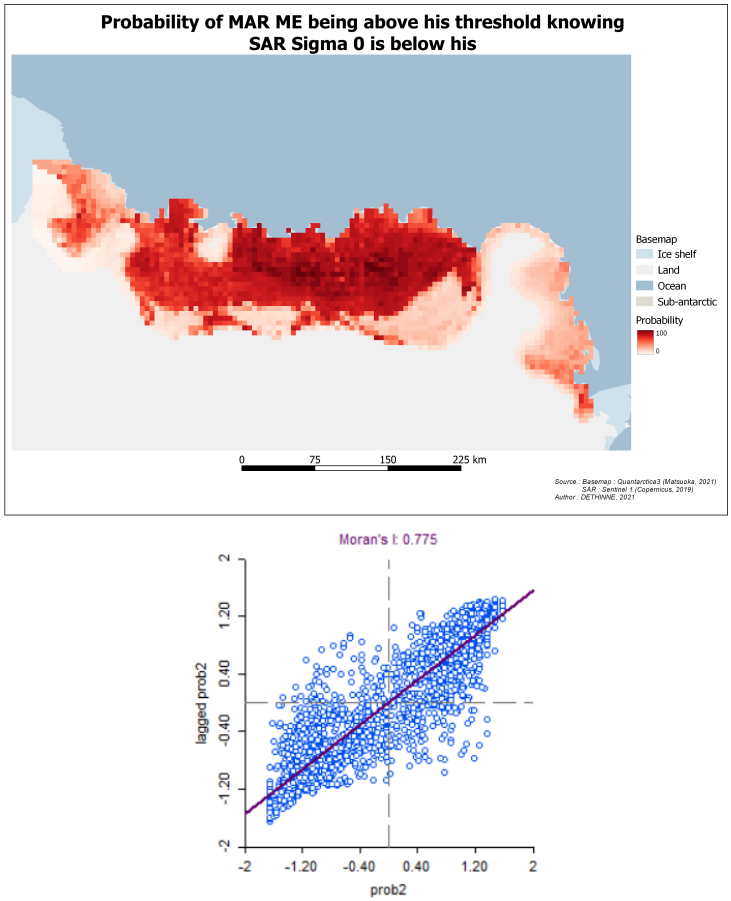

Figure 6.18: Probability map of ME modelling melt knowing SAR detects it. The spatial autocorrelation is confirmed by a Moran's I of 0,766. The ice shelves East and West of the zone show smaller probabilities than RBIS.

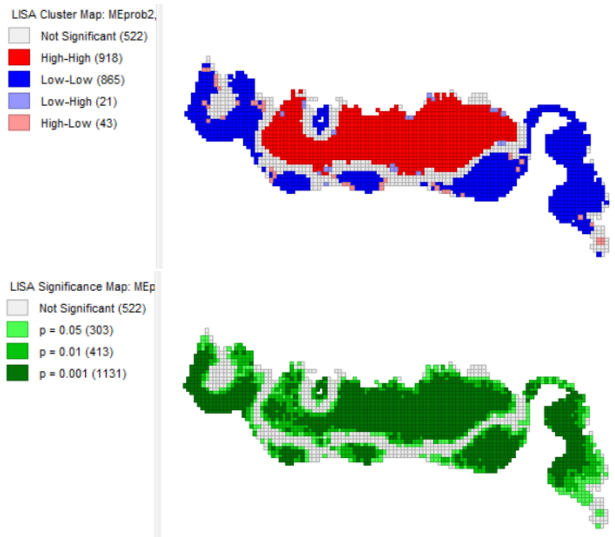

Figure 6.19: Local Moran's I map (top) and its statistical significance (bottom) for the probability map of ME modelling melt knowing SAR detects it. The maps are really close to the previous LISA (fig 6.17) maps except for the West part.

WR

As for the temporal analysis, the remaining figures are moved to the annexes (annexe 8.3.3) in a manner of exhaustiveness and to avoid cluttering the analysis. For the correlation map, the analysis is the same as for ME, which is logical as they represent almost the same phenomenon. The almost same values are visible on the ice shelf, with at 0,8 on the coast, descending to 0,2 in the blue ice zones and almost 0 on the slopes. Local Moran also gives the same reasoning as for ME. On the first probability map, the zones are even more distinct with 95% on the ice and 5% elsewhere. The distinction between the zones is due to WR showing less melt than the other variables. When ME and WA1 tend to model more water than SAR detects it, WR is more in line with SAR on the ice shelf but less in the problematic zones.

The conditional probability is one of the variables with the greater Moran's I with I = 0,862. The results are consistent with the previous analysis: it is less likely to have WR modelling melt when SAR detects it. The values are lower than for the other variables with 60% near the coast and 40% behind the ice rise. In fact, the spatial distribution is visible on the map. With WR, the edges of the area are not likely at all to have melt at the same time as SAR. It can be assumed that it is because of the lower quantity of melt detected by WR (see the temporal analysis).

WA1

WA1 is even closer to ME than WR. The correlation values are a bit higher than for ME, ranging from 0,8 to 0,7 on the ice shelf and 0,4 in blue ice and Prince Harald ice shelf. The Moran's I is also higher than for ME (0,81). In terms of the two likelihoods, they both show the same pattern as ME with a gradient from West to East. With WA1, the probabilities of it giving the same information as SAR is a bit higher in the 3 pockets before the slope (approximately 5 to 10% more). But lower in the rest of the area (90% >< 92%). The explanation comes from the fact that when the melting season come to an end, the melt is thus not modelled but there is still water in the snowpack for one or two weeks after. This presence of water after the season is not detected by SAR so it may be located deeper in the snowpack or there may be only a small amount of water left. For the second probability, Prince Harald ice shelf as well as the higher ground and the three pinpointed zones have a lower probability of 20% on average compared to the rest of the zone.

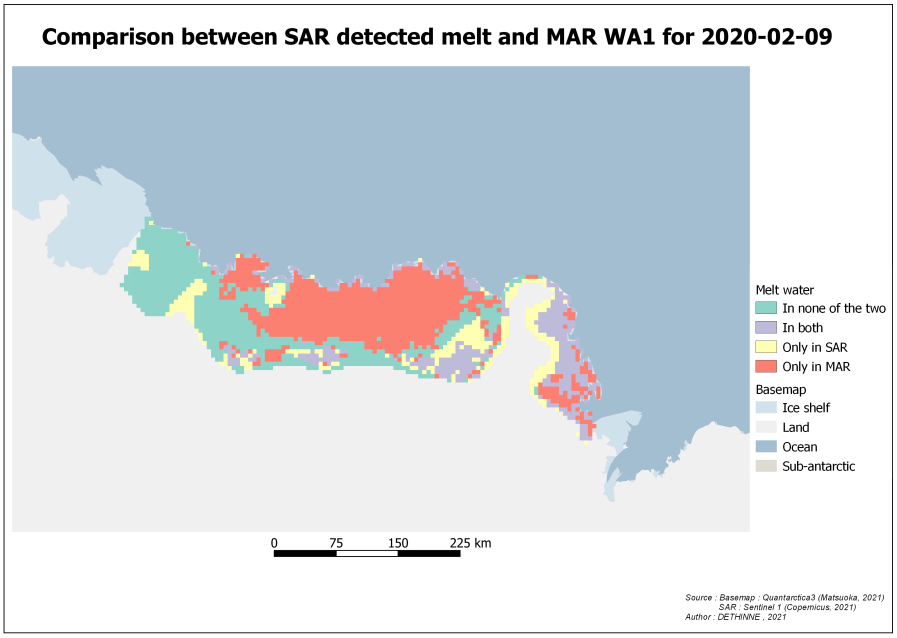

Figure 6.20: Comparison map for 2020-02-09 with WA1. There is still a lot water in the snow pack in numerous place of the ice shelf.

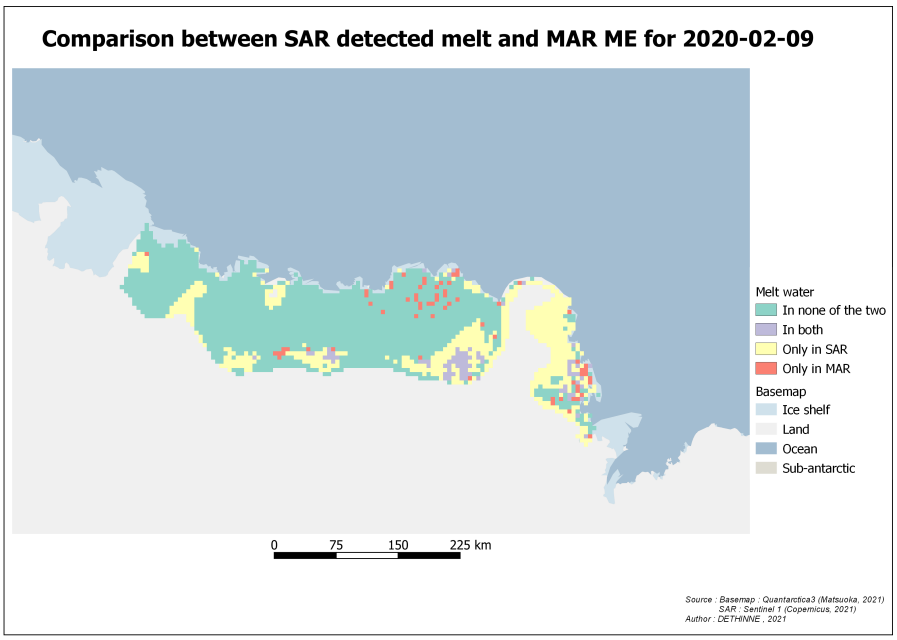

Figure 6.21: Comparison map for 2020-02-09 with ME. There is not a lot of melting that has been modeled as opposed to WA1.

The second probability map is mostly the same as for ME but with 1 or 2% of likeliness in more for WA1. To sums up, ME and WA1 are as similar for quantitative and temporal comparison with SAR as for spatial analysis. They both show strong spatial autocorrelation and a higher negative correlation in the ice shelf than on the slopes and lakes.

RU

RU variable was taken in the analysis because, in a first approach, it looks like the location of RU during specific years could explain some differences between SAR and ME (see fig 6.13). However, the spatial analysis is less convincing on this part (I = 0,5). The correlation map still goes in the direction that was expected with a greater correlation on the blue ice than in the other zones but the values are smaller than for the variables modelling melt. Surprisingly, there is a line of uncorrelated values between the zones at the bottom of the slope and the ice shelf. The two probability maps should be viewed in parallel as the non-melting period strongly influences the probability of having the same values. That first probability (fig 8.27) map has almost the same characteristics as the other maps of that type because of that fact. Whereas the conditional probability map is more similar to the correlation map. Even if statistically significant (p-values<0.05), Moran's I value is only 0,45 meaning little positive spatial autocorrelation. LISA's maps also represent this low spatial evolution with spare batches of significant values. Only Prince Harald ice shelf is showing strong spatial autocorrelation.

SU

Sublimation is the last variable to be compared with SAR. As noticed during time-series analysis, SU has a different behaviour than the other variables with more continuous growth. The continuous growth comparing to the more binary evolution of SAR σ_0 is noticed through the lower correlation values than for the first three variables studied. Apart from the difference in values, there is not more to say than what has already been said before.

In the likeliness of having the same information, the values show a South to North gradient with the exceptions of the 3 problematic zones that have an opposite gradient. The explanation may be that MAR tends to model more sublimation in altitude and during all the year. So where SAR detects melt during all year, it is the same for SU (resulting in high probability). Around those zones, SAR σ_0 is not low enough to be considered as melt all the year but the altitude is high enough to have sublimation. With queen contiguity and two order of neighbours, the high probabilities do not have a significant local Moran's I.

With the last map, the differences with the South-West zone are less visible with LISA.

6.3 Discussion

The obtained results are promising in term of future developments. There is a strong correlation between the majority of MAR variables tested and the SAR backscatter coefficient. Whether it is quantitatively, temporally or spatially, SAR σ_0 and ME, WA1 and WR are very similar a majority of the time. In the three variables, none is perfectly synchronous with SAR. ME and WA1 have higher values before SAR detects melt, WA1 exceeds the time σ_0 is lower than its threshold and WR is mostly under the quantity of melt detected. The thresholds chosen for SAR and MAR can have impacted the analysis but for most of the differences, there is a physical explanation. For example, MAR can model liquid water for a longer time in the snowpack without being able to see it with SAR. Water can percolate in the deeper layers of snow and volume scattering can occur above the water, causing an increase in σ_0 and the loss of the ability to see the water.
Spatial differences can be explained by zones that have a constant σ_0 under the threshold of -2.6 dB. The zones that are problematic are the ice ridge at the West of the studied zone, the Derwael ice rise, the prince Harald ice shelf and the zones of lakes and lower albedo referenced in (Lenaerts et al., 2016) (2016). The lower values may not be caused by the presence of water but could come from physical properties of the snow/ice as, in altitudes, there is less backscatter because of the snow particle size. To avoid restricting the analysis, it would have been possible to use multiple techniques: image calibration with a reference image with no melt, spatially or temporally varying thresholds, "co-orbit normalisation" (Liang et al., 2021) or all other normalisation techniques.
SAR could complement MAR by giving approximately the days when the quantity of water in the top layers is important and MAR can still models when SAR cannot see. Also, an interesting purpose of using SAR rather than optic satellite for such a comparison is that it was possible to conduct the comparison during winter and being able to monitor if events of melt happen at that time too. Results are promising and with the technique developed, conducting the experiment on a larger zone, higher resolution and with some enhancements is totally possible.

Chapter 7

Conclusion

Comparing SAR and MAR has been a challenge in several ways. First, data were not in the same format and, even after projecting the two of them in the same format and coordinate system, perfect co-registration was still needed to perform a significant comparison. Second, SAR and MAR originate from different horizons. To understand the differences and variations of each product, knowledge in a lot of fields like remote sensing, physics, glaciology was necessary.
Thanks to the Copernicus program, the observation of the Earth with space-borne sensors is made easier and more accessible. The European Space Agency offers the possibility, for whoever wants to, to get open access to the free and high-resolution data that are Sentinel-1 images.
After multiple processing and corrections, the analysis of approximately 1500 SAR images and 6 MAR variables was possible. To conduct the comparison, chosen SAR images are images with HH polarisation and in which melt is considered in a pixel when its value is lower than -2.6 dB. The MAR variables used are ME, RU, SU, SMB and WA1. In complement, an index, WR, was created from WA1 and RO1. The similarities and complementarity of the two data sources have been studied quantitatively, temporally and spatially. The co-registration of images was carried out with the creation of a grid centred on MAR data pixels and a time interpolation between SAR images. The results show a strong correlation between SAR backscattering coefficient, σ_0 and MAR variables representing melt (ME, WA1 and WR), as well as similar variations in time and quantity over RBIS.
The spatial analysis also highlights some areas where the comparison did not produce the expected results. Those areas are :

- The Prince Harald ice shelf.
- The slopes bordering the area and the Derwael ice rise.

- The lakes and the blue ice south of the studied area.

Most of the problems in the above areas can be associated with a non-normalisation of the SAR images with a reference image containing no melt. The simple threshold of -2.6 can work in zones where σ_0 is higher in non-melting times but not if the backscatter is already under it all the time.
Nevertheless, this work shows the complementarity and similarities between the two products and open the subject to more research. Some improvements can be made. For example, using a better pixel size or a larger region of interest to create larger and more precise maps of melt by using SAR and MAR together. The pre-processing of SAR and the choice of the threshold could also be more advanced to take into account more characteristics of radar imagery as the cross-polarisation. Scripts used could be optimised to reduce processing time too.
When the differences can be linked to the SAR images normalisation, the variation of σ_0 in the scene can also be due to the physical properties of the snow and ice in the site. The change in physical properties could be studied with MAR to understand the variations of SAR. The analysis stayed focused on where the analysis is satisfactory, to prove that MAR and SAR can corroborate each other rather than trying to explain the differences. The three areas mentioned above have been withdrawn from the analysis one after the other without looking for an explanation. Adding a better understanding of glaciology may improve the conclusion of this master thesis by adding further explanations for the unresolved issues.

Nomenclature

DEM Data Elevation Model

$EPSG$ European Petroleum Survey Group

ESA European Space Agency

$LISA$ Local Indicator for Spatial Association

MAR Regional Atmospheric Model

ME Melt

NN Nearest Neighbors

$RBIS$ Roi Baudouin Ice Shelf

$RO1$ Snow Density

RU Surface Runoff

SA Synthetic Aperture

SAR Syntactical Aperture Radar

$SISVAT$ Soil-Ice-Snow-Vegetation-Atmosphere-Transfer

SMB Surface Mass Balance

SU Surface Sublimation

$WA1$ Water Liquid Content

WR WA1 and RO1 Based Index

Chapter 8

Annexe

8.1 Images

The name of the SAR images used for the comparison can be found in the complementary document available on MatheO, at point 1.

8.2 Code

The codes used for the comparison can be found in the complementary document available on MaTheo, at point 2.

8.3 Comparison

8.3.1 Comparison Maps

Comparison maps can be found in an annexe document available on MaTheO.

8.3.2 Times Series

WA1

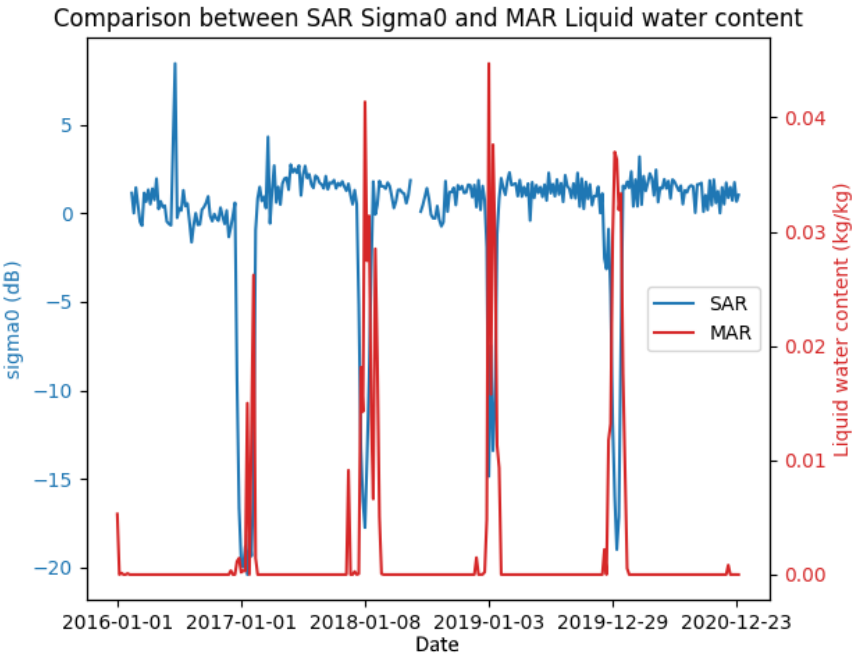

Figure 8.1: Evolution of MAR WA1 and SAR σ_0.

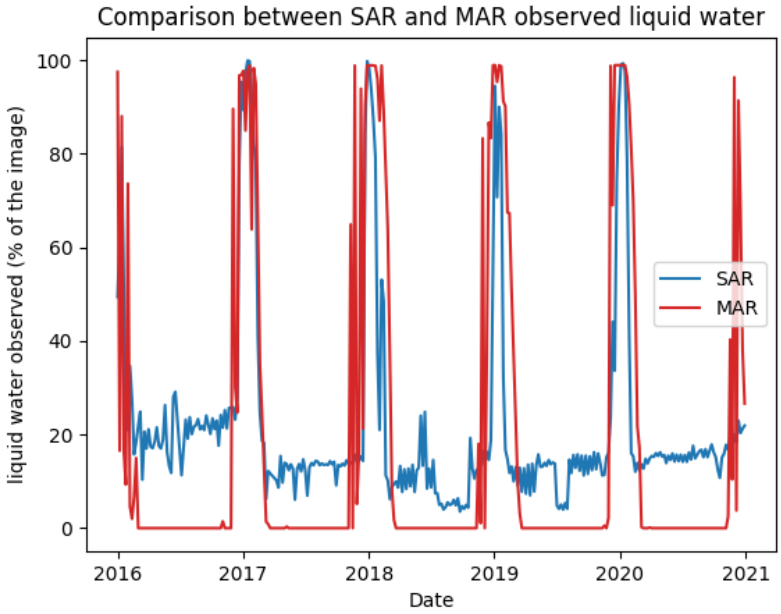

Figure 8.2: Evolution of quantity of liquid water detected by SAR and MAR WA1 in the whole studied zone.

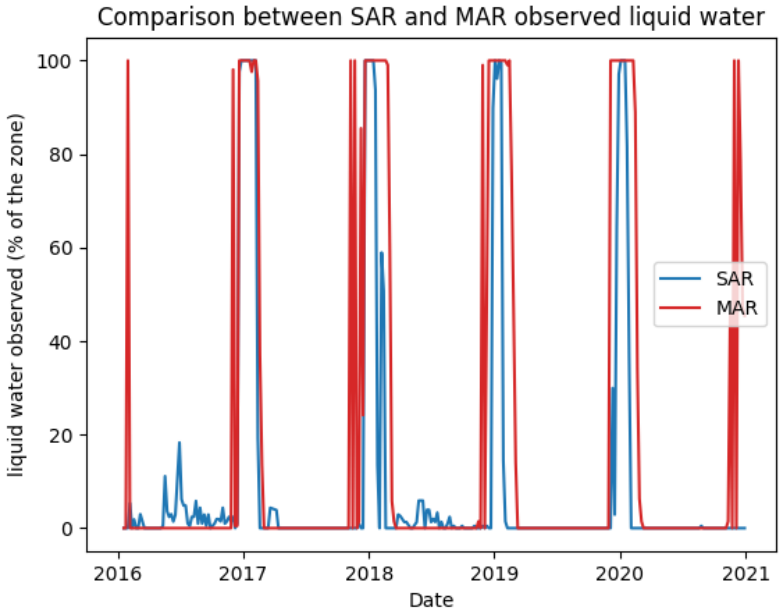

Figure 8.3: Evolution of quantity of liquid water detected by SAR and MAR WA1 in the limited area.

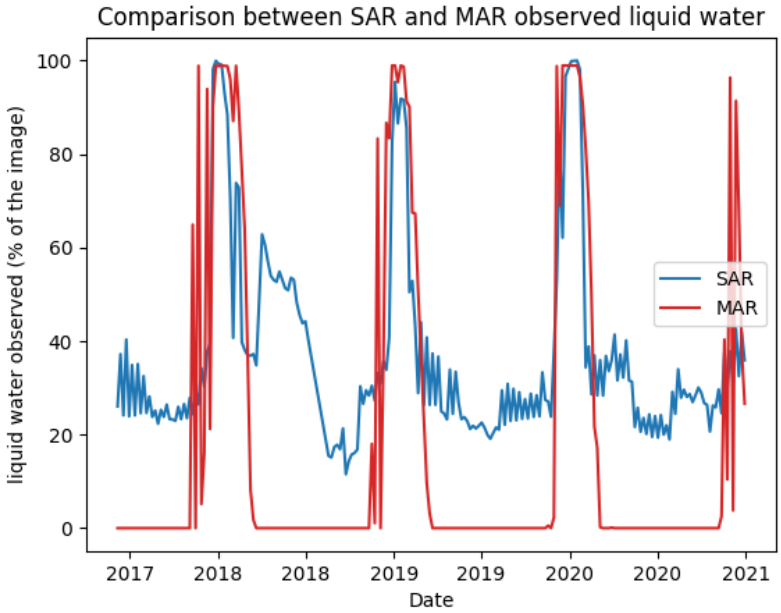

Figure 8.4: Evolution of quantity of liquid water detected by SAR and by MAR WA1 in the whole studied zone with HV polarisation.

RU

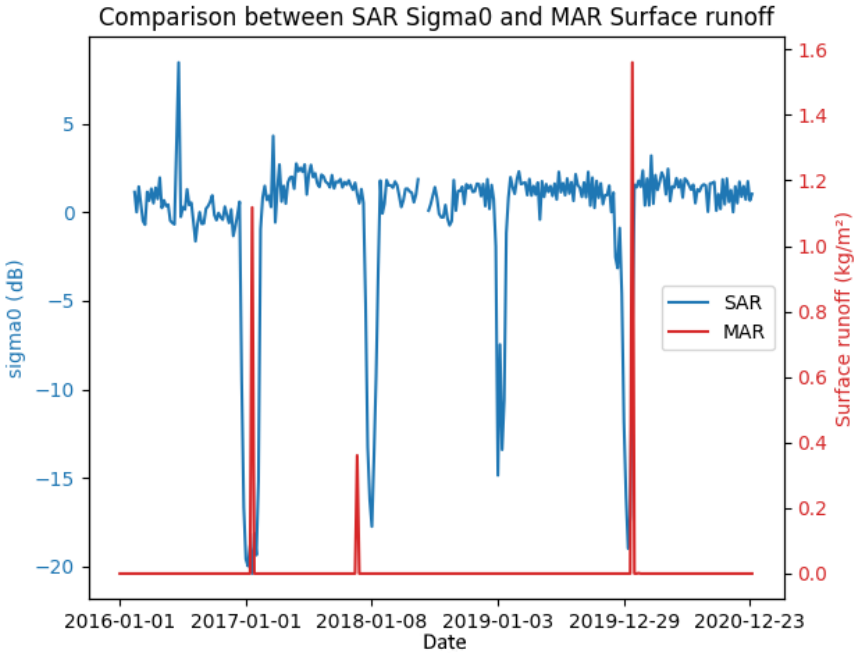

Figure 8.5: Evolution of MAR RU and SAR σ_0.

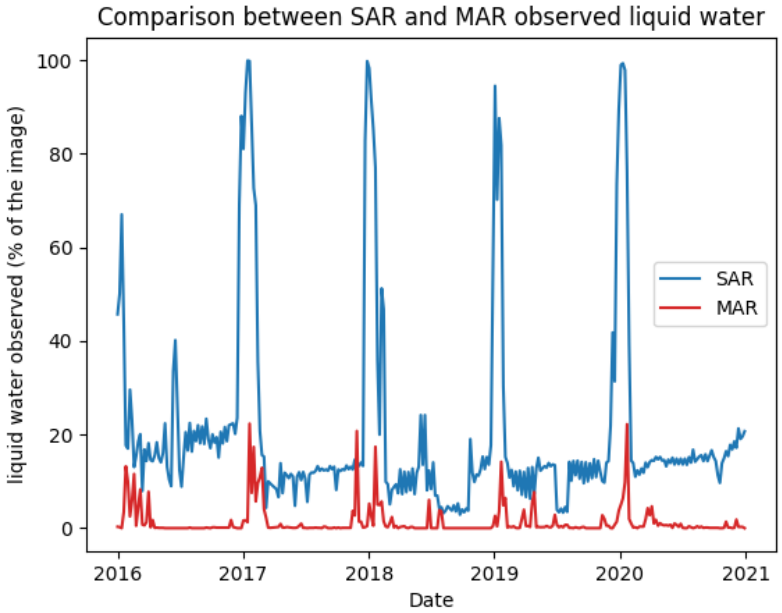

Figure 8.6: Evolution of quantity of liquid water detected by SAR and MAR RU in the whole studied zone.

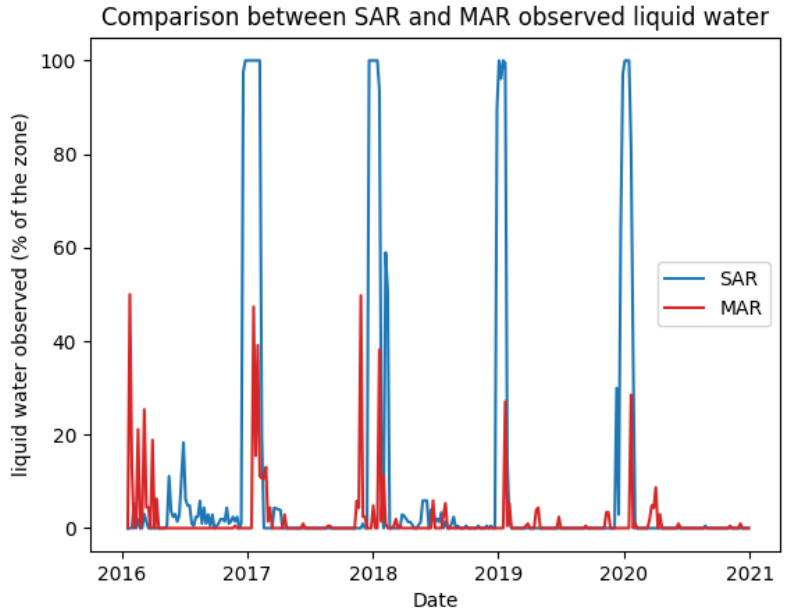

Figure 8.7: Evolution of quantity of liquid water detected by SAR and MAR RU in the limited area.

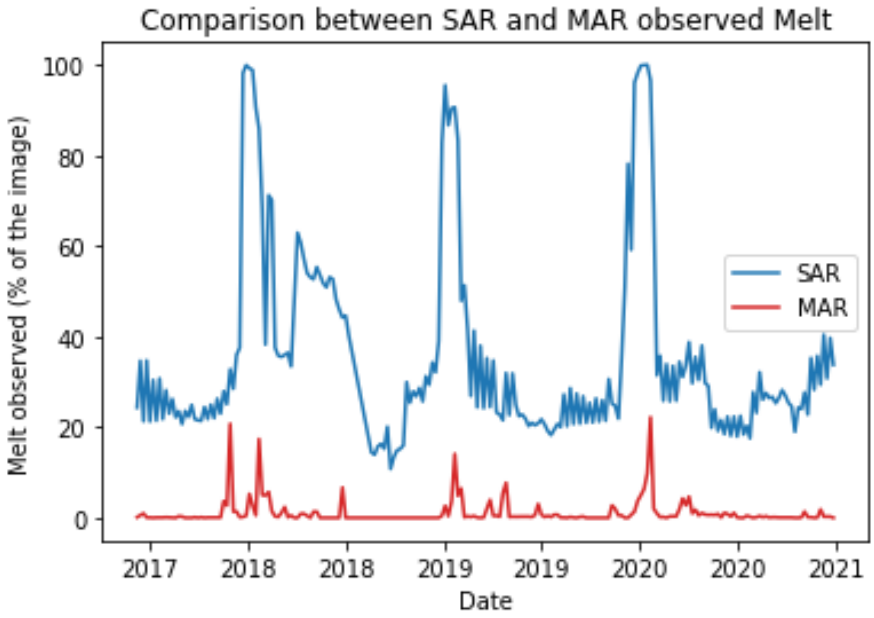

Figure 8.8: Evolution of quantity of liquid water detected by SAR and by MAR RU in the whole studied zone with HV polarisation.

SU

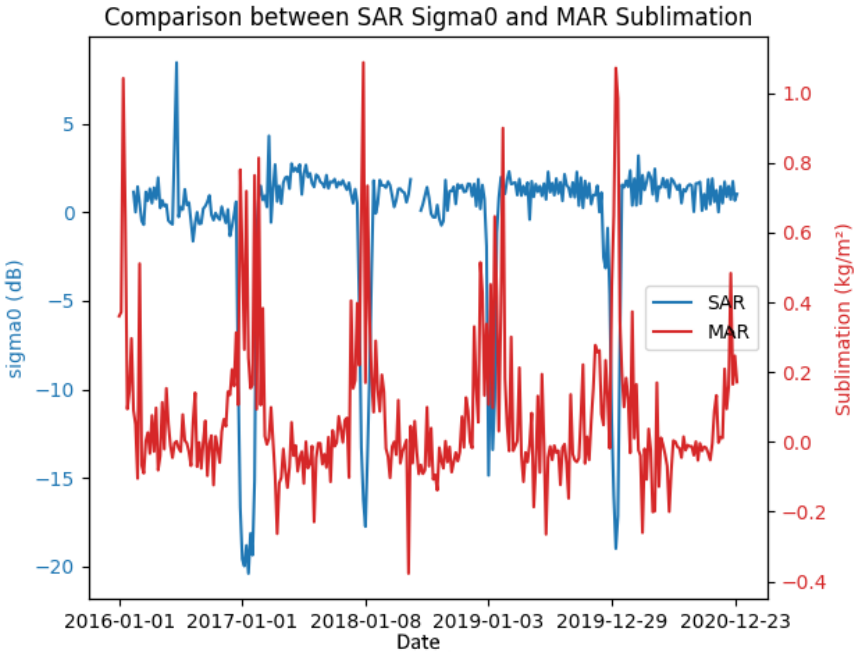

Figure 8.9: Evolution of MAR SU and SAR σ_0.

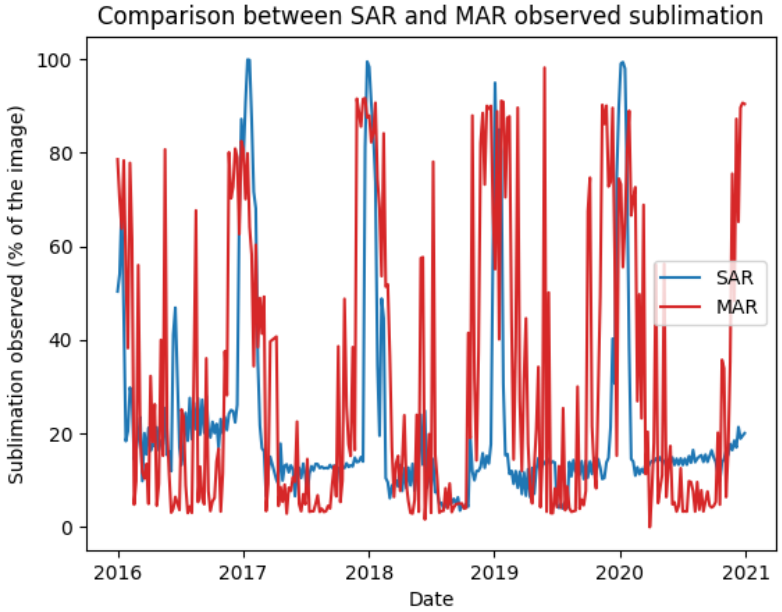

Figure 8.10: Evolution of quantity of liquid water detected by SAR and MAR SU in the whole studied zone.

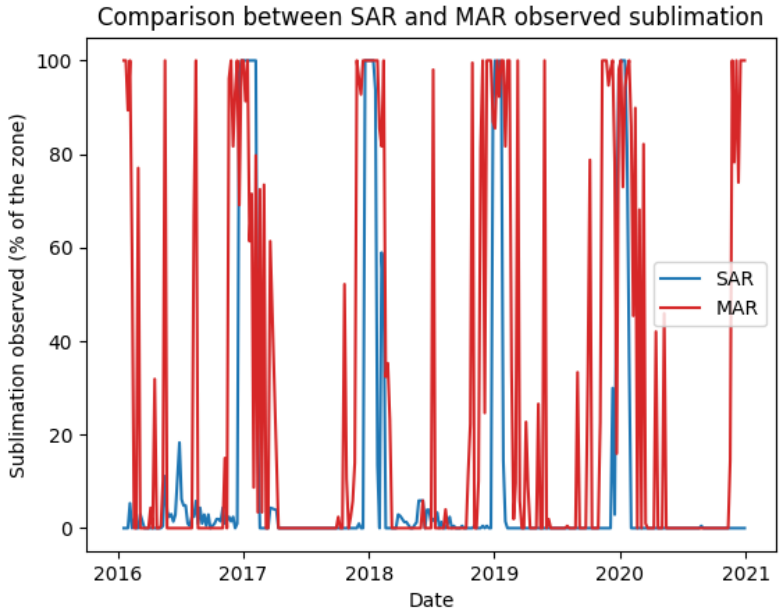

Figure 8.11: Evolution of quantity of liquid water detected by SAR and MAR SU in the limited area.

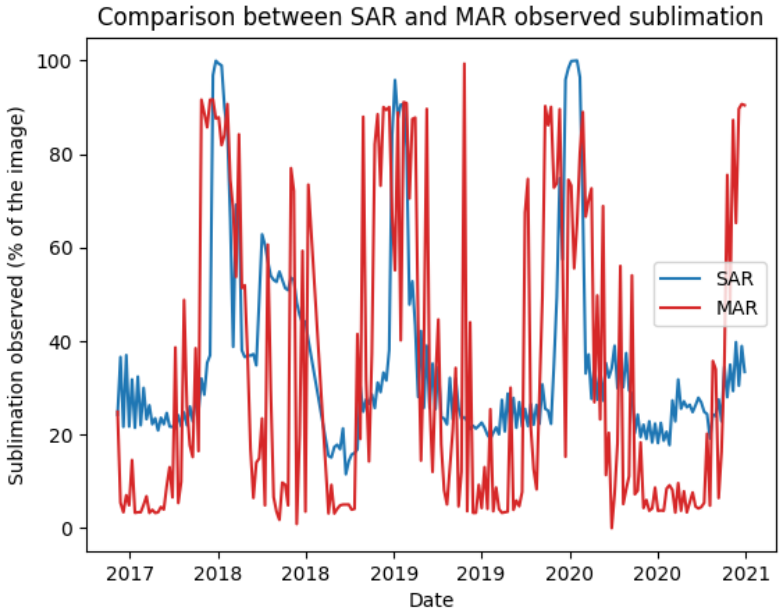

Figure 8.12: Evolution of quantity of liquid water detected by SAR and by MAR SU in the whole studied zone with HV polarisation.

8.3.3 Spatial Analysis

WR

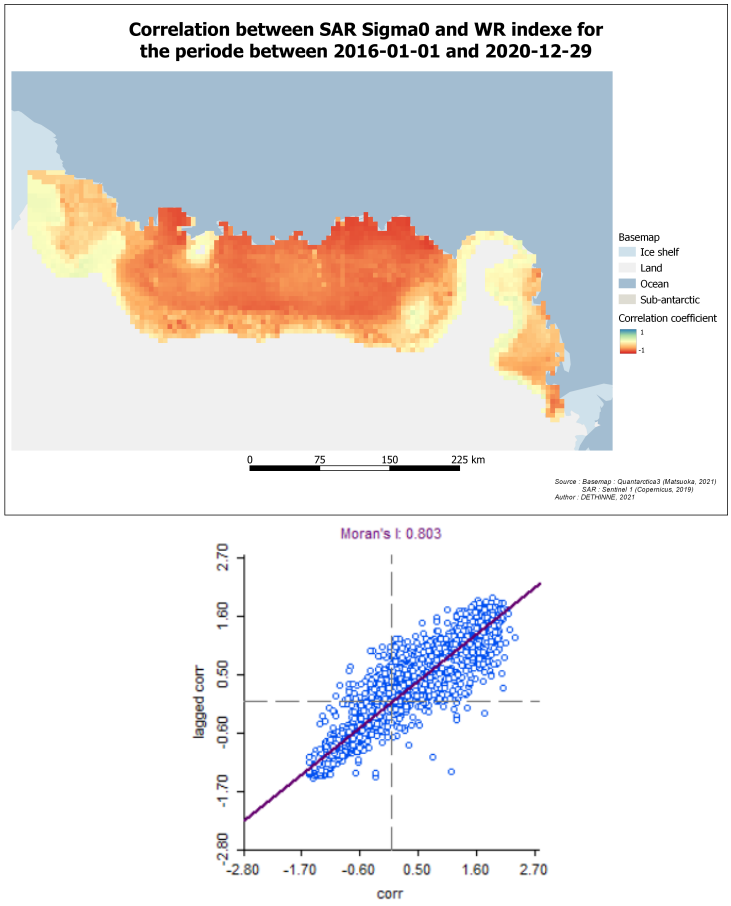

Figure 8.13: Correlation map between SAR σ_0 and WR.

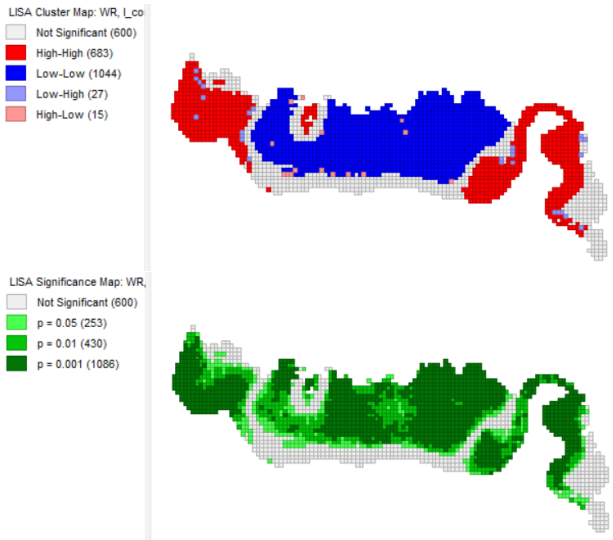

Figure 8.14: Local Moran's I map (top) and its statistical significance (bottom) for the correlation map between SAR σ_0 and WR.

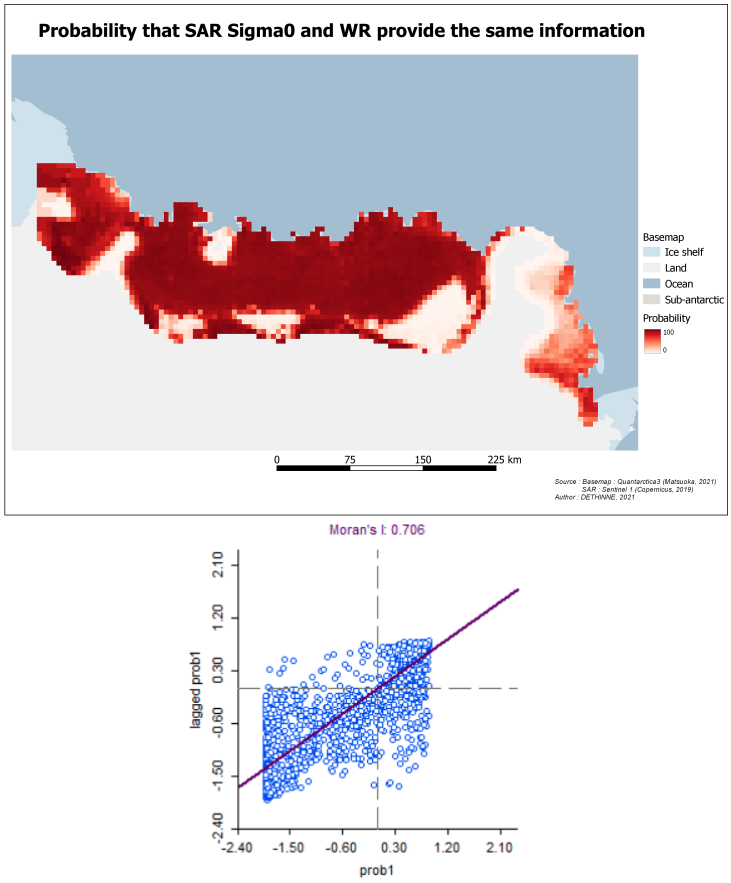

Figure 8.15: Probability map of SAR σ_0 and WR corresponding together.

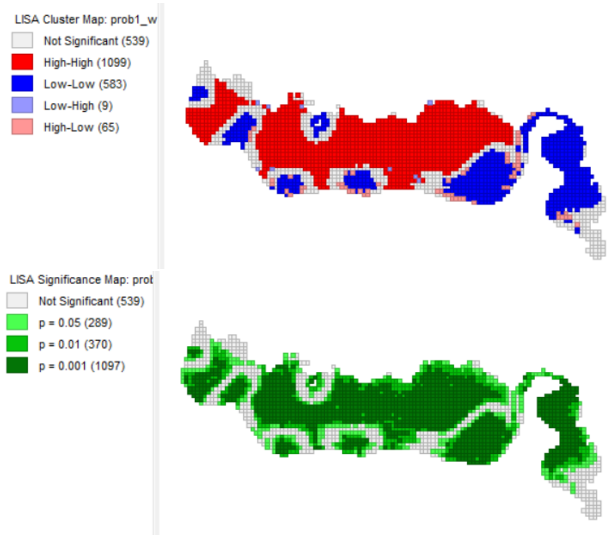

Figure 8.16: Local Moran's I map (top) and its statistical significance (bottom) for the probability map of SAR σ_0 and WR.

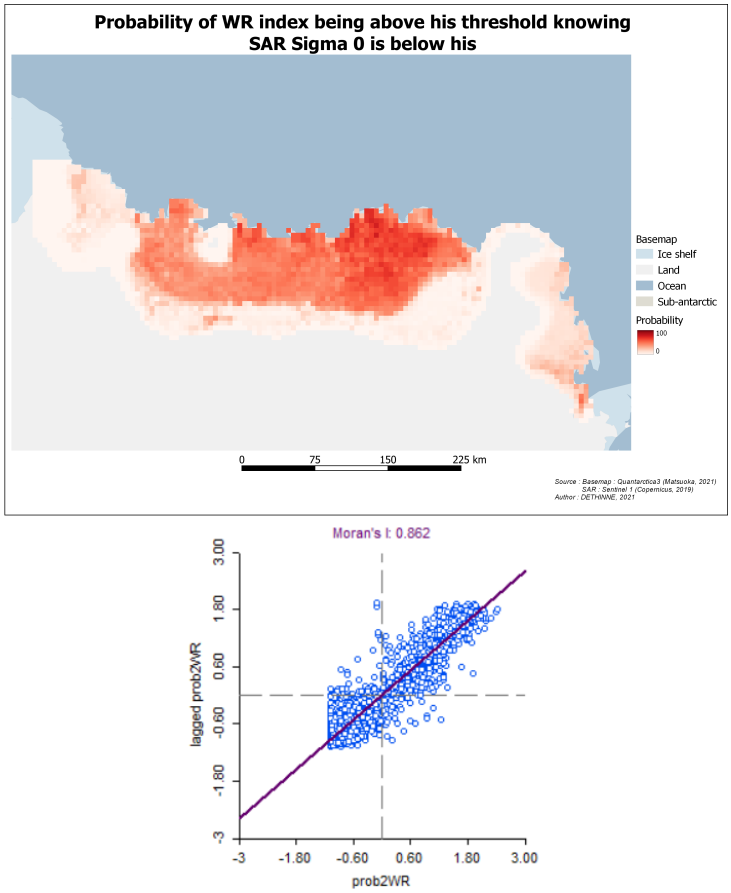

Figure 8.17: Probability map of WR modelling melt knowing SAR detects it.

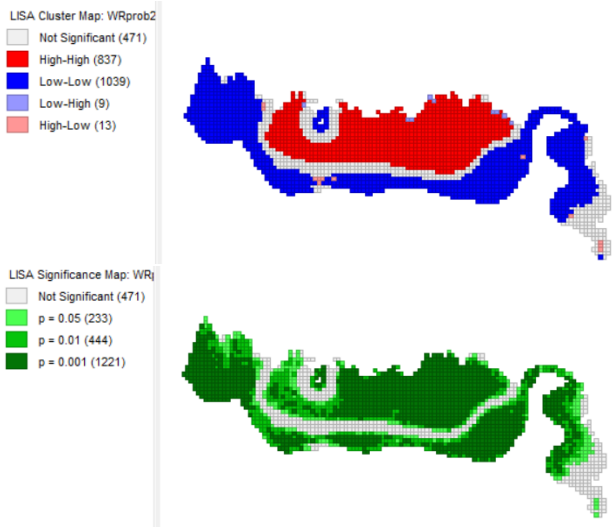

Figure 8.18: Local Moran's I map (top) and its statistical significance (bottom) for the probability map of WR modelling melt knowing SAR detects it.

WA1

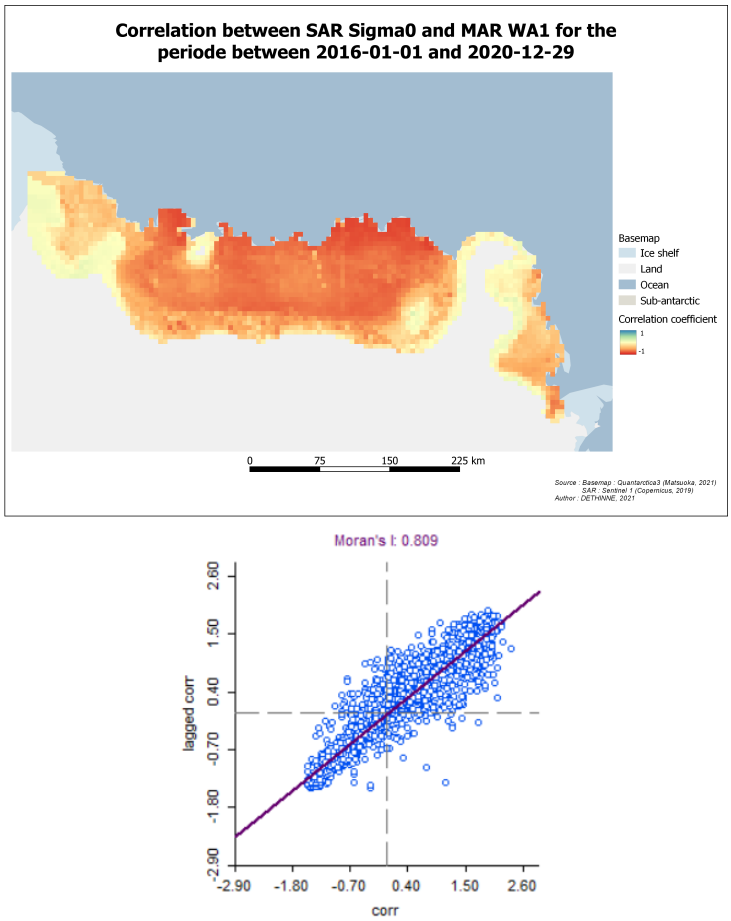

Figure 8.19: Correlation map between SAR σ_0 and WA.

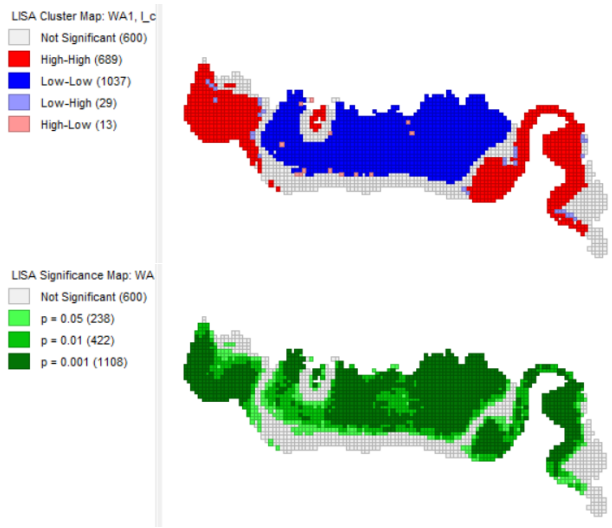

Figure 8.20: Local Moran's I map (top) and its statistical significance (bottom) for the correlation map between SAR σ_0 and WA1.

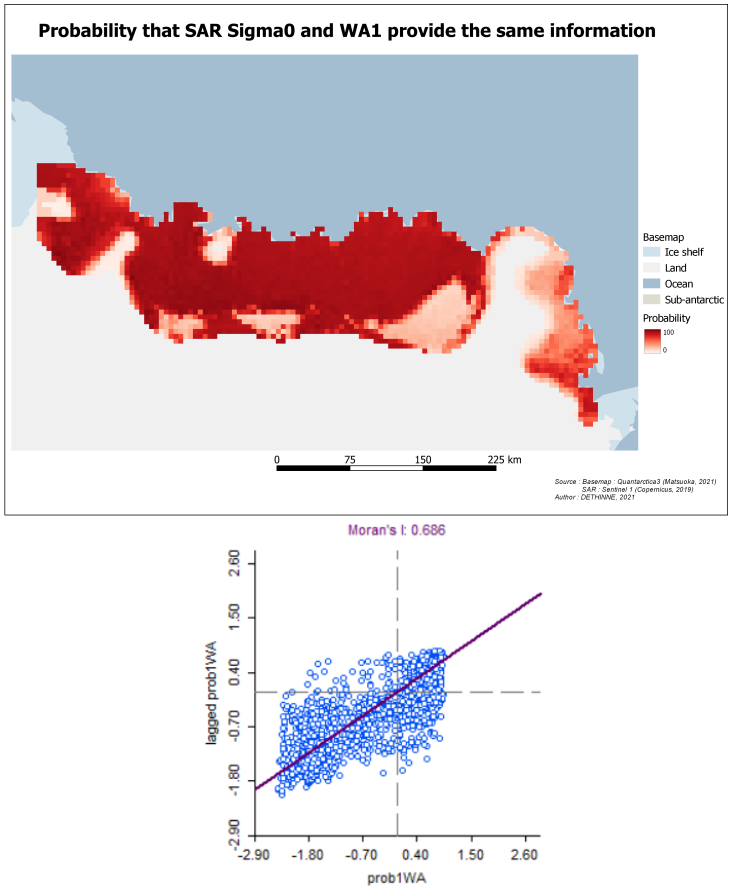

Figure 8.21: Probability map of SAR σ_0 and WA1 corresponding together.

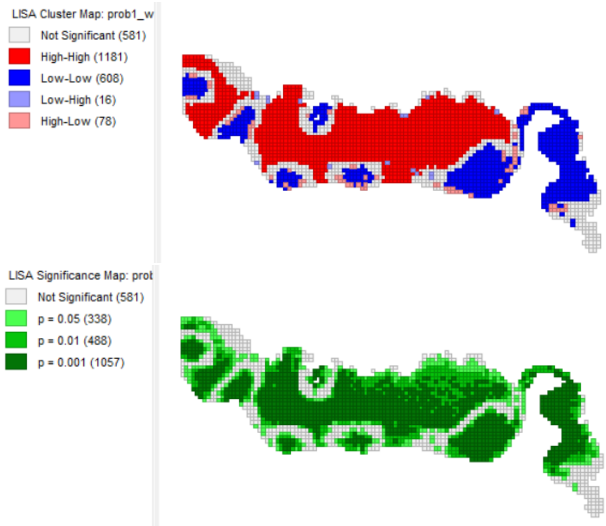

Figure 8.22: Local Moran's I map (top) and its statistical significance (bottom) for the probability map of SAR σ_0 and WA1.

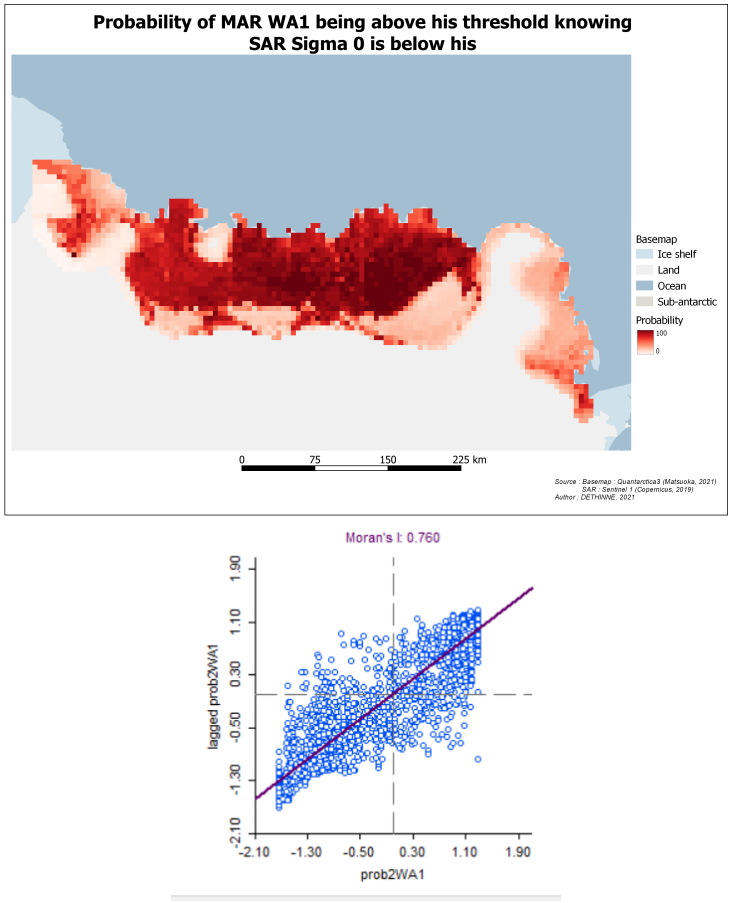

Figure 8.23: Probability map of WA1 modelling liquid water knowing SAR detects it.

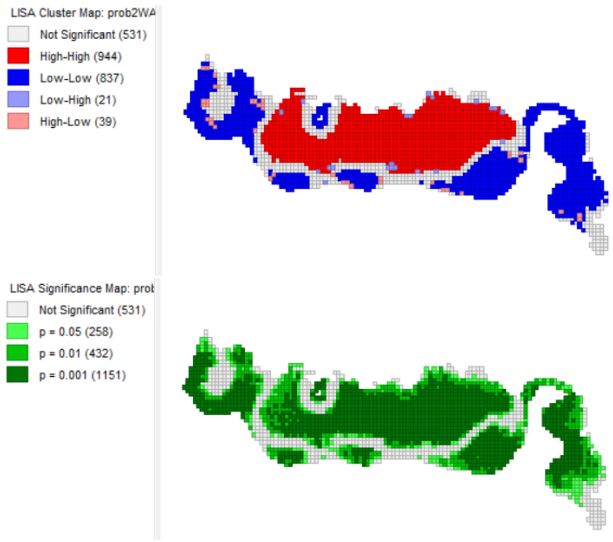

Figure 8.24: Local Moran's I map (top) and its statistical significance (bottom) for the probability map of WA modelling liquid water knowing SAR detects it.

RU

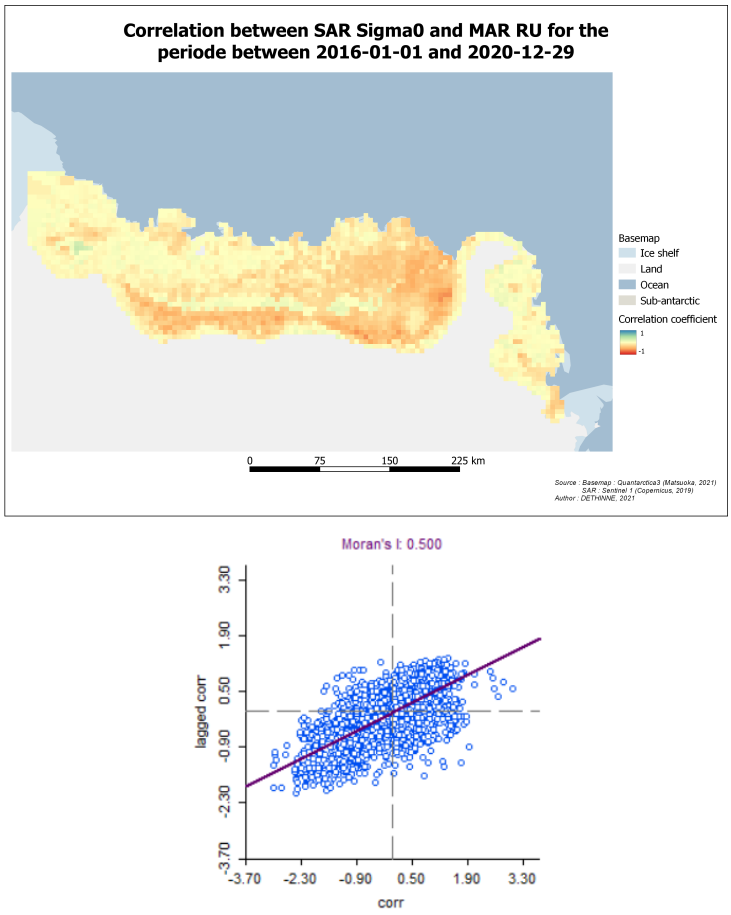

Figure 8.25: Correlation map between SAR σ_0 and RU.

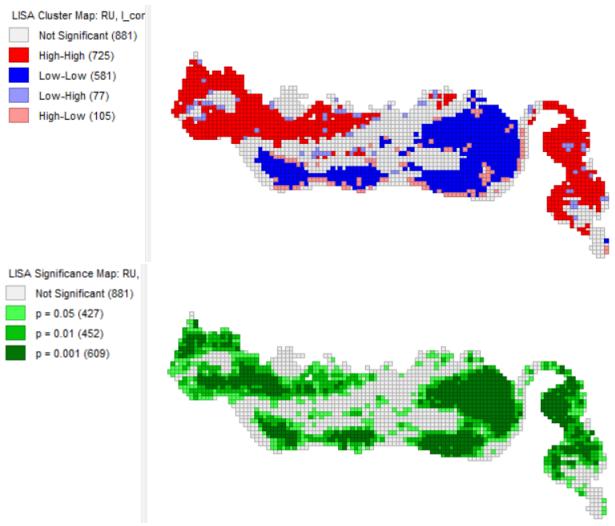

Figure 8.26: Local Moran's I map (top) and its statistical significance (bottom) for the correlation map between SAR σ_0 and RU.

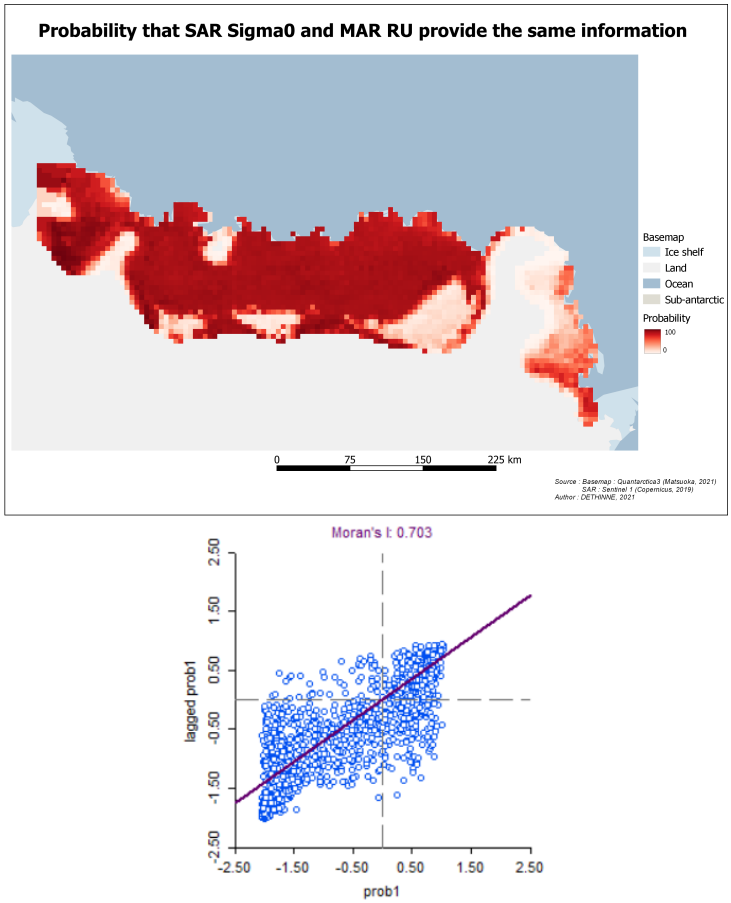

Figure 8.27: Probability map of SAR σ_0 and RU corresponding together.

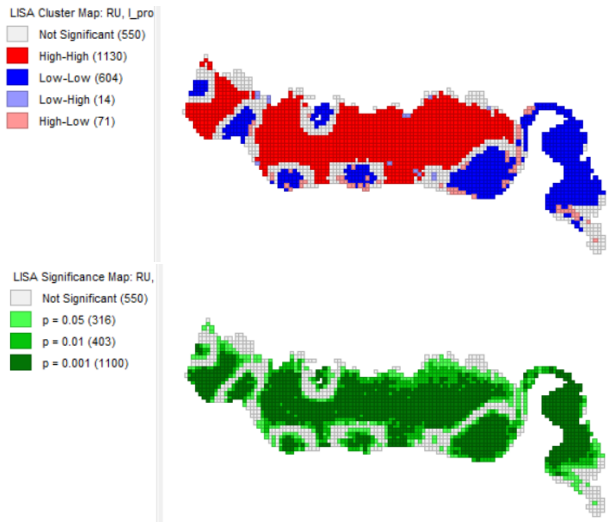

Figure 8.28: Local Moran's I map (top) and its statistical significance (bottom) for the probability map of SAR σ_0 and RU.

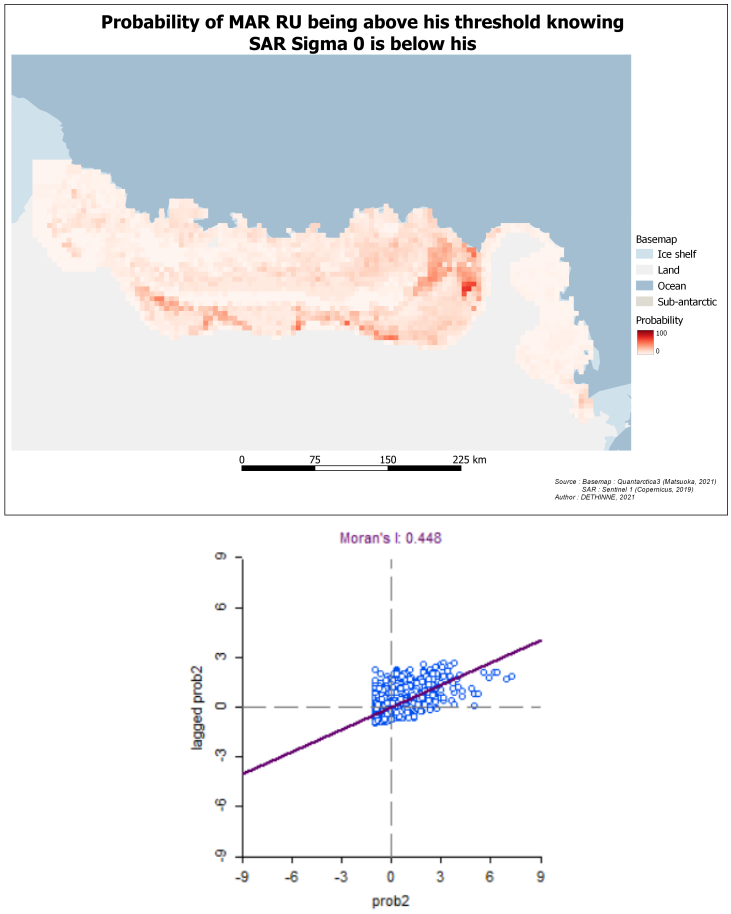

Figure 8.29: Probability map of RU modelling runoff knowing SAR detects melting.

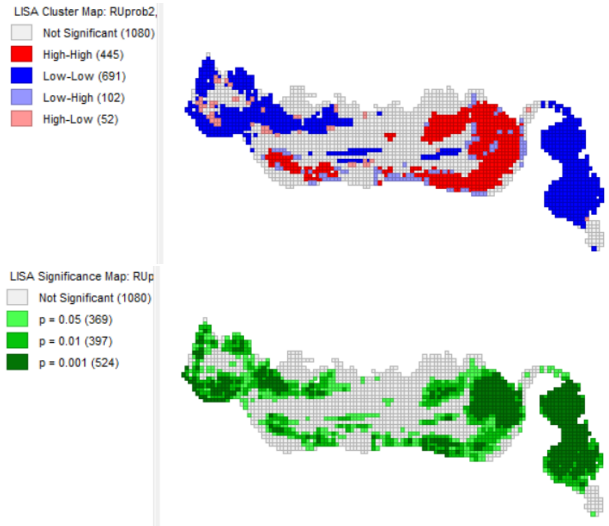

Figure 8.30: Local Moran's I map (top) and its statistical significance (bottom) for the probability map of RU modelling runoff knowing SAR detects melting.

SU

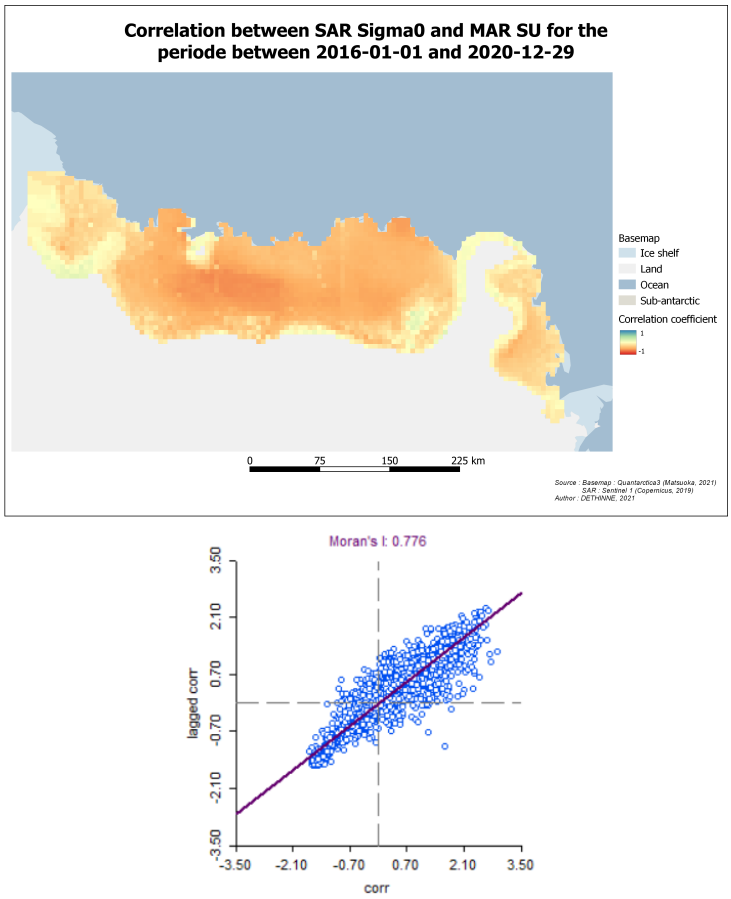

Figure 8.31: Correlation map between SAR σ_0 and SU.

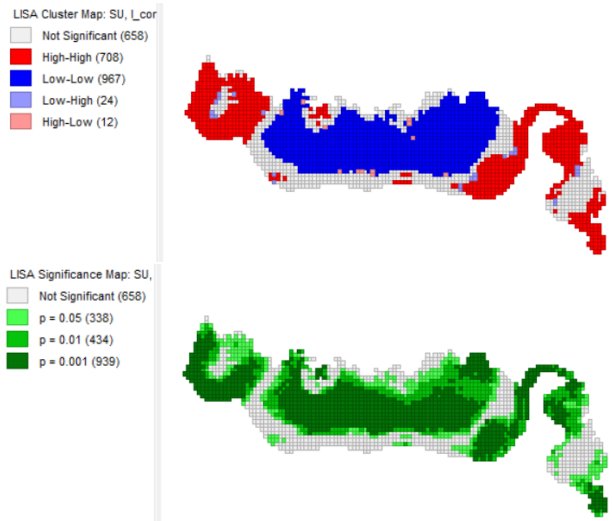

Figure 8.32: Local Moran's I map (top) and its statistical significance (bottom) for the correlation map between SAR σ_0 and SU.

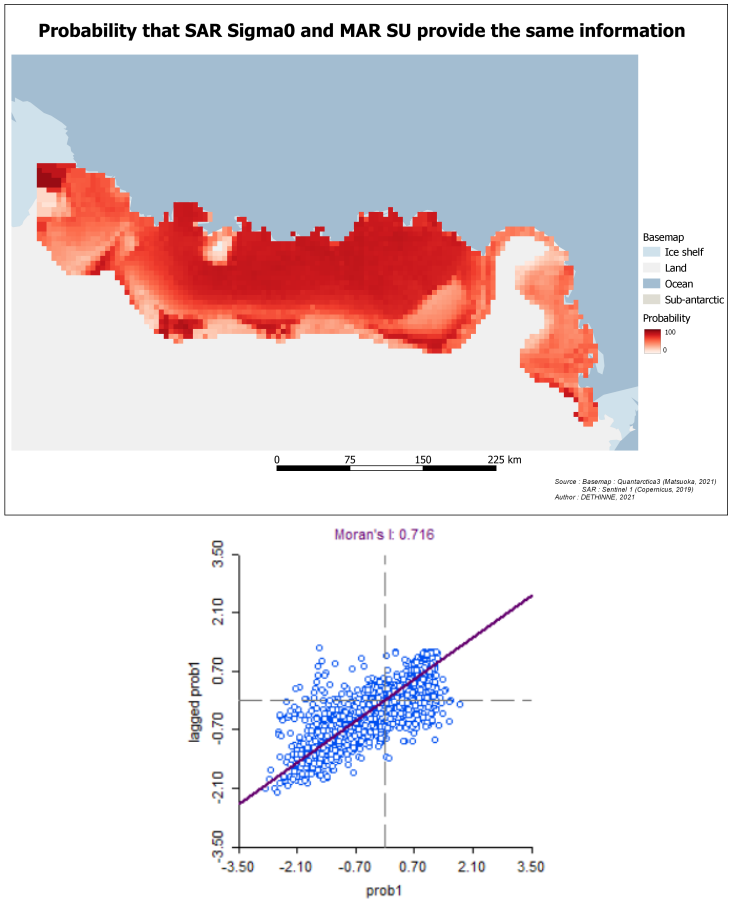

Figure 8.33: Probability map of SAR σ_0 and SU corresponding together.

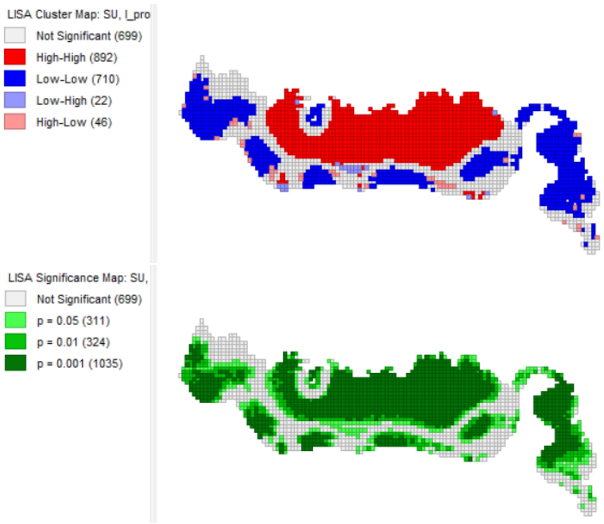

Figure 8.34: Local Moran's I map (top) and its statistical significance (bottom) for the probability map of SAR σ_0 and SU.

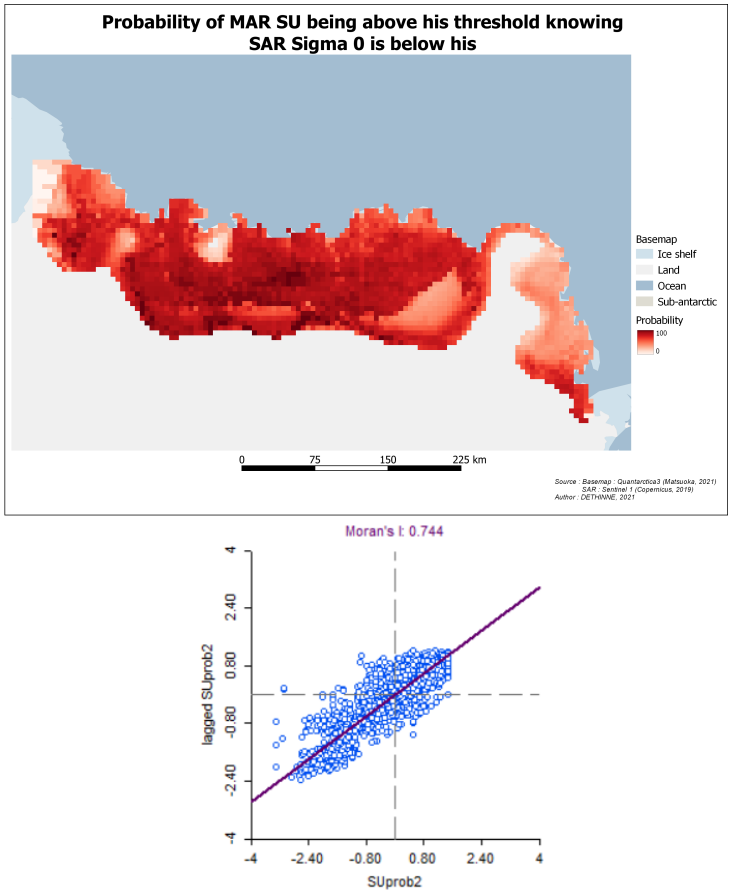

Figure 8.35: Probability map of SU modelling sublimation knowing SAR detects melting.

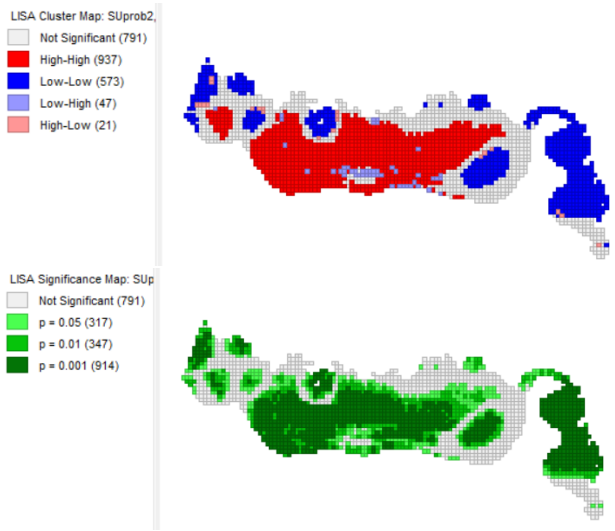

Figure 8.36: Local Moran's I map (top) and its statistical significance (bottom) for the probability map of SU modelling sublimation knowing SAR detects melting.

References

Amory, C., Kittel, C., Le Toumelin, L., Agosta, C., Delhasse, A., Favier, V., & Fettweis, X. (2020). Performance of MAR (v3.11) in simulating the drifting-snow climate and surface mass balance of Adelie Land, East Antarctica. *Geoscientific Model Development Discussions*, *2020*, 35 p. Retrieved from `https://gmd.copernicus.org/preprints/gmd-2020-368/` doi: 10.5194/gmd-2020-368

ASF. (2021). *ASF Data Search.* Alaska Satellite facility (ASF). Retrieved 26 May 2021, from `https://search.asf.alaska.edu/#/`

Baghdadi, N., Gauthier, Y., Bernier, M., & Fortin, J.-P. (2000). Potential and limitations of RADARSAT SAR data for wet snow monitoring. *IEEE Transactions on Geoscience and Remote Sensing*, *38*(1), 316–320. doi: 10.1109/36.823925

Banwell, A. F., & Macayeal, D. R. (2015). Ice-shelf fracture due to viscoelastic flexure stress induced by fill/drain cycles of supraglacial lakes. *Antarctic Science*, *27*(6), 587–597. doi: 10.1017/S0954102015000292

Bartels-Rausch, T., Bergeron, V., Cartwright, J. H. E., Escribano, R., Finney, J. L., Grothe, H., ... Uras-Aytemiz, N. (2012). Ice structures, patterns, and processes: A view across the icefields. *Reviews of Modern Physics*, *84*(2), 885–944. doi: 10.1103/RevModPhys.84.885

Boain, R. J. (2004). A-B-Cs of sun-synchronous orbit mission design. In *Advances in the astronautical sciences.*

Buchelt, S., Skov, K., & Ullmann, T. (2021). Sentinel-1 time series for mapping snow cover and timing of snowmelt in Arctic periglacial environments: Case study from the Zackenberg Valley, Greenland. *The Cryosphere Discussions*, 24 p. Retrieved from `https://tc.copernicus.org/preprints/tc-2021-78/` doi: 10.5194/tc-2021-78

Copernicus. (2019). *À propos de Copernicus.* Copernicus. Retrieved 26 May 2021, from `https://www.copernicus.eu/fr/propos-de-copernicus`

Cutrona, L., Vivian, W., Leith, E., & Hall, G. (1961). Synthetic Aperture Radars:

A paradigm for technology evolution. *IRE Transactions on Military Electronics*, 127-131.

Davies, B. (2020). *Ice Shelves.* AntarcticGlaciers.org. Retrieved 14 May 2021, from `http://www.antarcticglaciers.org/glaciers-and-climate/shrinking-ice-shelves/ice-shelves/`

Dupont, T. K., & Alley, R. B. (2006). Role of small ice shelves in sea-level rise. *Geophysical Research Letters*, *33*(9), 4 p. doi: 10.1029/2005GL025665

EO College. (2020). *Echoes in space.* EO college. Retrieved 14 May 2021, from `https://eo-college.org/courses/echoes-in-space/`

EO College. (2021). *Principes fondamentaux de la rétrodiffusion radar.* EO college. Retrieved 6 April 2021, from `https://eo-college.org/courses/principes-de-la-retrodiffusion-radar/`

ESA. (2019). *Sentinel-1.* European Spatial Agency (ESA). Retrieved 26 May 2021, from `https://sentinel.esa.int/web/sentinel/missions`

Ferguson, S. H., Taylor, M. K., & Messier, F. (2000). Influence of Sea Ice Dynamics on Habitat Selection by Polar Bears . *Ecology*, *81*(3), 761–772. doi: 10.1175/1520-0493(1994)122\%3C0671:DOATDM\%3E2.0.CO;2

Fettweis, X. (2007). Reconstruction of the 1979-2006 Greenland ice sheet surface mass balance using the regional climate model MAR. *The Cryosphere*, *1*(1), 21–40. doi: 10.5194/tc-1-21-2007

Fettweis, X., Gallée, H., Lefebre, F., & van Ypersele, J.-P. (2006). The 1988-2003 Greenland ice sheet melt extent using passive microwave satellite data and a regional climate model. *Climate Dynamics*, *27*(5), 531–541. doi: 10.1007/s00382-006-0150-8

Fettweis, X., Tedesco, M., van den Broeke, M., & Ettema, J. (2011). Melting trends over the Greenland ice sheet (1958-2009) from spaceborne microwave data and regional climate models. *The Cryosphere*, *5*(2), 359–375. doi: 10.5194/tc-5-359-2011

Fretwell, P., Pritchard, H. D., Vaughan, D. G., Bamber, J. L., Barrand, N. E., Bell, R., ... Zirizzotti, A. (2013). Bedmap2: Improved ice bed, surface and thickness datasets for Antarctica. *The Cryosphere*, *7*(1), 375–393. doi: 10.5194/tc-7-375-2013

Fretwell, P. T., LaRue, M. A., Morin, P., Kooyman, G. L., Wienecke, B., Ratcliffe, N., ... Trathan, P. N. (2012). An emperor penguin population estimate: The first global, synoptic survey of a species from space. *PLOS ONE*, *7*(4), 11 p. doi: 10.1371/journal.pone.0033751

Gallée, H. (1995). Simulation of the Mesocyclonic Activity in the Ross Sea,

Antarctica. *Monthly Weather Review*, *123*(7), 2051–2069. doi: 10.1175/1520-0493(1995)123⟨2051:sotmai⟩2.0.co;2

Gallée, H., Guyomarc'h, G., & Brun, E. (2001). Impact of Snow Drift on the Antarctic Ice Sheet Surface Mass Balance: Possible Sensitivity to Snow-Surface Properties. *Boundary-Layer Meteorology*, *99*, 1–19. doi: 10.1023/A:1018776422809

Gallée, H., & Schayes, G. (1994). Development of a Three-Dimensional Meso-γ Primitive Equation Model: Katabatic Winds Simulation in the Area of Terra Nova Bay, Antarctica. *Monthly Weather Review*, *122*, 671–685.

Gilbert, E., & Kittel, C. (2021). Surface Melt and Runoff on Antarctic Ice Shelves at 1.5°C, 2°C and 4°C of Future Warming. *Geophysical Research Letters*, *48*(8). doi: 10.1029/2020GL091733

Glaude, Q. (2018). *Télédétection radar.* University Lecture, University of Liège. Retrieved from `http://hdl.handle.net/2268/223142`

Gloersen, P., Campbell, W. J., Cavalieri, D. J., Comiso, J. C., Parkinson, C. L., & Zwally, H. J. (1993). Satellite passive microwave observations and analysis of Arctic and Antarctic sea ice, 1978-1987. *Annals of Glaciology*, *17*, 149–154. doi: 10.3189/S0260305500012751

Goodchild, M. F. (1986). Spatial Autocorrelation. *Concepts and Techniques in Modern Geography (CATMOG)*, *47*.

Harris, C. M., Lorenz, K., Fishpool, L. D. C., Lascelles, B., Cooper, J., Coria, N. R., ... Woehler, E. J. (2015). Important Bird Areas in Antarctica 2015. *BirdLife International and Environmental Research & Assessment Ltd., Cambridge*.

Harris, C. R., Millman, K. J., van der Walt, S. J., Gommers, R., Virtanen, P., Cournapeau, D., ... Oliphant, T. E. (2020). Array programming with NumPy. *Nature*, *585*, 357–362. doi: 10.1038/s41586-020-2649-2

Hersbach, H., Bell, B., Berrisford, P., Hirahara, S., Horányi, A., Muñoz-Sabater, J., ... Thépaut, J. N. (2020). The ERA5 global reanalysis. *Quarterly Journal of the Royal Meteorological Society*, *146*(730), 1999–2049. doi: 10.1002/qj.3803

Hui, F., Ci, T., Cheng, X., Scambos, T. A., Liu, Y., Zhang, Y., ... Wang, K. (2014). Mapping blue-ice areas in Antarctica using ETM+ and MODIS data. *Annals of Glaciology*, *55*(66), 129–137. doi: 10.3189/2014AoG66A069

Johnson, A., Fahnestock, M., & Hock, R. (2020). Evaluation of passive microwave melt detection methods on Antarctic Peninsula ice shelves using time series of Sentinel-1 SAR. *Remote Sensing of Environment*, *250*, 10 p. doi: 10.1016/

j.rse.2020.112044

Kittel, C. (2021). *Present and future sensitivity of the Antarctic surface mass balance to oceanic and atmospheric forcings: insights with the regional climate model MAR.* PhD thesis, Liège, University of Liège, 246 p.

Kittel, C., Amory, C., Agosta, C., Delhasse, A., Doutreloup, S., Huot, P.-V., ... Fettweis, X. (2018). Sensitivity of the current Antarctic surface mass balance to sea surface conditions using MAR. *The Cryosphere*, *12*(12), 3827–3839. doi: 10.5194/tc-12-3827-2018

Kittel, C., Amory, C., Agosta, C., Jourdain, N. C., Hofer, S., Delhasse, A., ... Fettweis, X. (2021). Diverging future surface mass balance between the Antarctic ice shelves and grounded ice sheet. *The Cryosphere*, *15*(3), 1215–1236. doi: 10.5194/tc-15-1215-2021

Koskinen, J. T., Pulliainen, J. T., & Hallikainen, M. T. (1997). The use of ERS-1 SAR data in snow melt monitoring. *IEEE Transactions on Geoscience and Remote Sensing*, *35*(3), 601–610. doi: 10.1109/36.581975

Lee, J.-S., Wen, J.-H., Ainsworth, T., Chen, K., & Chen, A. (2009). Improved sigma filter for speckle filtering of sar imagery. *IEEE Transactions on Geoscience and Remote Sensing*, *47*, 202-213.

Lefebre, F., Gallée, H., van Ypersele, J.-P., & Greuell, W. (2003). Modeling of snow and ice melt at ETH Camp (West Greenland): A study of surface albedo. *Journal of Geophysical Research: Atmospheres*, *108*(8). doi: 10.1029/2001JD001160

Lenaerts, J. T. M., Lhermitte, S., Drews, R., Ligtenberg, S. R., Berger, S., Helm, V., ... Pattyn, F. (2016). Meltwater produced by wind-albedo interaction stored in an East Antarctic ice shelf. *Nature Climate Change*, *7*(1), 58–62. doi: 10.1038/nclimate3180

Lenaerts, J. T. M., Medley, B., van den Broeke, M. R., & Wouters, B. (2019). Observing and Modeling Ice Sheet Surface Mass Balance. *Reviews of Geophysics*, *57*(2), 376–420. doi: 10.1029/2018RG000622

Liang, D., Guo, H., Zhang, L., Cheng, Y., Zhu, Q., & Liu, X. (2021). Time-series snowmelt detection over the Antarctic using Sentinel-1 SAR images on Google Earth Engine. *Remote Sensing of Environment*, *256*, 17 p. doi: 10.1016/j.rse.2021.112318

Lievens, H., Demuzere, M., Marshall, H. P., Reichle, R. H., Brucker, L., Brangers, I., ... De Lannoy, G. J. (2019). Snow depth variability in the Northern Hemisphere mountains observed from space. *Nature Communications*, *10*, 12 p. Retrieved from `http://dx.doi.org/10.1038/s41467-019-12566-y`

doi: 10.1038/s41467-019-12566-y

Mahmud, M. S., Nandan, V., Howell, S. E., Geldsetzer, T., & Yackel, J. (2020). Seasonal evolution of L-band SAR backscatter over landfast Arctic sea ice. *Remote Sensing of Environment*, *251*, 19 p. Retrieved from `https://doi.org/10.1016/j.rse.2020.112049` doi: 10.1016/j.rse.2020.112049

Matsuoka, K., Skoglund, A., Roth, G., de Pomereu, J., Griffiths, H., Headland, R., ... Melvær, Y. (2021). Quantarctica, an integrated mapping environment for Antarctica, the Southern Ocean, and sub-Antarctic islands. *Environmental Modelling and Software*, *140*, 14 p. doi: 10.1016/j.envsoft.2021.105015

Morcrette, J. J. (2002). Assessment of the ECMWF Model Cloudiness and Surface Radiation Fields at the ARM SGP Site. *Monthly Weather Review*, *130*, 257–277. doi: 10.1175/1520-0493(2002)130⟨0257:AOTEMC⟩2.0.CO;2

Moreira, A., Prats-Iraola, P., Younis, M., Krieger, G., Hajnsek, I., & Papathanassiou, K. P. (2013). A Tutorial on Synthetic Aperture Radar. *IEEE Geoscience and Remote Sensing Magazine*, *1*, 6-43. doi: 10.1109/MGRS.2013.2248301

Nagler, T., & Rott, H. (2000). Retrieval of wet snow by means of multitemporal SAR data. *IEEE Transactions on Geoscience and Remote Sensing*, *38*(2), 754–765. doi: 10.1109/36.842004

Nagler, T., Rott, H., Hetzenecker, M., Wuite, J., & Potin, P. (2015). The Sentinel-1 Mission: New Opportunities for Ice Sheet Observations. *Remote Sensing*, *7*(7), 9371–9389. doi: 10.3390/rs70709371

Nagler, T., Rott, H., Ripper, E., Bippus, G., & Hetzenecker, M. (2016). Advancements for Snowmelt Monitoring by Means of Sentinel-1 SAR. *Remote Sensing*, *8*(4), 17 p. doi: 10.3390/rs8040348

Nuñez, C. (2019). *Sea level rise, facts and information.* National Geographic. Retrieved 3 May 2021, from `https://www.nationalgeographic.com/environment/global-warming/sea-level-rise/`

Paolo, F. S., Fricker, H. A., & Padman, L. (2015). Volume loss from Antarctic ice shelves is accelerating. *Science*, *348*(6232), 327–331. doi: 10.1126/science.aaa0940

Parkinson, C. (2001). Satellite Passive Microwave Measurements of Sea Ice. *Encyclopedia of Ocean Sciences*, 2531–2539. doi: 10.1006/rwos.2001.0336

Parotto, G. (2019). *Investigating the influence of aeolian snow transport processes on the representation of the climate. a modelling study using a high-resolution regional climate model over the period 1980-2018.* Master thesis in sciences geography, Liège, University of Liège, unpublished, 53 p.

Price, M. R., Heywood, K. J., & Nicholls, K. W. (2008). Ice-shelf - Ocean interactions at Fimbul Ice Shelf, Antarctica from oxygen isotope ratio measurements. *Ocean Science*, *4*, 89–98. doi: 10.5194/os-4-89-2008

Pritchard, H. D., Ligtenberg, S. R., Fricker, H. A., Vaughan, D. G., Van Den Broeke, M. R., & Padman, L. (2012). Antarctic ice-sheet loss driven by basal melting of ice shelves. *Nature*, *484*, 502–505. doi: 10.1038/nature10968

Ramjan, S., Geldsetzer, T., Scharien, R., & Yackel, J. (2018). Predicting Melt Pond Fraction on Landfast Snow Covered First Year Sea Ice from Winter C-Band SAR Backscatter Utilizing Linear, Polarimetric and Texture Parameters. *Remote Sensing*, *10*(10), 21 p. doi: 10.3390/rs10101603

Reese, R., Gudmundsson, G. H., Levermann, A., & Winkelmann, R. (2018). The far reach of ice-shelf thinning in Antarctica. *Nature Climate Change*, *8*, 53–57. doi: 10.1038/s41558-017-0020-x

Rignot, E., Bamber, J. L., Van Den Broeke, M. R., Davis, C., Li, Y., Van De Berg, W. J., & Van Meijgaard, E. (2008). Recent Antarctic ice mass loss from radar interferometry and regional climate modelling. *Nature Geoscience*, *1*, 106–110. doi: 10.1038/ngeo102

Rignot, E., Jacobs, S., Mouginot, J., & Scheuchl, B. (2013). Ice-shelf Melting Around Antarctica. *Science*, *341*(6143), 266–270. doi: 10.1126/science.1235798

Rignot, E., Mouginot, J., & Scheuchl, B. (2017). *MEaSUREs InSAR-Based Antarctica Ice Velocity Map, Version 2* (No. 66). Boulder, Colorado USA. NASA National Snow and Ice Data Center Distributed Active Archive Center. doi: 10.5067/D7GK8F5J8M8R

Scambos, T., Bohlander, J. A., Shuman, C. A., & Skvarca, P. (2004). Glacier acceleration and thinning after ice shelf collapse in the Larsen B embayment, Antarctica. *Geophysical Research Letters*, *31*(18), 4 p. doi: 10.1029/2004GL020670

Scambos, T., Hulbe, C., & Fahnestock, M. (2013). Climate-Induced Ice Shelf Disintegration in the Antarctic Peninsula. *Antarctic Peninsula Climate Variability*, *79*, 79–92. doi: 10.1029/ar079p0079

Shah, E., Jayaprasad, P., & James, M. E. (2019). Image Fusion of SAR and Optical Images for Identifying Antarctic Ice Features. *Journal of the Indian Society of Remote Sensing*, *47*(12), 2113–2127. doi: 10.1007/s12524-019-01040-3

Shepherd, A., & Wingham, D. (2007). Recent Sea-Level Contributions of the Antarctic and Greenland Ice Sheets. *Science*, *315*(March), 1529–1533. doi: 10.1126/science.1136776

Small, D. (2011). Flattening gamma: Radiometric terrain correction for SAR imagery. *IEEE Transactions on Geoscience and Remote Sensing*, *49*(8), 3081–3093. doi: 10.1109/TGRS.2011.2120616

Small, D., & Schubert, A. (2008). Guide to ASAR Geocoding. RSL-ASAR-GC-AD, Issue 1.0, 36 p. Retrieved from `https://www.geo.uzh.ch/microsite/rsl-documents/research/publications/other-sci-communications/2008_RSL-ASAR-GC-AD-v101-0335607552/2008_RSL-ASAR-GC-AD-v101.pdf`

Stern, N. (2007). *The economics of climate change: The stern review*. Cambridge University Press. doi: 10.1017/CBO9780511817434

The IMBIE team, Shepherd, A., & Ivins, E. (2018). Mass balance of the Antarctic ice sheet from 1992 to 2017. *Nature*, *558*, 219–222. doi: 10.1038/s41586-018-0179-y10.1098/rsta.2006.1792

Thomas, R., Rignot, E., Casassa, G., Kanagaratnam, P., Acuna, C., Akins, T., ... Zwally, H. J. (2004). Accelerated Sea-Level Rise from West Antarctica. *Science*, *306*(October), 255–258.

Tychon, B. (2019). *Télédétection, Télédétection par hyperfréquences.* University Lecture, University of Liège.

USGS. (2020). *What is remote sensing and what is it used for?* United States Geological Survey (USGS). Retrieved 11 May 2021, from `https://www.usgs.gov/faqs/what-remote-sensing-and-what-it-used?qt-news_science_products=0\#qt-news_science_products`

Walker, R. T., Dupont, T. K., Parizek, B. R., & Alley, R. B. (2008). Effects of basal-melting distribution on the retreat of ice-shelf grounding lines. *Geophysical Research Letters*, *35*(17), 5 p. doi: 10.1029/2008GL034947

Wiley, C. A. (1985). Synthetic Aperture Radars: A paradigm for technology evolution. *IEEE Transactions on Aerospace and Electronic Systems*, *AES-21*(3), 440-443. doi: 10.1109/TAES.1985.310578

Winebrennernelson, D. P., Nelson, E., Colony, R., & West, R. D. (1994). Observation of melt onset on multiyear Arctic sea ice using the ERS 1 synthetic aperture radar. *Journal of Geophysical Research*, *99*(C11), 22425–22441. doi: 10.1029/94jc01268